SAND2016-9828

SANDIA REPORT

SAND2014-0763
Printed September 2016

Imaging LIDAR through Fog and Dust for Maritime Surveillance

S.A. Kemme, J.B. Wright, J.D. van der Laan

Prepared by
Sandia National Laboratories
Albuquerque, New Mexico 87185 and Livermore, California 94550

Sandia National Laboratories is a multi-mission laboratory managed and operated by Sandia Corporation, a wholly owned subsidiary of Lockheed Martin Corporation, for the U.S. Department of Energy's National Nuclear Security Administration under contract DE-AC04-94AL85000.

Sandia National Laboratories

Issued by Sandia National Laboratories, operated for the United States Department of Energy by Sandia Corporation.

NOTICE: This report was prepared as an account of work sponsored by an agency of the United States Government. Neither the United States Government, nor any agency thereof, nor any of their employees, nor any of their contractors, subcontractors, or their employees, make any warranty, express or implied, or assume any legal liability or responsibility for the accuracy, completeness, or usefulness of any information, apparatus, product, or process disclosed, or represent that its use would not infringe privately owned rights. Reference herein to any specific commercial product, process, or service by trade name, trademark, manufacturer, or otherwise, does not necessarily constitute or imply its endorsement, recommendation, or favoring by the United States Government, any agency thereof, or any of their contractors or subcontractors. The views and opinions expressed herein do not necessarily state or reflect those of the United States Government, any agency thereof, or any of their contractors.

Printed in the United States of America. This report has been reproduced directly from the best available copy.

Available to DOE and DOE contractors from
U.S. Department of Energy
Office of Scientific and Technical Information
P.O. Box 62
Oak Ridge, TN 37831

Telephone: (865) 576-8401
Facsimile: (865) 576-5728
E-Mail: reports@osti.gov
Online ordering: http://www.osti.gov/scitech

Available to the public from
U.S. Department of Commerce
National Technical Information Service
5301 Shawnee Rd
Alexandria, VA 22312

Telephone: (800) 553-6847
Facsimile: (703) 605-6900
E-Mail: orders@ntis.gov
Online order: http://www.ntis.gov/search

SAND2014-0763

September, 2016

Imaging LIDAR through Fog and Dust for Maritime Surveillance

Shanalyn A. Kemme, Jeremy B. Wright, John D. van der Laan
SOF and EO/IR Systems
Sandia National Laboratories
P.O. Box 5800
Albuquerque, New Mexico 87185-MS0957

Abstract

This work supports Airborne Intelligence, Surveillance, and Reconnaissance (ISR) for tactical situational awareness in challenging environments with modified imaging LIDAR (light detection and ranging). LIDAR produces an irradiance-based scene with high, three-dimensional, spatial resolution; differentiating reflecting surfaces and surface textures not just for target detection, but also target recognition.

LIDAR is generally prevented from working through all weather; as the traditional source wavelengths are scattered and/or absorbed by fog, clouds, and dust known as degraded visual environments (DVEs). This work identifies and quantifies improved optical wavelength regimes and polarization strategies that should open this otherwise denied operating window for LIDAR. We demonstrate modified imaging LIDAR's utility and ability to produce images in environments that have been challenging for traditional LIDAR (fog, dust) systems.

We utilize a state-of-the-art Geiger mode avalanche photodiode (GMAPD) 32X32 detecting array for imaging with an integrated fast timing circuit ROIC per imaging detector pixel. This GMAPD is equivalent to 1024 radar receivers and produces a 3-D point cloud scene for each <1nsec laser interrogation pulse. Through this work, we have demonstrated Sandia's first imaging LIDAR system. We developed significant software to scan the GMAPD array, control data acquisition, and stitch an arbitrary number of images for greater lateral spatial resolution. We designed and built an optical system to evaluate performance, in the laboratory and in field tests, and relate to the performance at tactically important distances.

Our use of this system is to study and characterize techniques that extend the range of useful imaging through fog for applications in a maritime environment. We quantify, with simulations, broad wavelength regimes and illuminating polarizations that have benefit in propagating through fog. In particular, we identify circular polarization over broad wavebands as a superior persisting signal technique in extending the useful range of active LIDAR in forward-scattering environments. Finally, we characterize the performance of our LIDAR system and confirm our theoretical predictions in the field and directly evaluate this system as a function of polarization in Sandia's medium-range Fog Tunnel Facility. This technology has potential impacts in improved ISR in maritime environments, but with further development could be revolutionary in tactical ISR by providing real-time three-dimensional full motion video (3D FMV) in DVEs.

CONTENTS

1. Introduction.....7
2. Background.....11
3. Imaging LIDAR Experimental Results.....17
4. Simulation Results: Fog and Dust Environments.....25
5. Simulation Results: Evolution in Scattering Environments.....43
6. Experimental Results: Polystyrene Microspheres in Water.....59
7. Experimental Results: Sandia Fog facility.....73
8. Conclusions.....81
References.....83
Distribution.....88

1. INTRODUCTION

LIDAR is a portmanteau of light and radar, though sometimes it is considered as an acronym of Light Detection and Ranging. Either definition is acceptable since they both suggest the product produced, a 3D survey measured by laser illumination. LIDAR has proven its usefulness in many different applications including; atmospheric remote sensing, mining, military applications, surveying, automation, and agriculture. However, LIDAR is generally prevented from working in all weather, as the traditionally used wavelengths are scattered and/or absorbed by fog, clouds, dust, and other obscurants. We have identified and quantify improved optical propagating wavelength and polarization state regimes that should open this operating window for LIDAR. This work supports airborne intelligence, surveillance, and reconnaissance for tactical situation awareness in denied environments with a modified imaging LIDAR. This will have broad impact over a range of DOE and intelligence airborne and satellite programs (e.g., SOCOM, Air Force, NRO, NASA). For example, US Special Operations Forces have identified challenges – which can be addressed within 5 years – that include LIDAR in all environments, day/night.

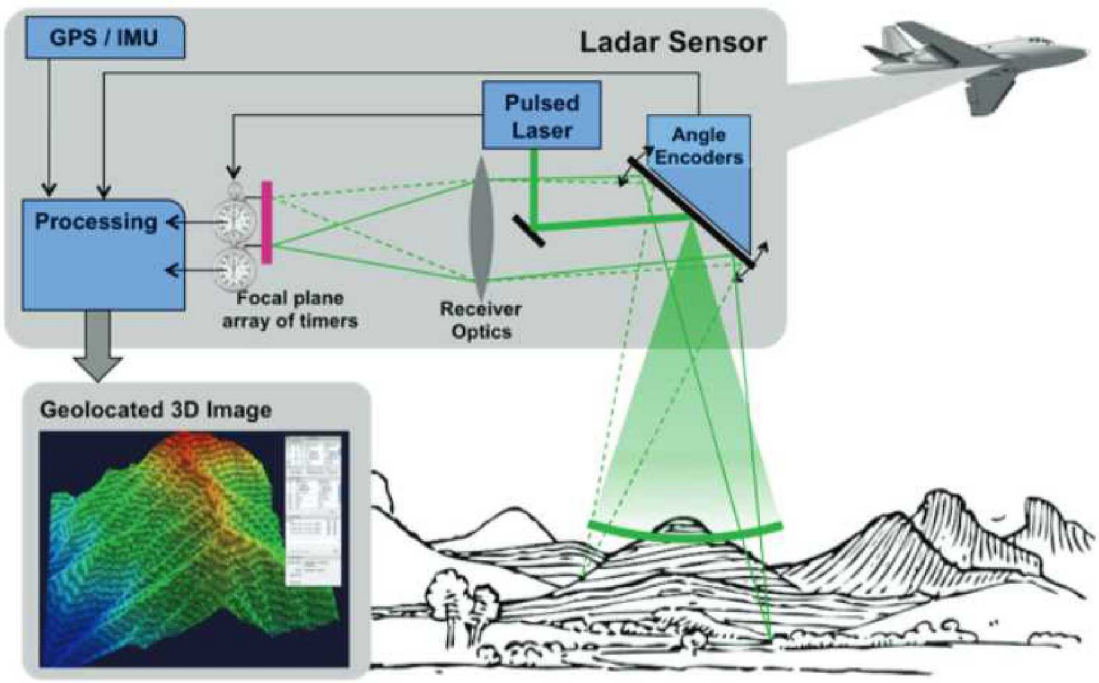

Figure 1: Typical LIDAR/LADAR setup
(https://www.ll.mit.edu/publications/technotes/TechNote_ALIRT.pdf)

This work focused on 2 regimes: 1) the operation of LIDAR in difficult scattering environments and 2) imaging LIDAR applications. This was done in order to move towards an "all-weather" LIDAR capability. Moreover, the goal was to maximize the range or signal-to-noise ratio using wavelength, polarization, illumination, waveform, or other detection discriminators.

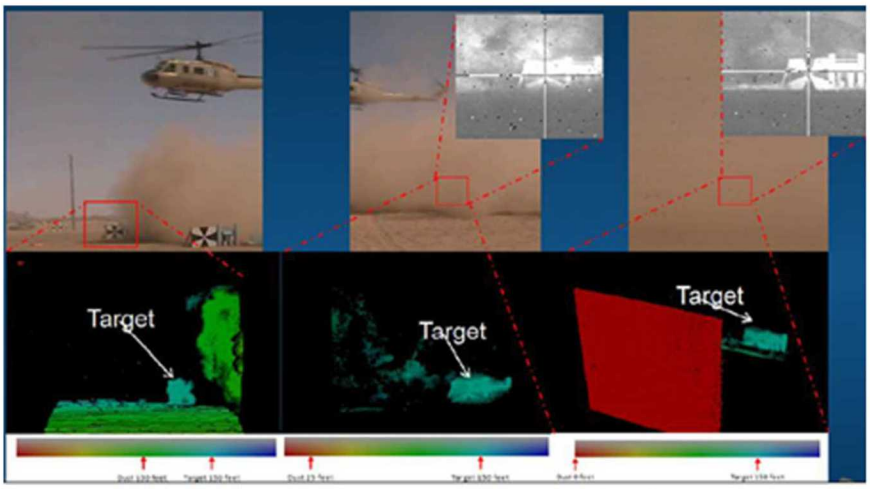

Figure 2: 3-D flash LIDAR shown penetrating through 150' of dust. Visible image is completely obscured while Flash LIDAR can provide 3-D imagery of hazards [1].

A major focus of this work was concentrated on proving via numerical simulations that circularly polarized light persists further than linearly-polarized light. Lasers used for LIDAR are traditionally inherently linearly polarized but traditional LIDAR do not utilize this property. Traditional LIDAR systems collect any and all polarized and unpolarized light. Polarized light adds an additional discriminating factor to any LIDAR system. Additionally, there has been some research showing polarized light can increase persistence and possibly range in certain scattering environments. Past research has focused on the use of linearly polarized light in laboratory scattering environment such as polystyrene microspheres in water. Until recently no research has systematically investigated the use of both linear and circular polarization over broad wavelength ranges and various scattering environments. Throughout this work we show that circular polarization has increased signal persistence through various real-world scattering environments compared to linear polarization. Increasing the amount of signal that transmits through scattering environments can enable increased range and signal-to-noise ratio. The use of polarized light, both linear and circular states, to increase range and signal to noise was thoroughly investigated through simulation in this work. In addition, a pursuit of this work was also experimental analysis of both circularly and linearly polarized light's persistence in various scattering environments. The results presented throughout this report show strong possibilities for the use of circularly polarized light in future LIDAR systems. This will enable the eventual demonstration of a polarized imaging LIDAR with improved range, detection, and identification in traditionally denied environment situations.

LIDAR is a complement to other detection technologies like synthetic aperture radar (SAR) and provides non-overlapping usage scenarios due to the fundamental physical differences in their sensing modalities. In addition, these technologies could be utilized in a single platform and provide novel multimodal sensing capabilities together.

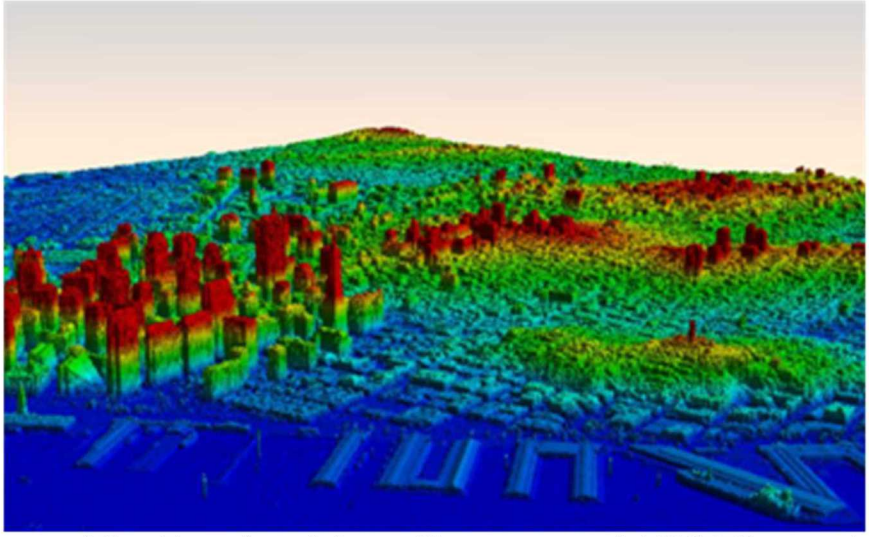

Figure 3: 3-D image of San Francisco taken with a commercial OPTEC scanning LIDAR [1].

This report is separated into three chapters. Chapter 3 provides an overview a new imaging LIDAR capability at Sandia National Laboratories. The chapter overviews the LIDAR system's hardware and software development that was built at Sandia. Extensive lens design and image analysis are included in this chapter. This chapter concludes with the first imaging LIDAR results ever performed at Sandia National Laboratories. Chapter 4 provides an exhaustive overview of polarization persistence simulation results for linear and circular polarization in various scattering environment. This chapter briefly overviews how the simulation program works and then presents the results from two journal publications. Chapter 6 provides experimental results for polarized light transmission through multiple scattering environments. The first scattering environment presented is a laboratory environments of polystyrene microspheres in water. Simulation results are presented for the same scattering environments to compare our simulation results to simulation results. Throughout this analysis a major finding was found, circular polarization is more tolerant to optical system parameters than linearly polarized light. These simulation results and their implications are included in this chapter. The second scattering environment included in Chapter 7 is the unique Sandia fog facility. Polarization persistence measurements were performed in the new Sandia fog facility. Those results are presented in the chapter as well as some simulations for a fog distribution similar to that measured in the fog facility. Lastly, Chapter 8 concludes the report.

2. BACKGROUND

Introduction

These acronyms generally mean Light Detection and Ranging or Laser Detection and Ranging; although, everyone uses a laser as the preferred source due to its maximal intensity. Sometimes LIDAR denotes aerosols measurement applications; while LADAR generally characterizes distance (along the z axis) measurement to a hard target.

Here we discuss detection and ranging, using a laser, off of a hard target. The setup and some definitions are in the figure below.

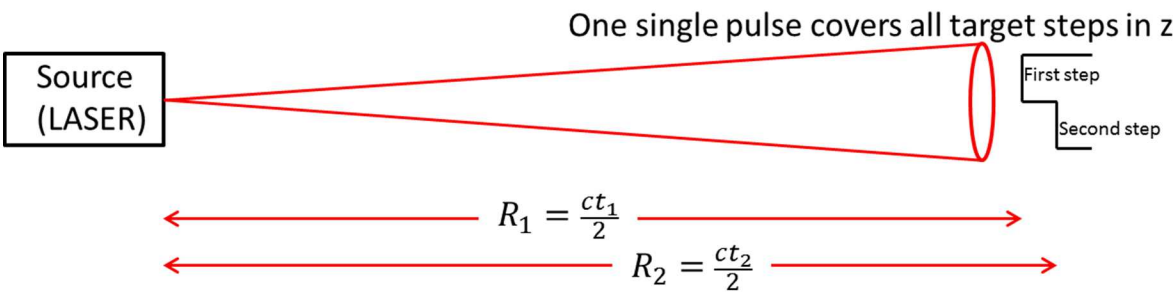

Figure 4: Layout for LIDAR over range R.

A single laser light pulse, in the shape of a diverging cone, illuminates all of the facets of the target within its cone angle. The pulse reflects off of each facet, and returns a reflection in a time that is proportional to the range (distance) between the facet and the source. An electronic circuit measures the amount of elapsed time between the laser pulse launch and each roundtrip returned pulse. R_1 is the range to the closest object step, or facet, and R_2 is the range to the next object step.

The measurement process assumes that the refractive index, and thus the speed of the light pulse, is constant over the path. A refractive index change along the path, if abrupt and of measurable difference, will return a pulse whose amplitude depends upon the delta refractive index (complex), the source divergence, the range, and the illuminating irradiance. This discussion will assume, without loss of generality, that the refractive index of the path is constant (vacuum, n=1) until the pulse illuminates the target and returns. If there is an intervening interface, an accompanying pulse will be produced and can be included using the described method.

Transmitted Pulse to the Target

We need the size of the laser beam at the target to calculate the illuminating irradiance (W/m^2) of the laser pulse at the target range. Generally the target is at a significant distance (far field) and the beam divergence is diffraction-limited.

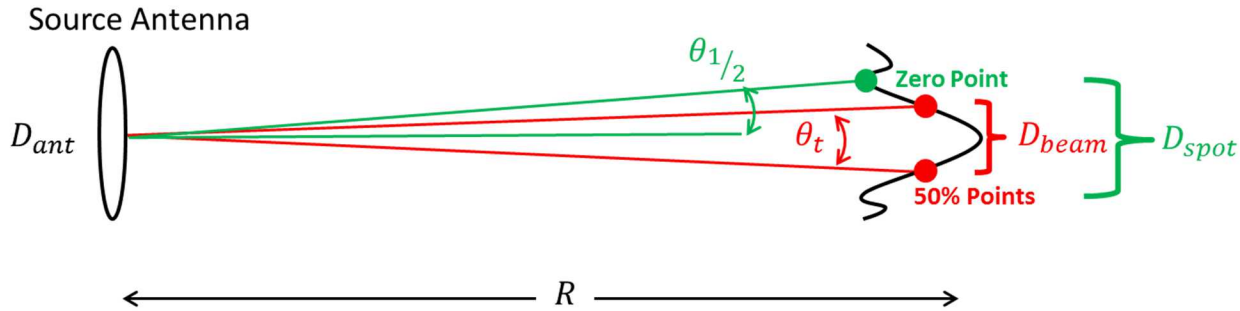

Figure 5: Source divergent angle and half-angle definitions.

From the figure, the diameter, D_{spot}, of the illuminating laser is:

$$D_{spot} = \frac{2.44\, R\, \lambda}{D_{ant}}$$

Also, for small angles:

$$D_{spot} = R\, 2\, \theta_{1/2}$$

so that the angular size of the beam is

$$\theta_{1/2} = 1.22 \frac{\lambda}{D_{ant}}$$

If we let the half angle (to the zero point) approximate the full angle to the 50% points, then

$$\theta_{1/2} = \theta_t = 1.22\, \frac{\lambda}{D_{ant}}$$

where θ_t is the (full) angular width of the transmitted beam in radians.
This means that the irradiance, in W/m^2, of the illuminating spot at the target is given by:

$$\begin{aligned} I_{at\ target} &= \frac{\tau_{atm} P_{initial}}{Area_{beam}} \\ &= \frac{\tau_{atm} P_{initial}}{\pi\left(\frac{D_{beam}}{2}\right)^2} \\ &= \frac{\tau_{atm} P_{initial}}{\frac{\pi}{4} D^2{}_{beam}} \\ &= \frac{\tau_{atm} P_{initial}}{\frac{\pi}{4}(R\theta_t)^2} \end{aligned}$$

where $P_{initial}$ is the laser source's initial power and the one-way transmission loss through the atmosphere is unitless and denoted by τ_{atm} .

Limiting Area at the Target

The power that is incident upon the target, P_{target}, and then reflected off of the target, P_{refl}, is given by:

$$P_{refl} = \rho_{target}\, I_{at\ target}\ Area_{target\ limit}$$

and is a function of the target's limiting area. This area is determined by the smallest angular subtense of 1) the illuminating beam, θ_t, 2) the target, γ_{tar}, or 3) the reciever's instantaneous field of view (FOV), γ_l. Here $Area_{target\ limit}$ is the projected area at the target.

1) If the illuminating beam angular subtense, $\theta_t = \frac{1.22\lambda}{D_{ant}}$, is the smallest, then for the limiting area, use:

$$Area_{target\ limit} = Area_{beam} = \pi\left(\frac{D_{beam}}{2}\right)^2 = \frac{\pi}{4}(R\ \theta_t)^2$$

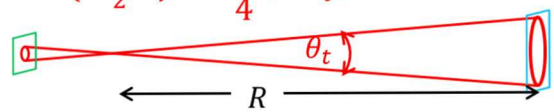

2) If the target angular subtense, $\gamma_{tar} = \frac{target\ width}{R}$, is the smallest, then for the limiting area, use:

$$Area_{target\ limit} = (R\ \gamma_{tar})^2$$

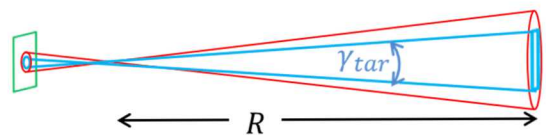

3) If the receiver IFOV angular subtense, $\gamma_l = \frac{\Delta}{f}$, is the smallest, then for the limiting area, use:

$$Area_{target\ limit} = (R\ \gamma_l)^2$$

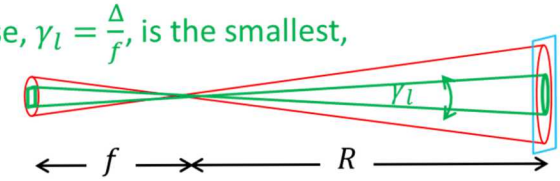

Figure 6: Limiting areas and solid angles for LIDAR.

Reflected Pulse Back at the Receiver

The irradiance back at the receiver will be

$$I_{rec} = \frac{\tau_{atm} P_{refl}}{\Omega_{targ}\ R^2}$$

Where Ω_{targ} is the solid angle that the target emits into. The solid angle (in steradians) ranges from the square of the specular angle (from a shiny target) to pi steradians (from a Lambertian, diffuse target): $\theta_t{}^2 \leq \Omega_{targ} \leq \pi$.

Finally, what is the power coupled into the antenna aperture of the receiver?

$$P_{rec} = I_{rec}\ \ Area_{RecAper} = I_{rec}\left(\frac{\pi}{4}D^2{}_{RecAper}\right)$$

$$= \frac{\tau_{atm}}{\Omega_{targ}\ R^2}\ \ P_{refl}\ \left(\frac{\pi}{4}D^2{}_{RecAper}\right)$$

$$= \frac{\tau_{atm}}{\Omega_{targ}\ R^2}\ \rho_{target}\ \ I_{at\ target}\ \ Area_{target\ limit}\left(\frac{\pi}{4}D^2{}_{RecAper}\right)$$

$$= \frac{\tau_{atm}}{\Omega_{targ}\ R^2}\ \rho_{target}\ \frac{\tau_{atm} P_{initial}}{\frac{\pi}{4}(R\theta_t)^2} Area_{target\ limit}\left(\frac{\pi}{4}D^2{}_{RecAper}\right)$$

$$= \frac{\rho_{target}\ \tau^2{}_{atm}\ \ P_{initial}}{\Omega_{targ}\theta_t{}^2\ R^4}\ \ Area_{target\ limit}\left(D^2{}_{RecAper}\right)$$

Results for Illuminating Beam as Limit

The following results are valid for these parameters:

The transmitting source antenna diameter is 0.1 m,
The source wavelength is 1.06 microns,
The initial laser power is 1000W,
The transmission efficiency throug the atmosphere is 1,
The target is lambertian with a reflectivity of 0.25,
And the receiving aperture diameter is 0.15m.

Figure 1 shows the diameter of the illuminating transmitted laser source as a function of several relevant target ranges (not linear) from 10 meters to 5000 kilometers (dark red curve with astericks markers). Also on the figure is the resulting irradiance (green curve with cross markers) at that target in W/m^2. We can see by the dark red curve that the assumption where the angular spread of the illuminating beam is the smallest limiter (smaller than the object angular size or the field of view) defining the "target size" is good out to a range of 1000km for a target diameter of about 10m. Even so, the irradiance of the transmitting beam has dropped to less than 10 W/m^2 at this range. In this log graph, we can see that the irradiance goes as the square of the range and the beam diameter is linear with the range.

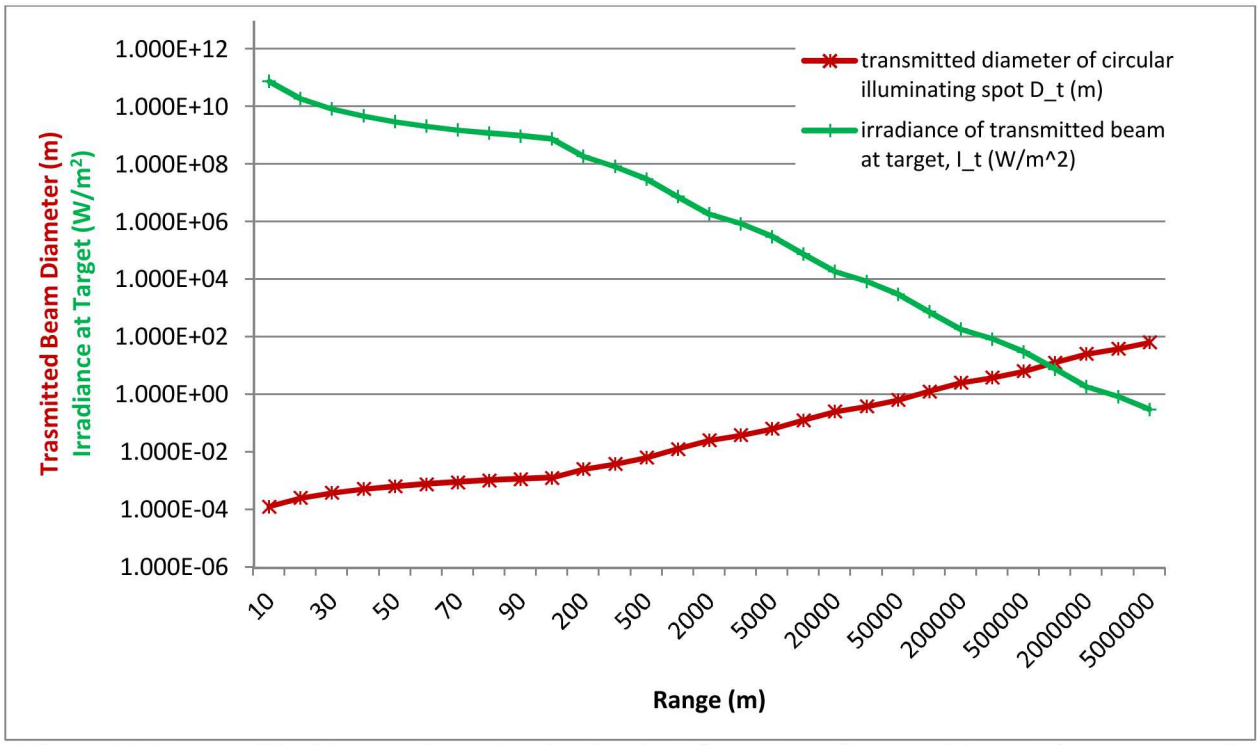

Figure 7: Transmitted beam diameter (red asterix) and irradiance at target (green cross) as a function of propagation distance (range).

The dark red transmitted beam diameter curve is also shown in Figure 2 below. Now we also see two other curves, as a function of the same range values. The blue curve with triangle markers shows the irradiance back at the receiver (in W/m2) given that the reflectance of the target is lambertian (the solid angle containing the emittance is pi steradians) with a reflectivity of 25%. Finally, the magenta curve with the circle markers is the collected power by the receiver for a collecting circular diameter aperture of 0.15m. An order of magnitude lower limit for power is 1

microwatt for a linear diode detector; thus the limiting range of an objects range is 1 km. We could extend this with more sensitive, nonlinear detectors such as avalanche photo diode detectors (APDs) to an order of magnitude lower power limit of 1 nanowatt. This extends the measurable range out to 50 km. Other range extenders might be to increase the initial transmitting power of the source and/or increase the collecting aperture diameter at the receiver. Ultimately, this configuration is disadvantaged by the diffracting beam divergence, particularly after the target reflection. This divergence is not easily controlled since there will not be optics to re-converge the beam after target reflection. Utilizing a longer source wavelength will help us to limit the divergence as a function of range. Finally, a passive configuration, where the target is the "source" and thus not susceptible to the two-way source range, is also a potential approach. Here, we can rely on infrared source radiation, which is long wavelength and thus less divergent, but at low power. This requires a cooled detecting scheme – possibly imaging detection, so that the target can be distinguished from other thermal sources within the scene.

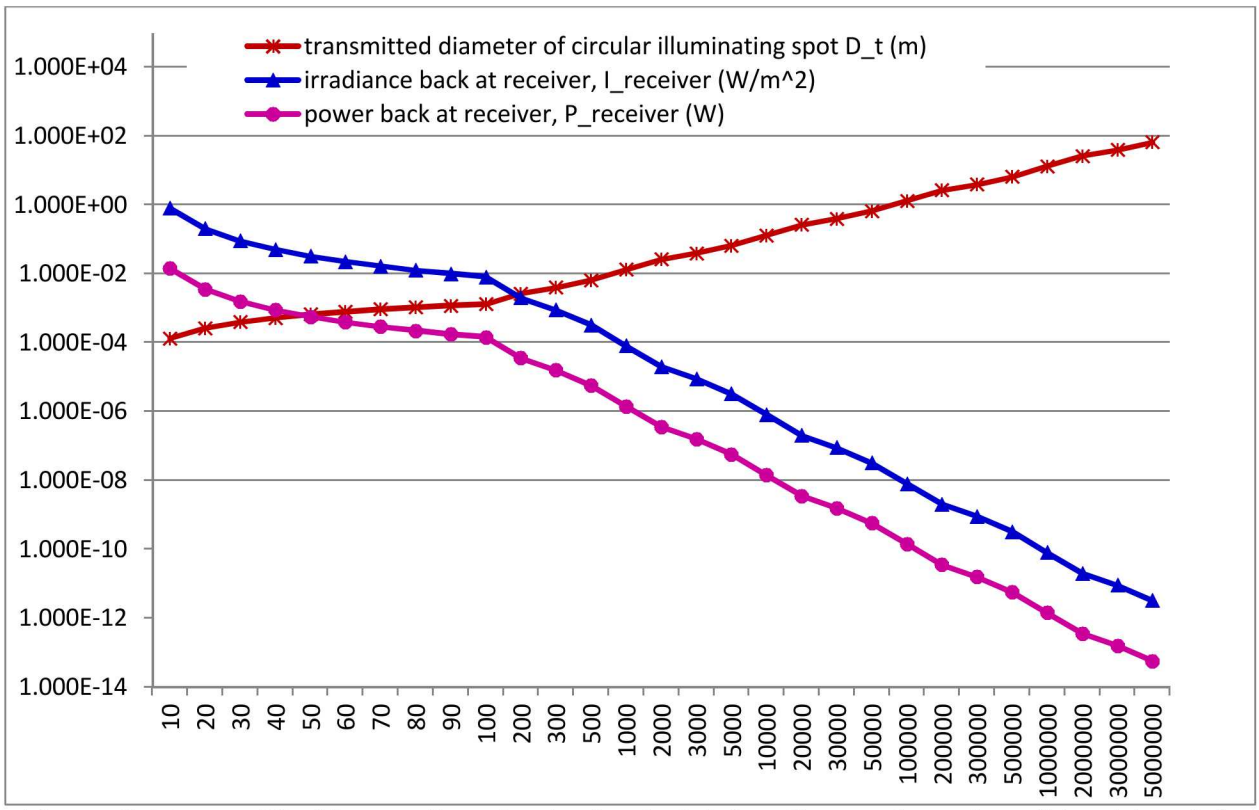

Figure 8: Transmitted beam diameter (red asterix), irradiance at receiver (blue triangle), and power at receiver (magenta circle) as a function of propagation distance (range).

Finally, Figure 9 below shows all of the results on one graph, as a function of the selected range values.

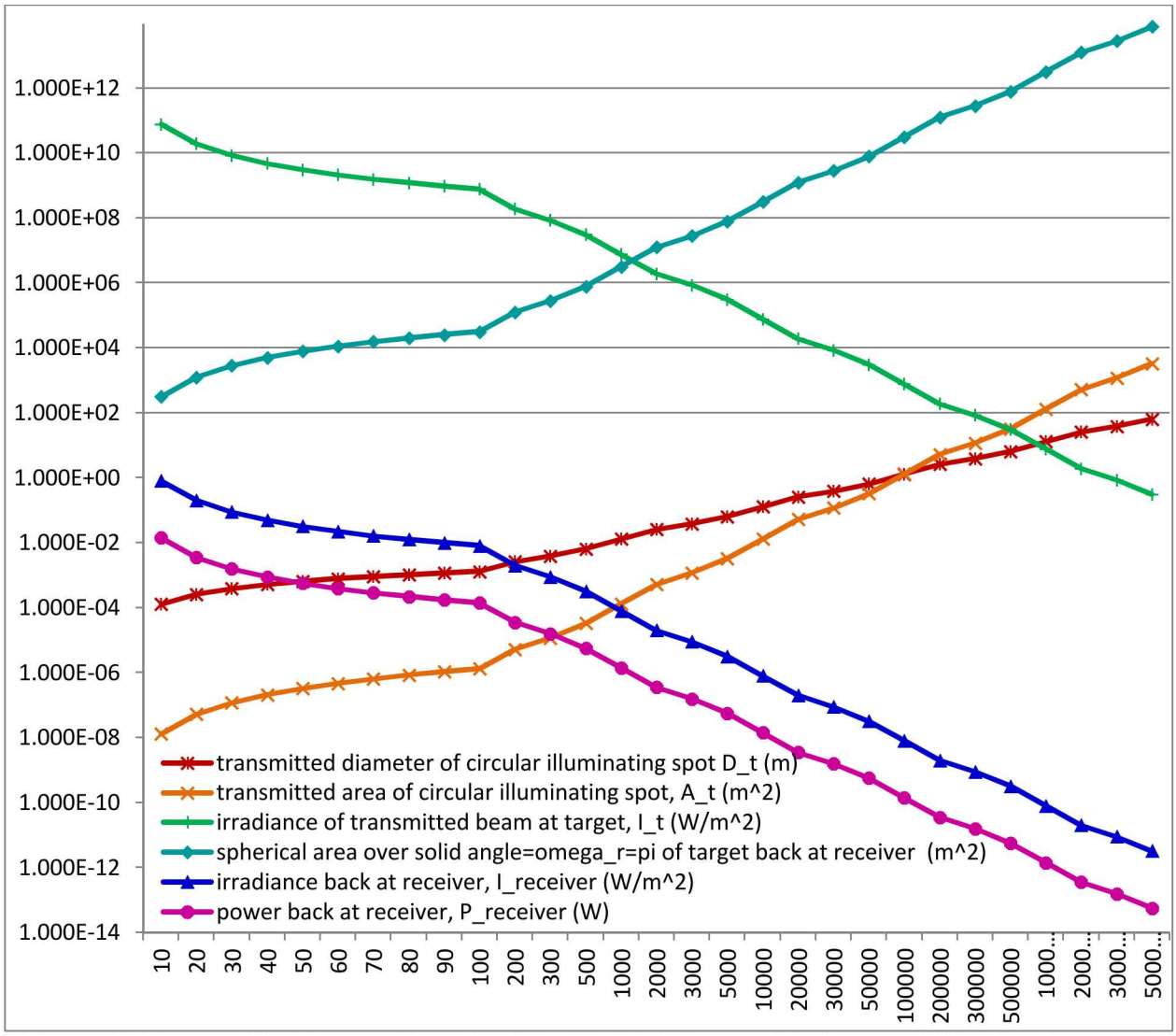

Figure 9: Transmitted beam diameter (red asterix), transmitted area of illuminating spot (orange x), irradiance at target (green cross), spherical area over solid angle at receiver (teal diamond), irradiance at receiver (blue triangle), and power at receiver (magenta circle) as a function of propagation distance (range).

3. IMAGING LIDAR EXPERIMENTAL RESULTS

Introduction:

The following chapter is a description of the imaging LIDAR that we built for this LDRD. It represents a new capability for Sandia in the realm of imaging LIDAR.

Section 1: System Overview and Design

1. Introduction:

Imaging LIDAR captures a 3D dataset from a single laser pulse, whereas traditional LIDAR requires the use of a scanning system to raster the beam over an area rather than a single point (3D vs 1D). Imaging LIDAR can be accomplished by a number of different means including fast gated cameras (Flash LIDAR), synthetic array heterodyne detection, and Geiger Mode Avalanche Photodiode (GMAPD) arrays. In recent years the GMAPD has been of great interest due to its compact size and improved accuracy.

The system we constructed for the project uses a GMAPD array from Boeing/Spectrolab. The array is comprised of 32x32 individual avalanche diodes bonded to a custom ROIC that can time each detector independently. Further information on the device can be found in reference [2].

2. System Overview

The system we designed for this project used the GMAPD described in Section 1. In order to collect data this imager was combined with other components to create a LIDAR. The principle operation of the system is to send out a laser pulse to illuminate the scene and then image the scene onto the detector, while timing the delay between the pulse being emitted and collected. The source we used for this system was an Ytterbium doped fiber laser (Fianium HE-1060). This laser is a mode-locked fiber laser with a 100 ps pulse with 10 μJ of energy. The laser system includes a pulse picker so that the repetition frequency can be tuned (single shot – 200 kHz); while this was practical for our test platform it would be better to use a fixed pulse repetition frequency laser for a practical system design. The short pulse of the laser is also a necessity since the depth resolution is entirely dependent on the pulse width and the timing resolution of the detector. A schematic of the system is shown in Figure 10. As can be seen from the figure the illumination and the imaging system do not share an optical system. This was done to reduce complexity and costs. However, there are numerous realized commercial system that have implemented shared optical systems for illumination and collection. For the illumination of the bench top, the laser beam was passed through an engineered laser diffuser which decollimates the beam to a uniform and square intensity profile. In a deployed system this technique would not be feasible due to the inefficiency of spreading the light so quickly, but it is very useful for lab characterization and gives a uniform illumination to characterize system performance with.

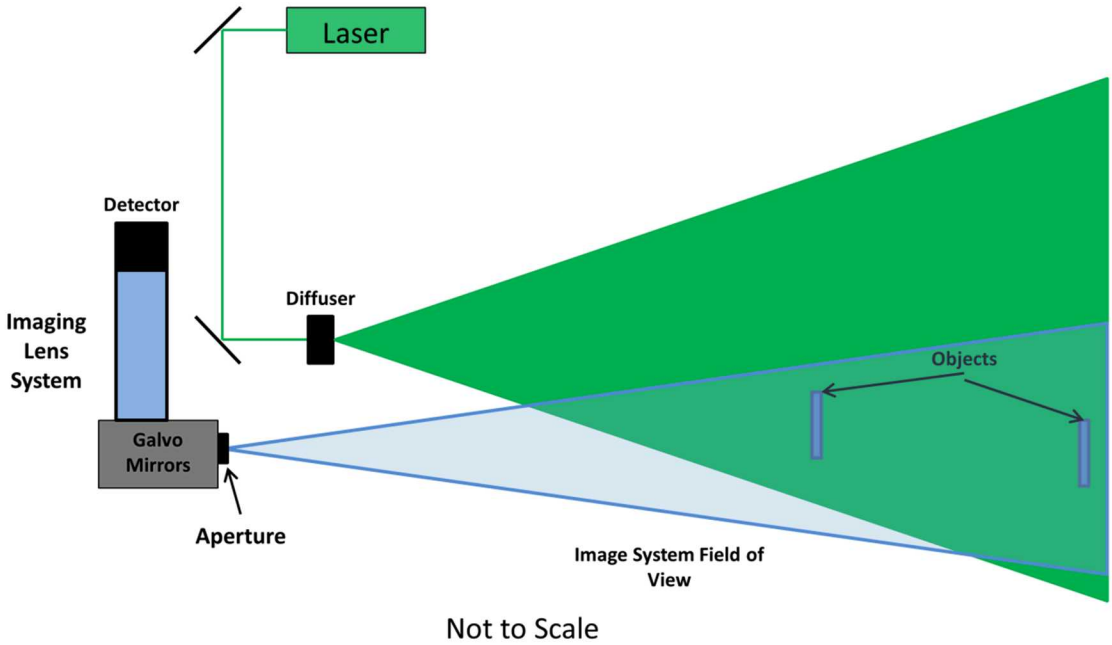

Figure 10: Benchtop LIDAR schematic showing the laser illumination and separate imaging GMAPD LIDAR detector.

Light from the scene is collected through an adjustable aperture and then steered via a dual-axis scanning galvanometer positioning system. This effectively allows the detector to scan over the area of interest and collect light over a 25 degree × 25 degree scan. The galvanometer we used was a commercially available system from Thorlabs (GVS112) that has a mechanical scan angle of ±20° and is controlled by an analog position voltage. Small steps can be made in 400µs, this means that a portion of the frames must be removed from the cameras stream or blurring will occur. (The camera captures a frame every 50µs.)

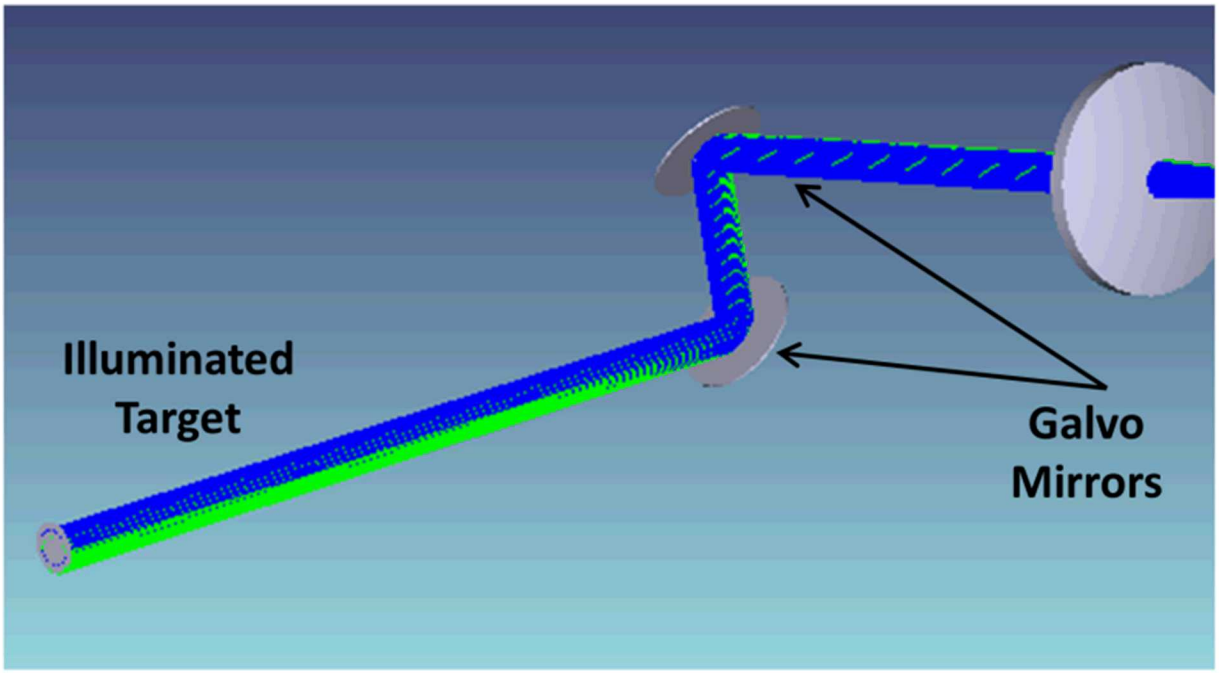

Figure 11: 3D representation of the galvanometer steering mirrors.

After the galvanometer, the collected light passes through an optical system so that the formed image can be magnified on the detector. The optical system consisted of a magnifying telescope and an imaging lens. A Keplerian telescope with a magnification of 2x was used. The telescope has two optics, a 50 mm focal length bi-convex lens and a 25.4 mm focal length bi-convex lens, these optics are spaced 75 mm apart. The magnified rays from the telescope are imaged to the detector plane using a 75 mm bi-convex lens. With this optical system the LIDAR achieved an instantaneous full field of view of 1 degree. Using the Galvo system the effective full field of view is 25 degrees in each direction.

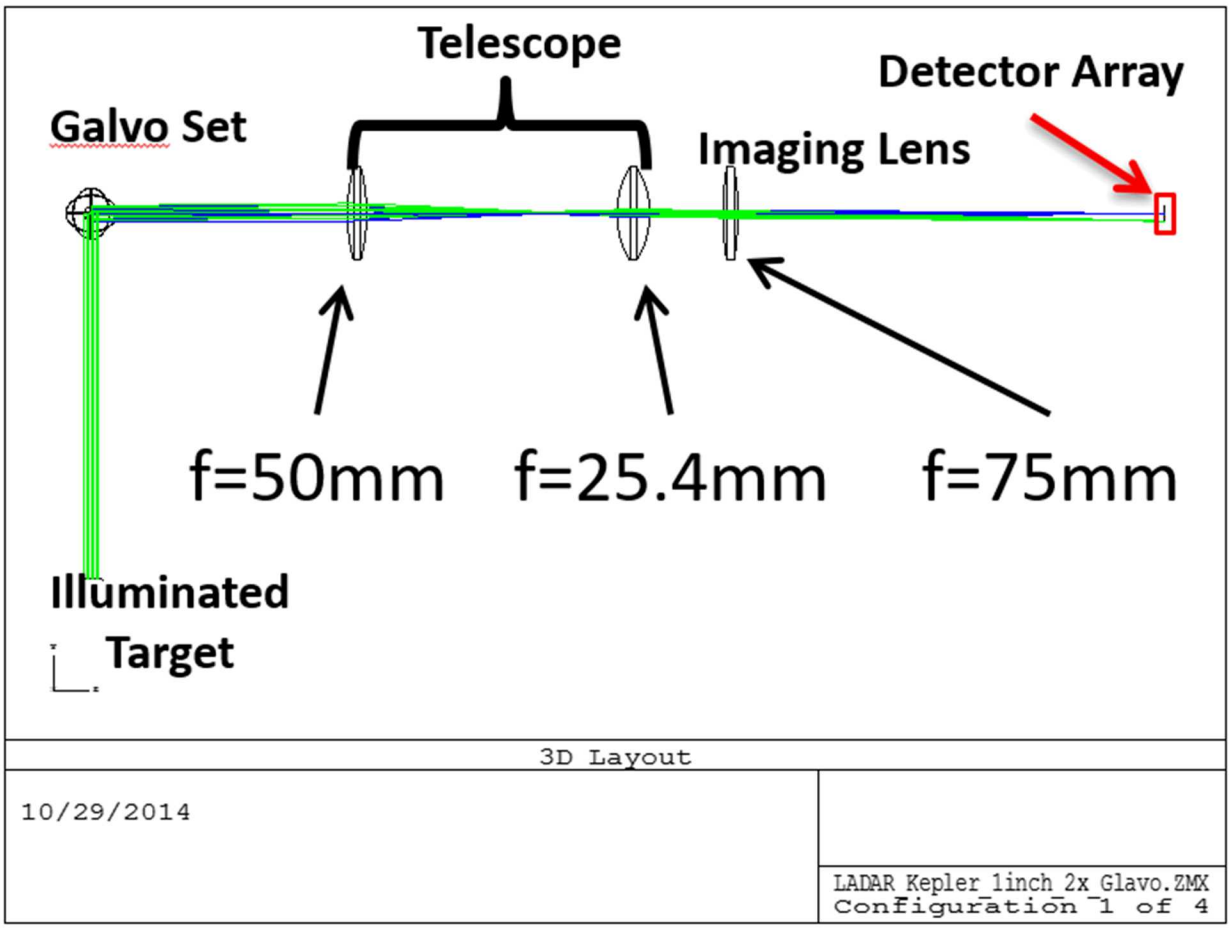

Figure 12: Optical system design.

To quantify the possible system performance, we simulated the performance of the imaging system viewing a resolution target at various distances. The distances we investigated, that were relevant to laboratory measurements, were 74 in., 119 in., 162 in., 234 in., and 780 in. For the simulation we chose 30 mm square bars from an Airforce 1951 resolution target. The target is shown in Figure 13 with the chosen portion highlighted.

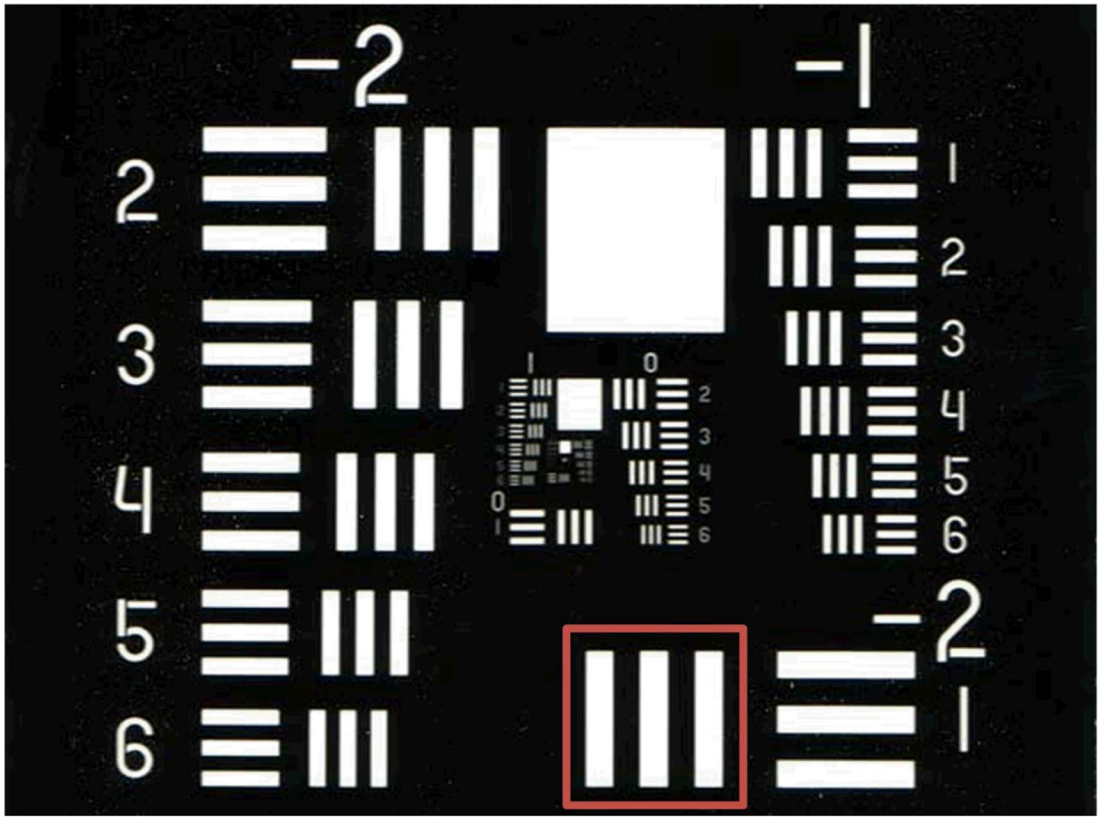

Figure 13: AF1951 resolution target with the region used for simulation highlighted.

We found that the performance of this simple system would be acceptable for laboratory testing of the detector and would also be acceptable for testing in long corridors (< 500 ft.), like Sandia's fog tunnel. The performance of the optical system for a distance of 74 in. is shown at the top of Figure 14. The original object rendered with a 500 × 500 pixel resolution is shown on the left. In the middle is how the object would appear at the imaging plane through the optical system rendered with a 500 × 500 pixel resolution. On the right is simulative of what the detector would see with a 40 × 40 pixel resolution. The detector is made of an array of 32 × 32 pixels, however the 40 × 40 corresponds to the correct pixel pitch and the image would overfill the detector. The performance for a target at 780 in. is shown at the bottom of Figure 14. The figure shows that while the optical system maintains the desired resolution, the system performance is limited purely by the detector since the pixel spacing is so large. At 780 in. the bars cannot be resolved. However, this performance would likely not be a requirement for a fielded system.

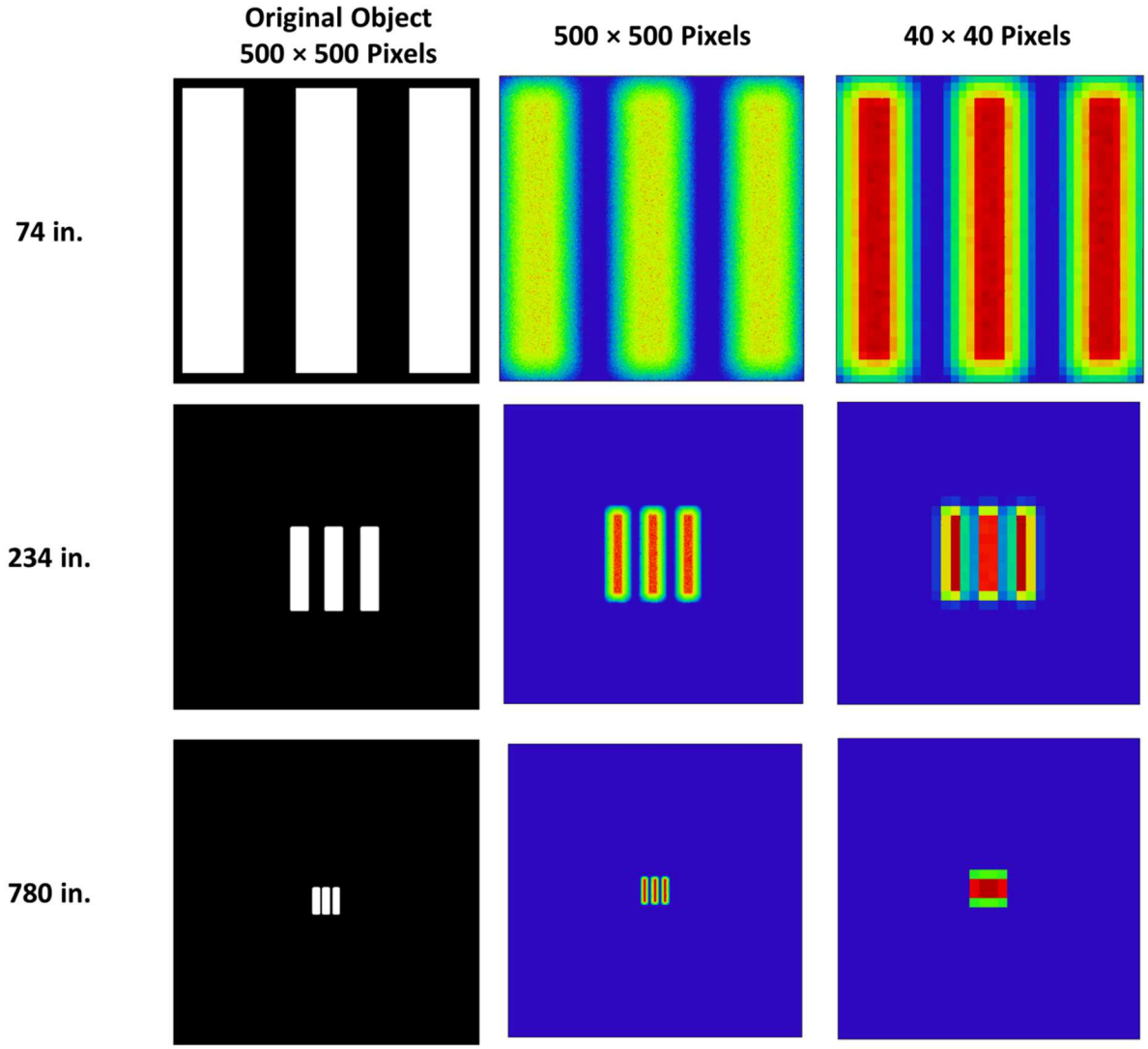

Figure 14: Simulated results of imaging at various distances. An ideal image is contrasted to the image formed by the detector.

Our camera included a camera link interface to transmit images to the computer as well as for control of the detector. This camera was supplied to Sandia from the manufacturer with software that allowed for capturing simple images. However, our desire was to create a system that could control the camera and capture images with the galvanometer in an automatic fashion. We therefore chose to explore a custom camera interface. The interface we designed allowed the user to preview the raw image feed from the camera or in a raster fashion acquire a series of images. The raster was achieved by supplying the 2d scanning galvanometer with 2 DC voltages; one for vertical scan, the other for horizontal. The voltages were generated by a National Instruments DAC/ADC board. Our software was coded in C# and employed the Sapera Application Programmers Interface (API) for camera control/data acquisition and the NI-DAQmx API to control the galvanometer. A separate program was produced by the team to post-process the acquired imagery by averaging and filtering multiple frames into a single intensity/depth data set and then tile multiple frames together to create a higher resolution image than what the camera

natively supported. An example data collection can be seen in Figure 15. Here the custom made (laser cut black anodized foil) resolution target was scanned with the system. The data stream was then displayed in a tiled format. This data shows the accumulated counts equivalent to an intensity image from the data collection.

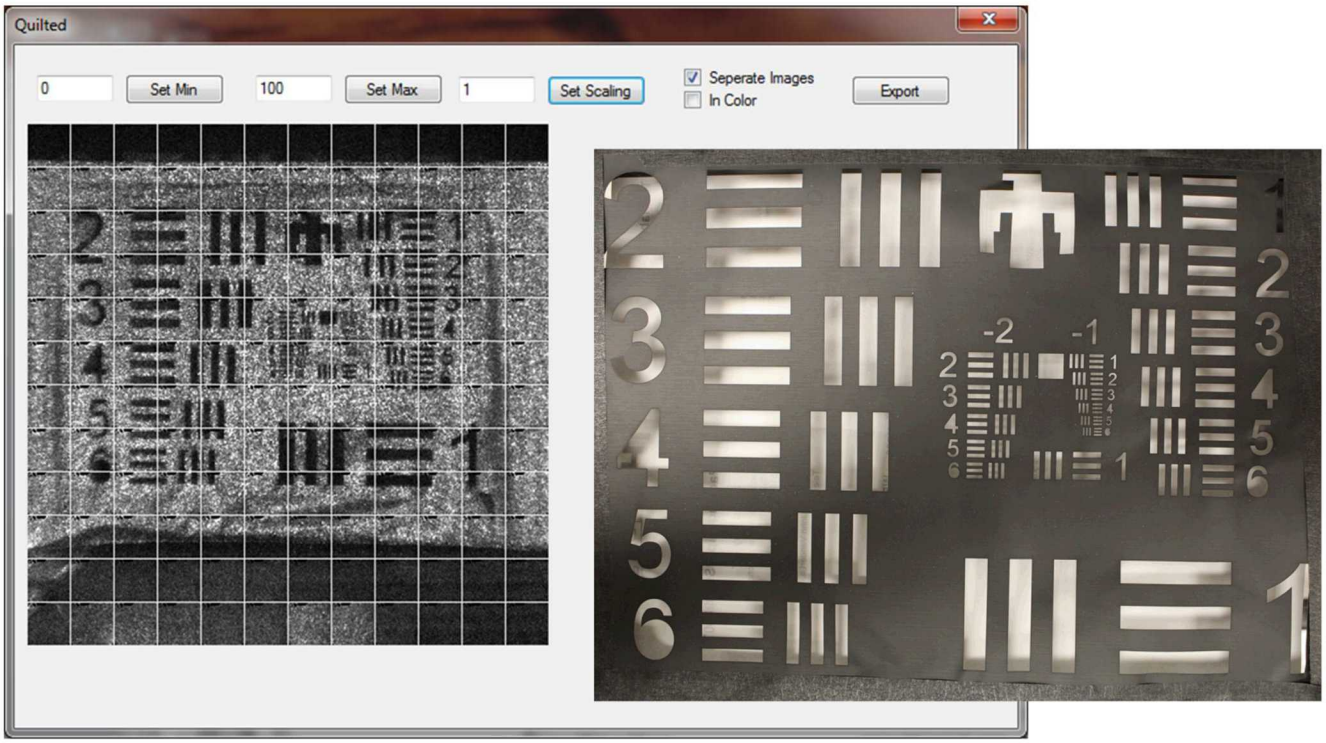

Figure 15: Experimental system performance at 74 in. shown with a photograph of the measured target. The target was laser cut at Sandia.

After testing the LIDAR system in the lab we moved to a more realistic testing environment in the Sandia fog tunnel facility. This facility is a 180 ft. long tunnel that can generate a fog like aeresol that simulates fog conditions for optical testing. As part of our project we upgraded the fog tunnel to support Class IV laser operations with a physical barrier and laser interlock system. Initial testing of our LIDAR system showed excellent ranging resolution in the tunnel with adequate imaging. One of the resulting tests is shown in Figure 16, where a number of target were placed at various distances away from the detector. It is easy to make out the targets at close range including the elements with different reflectivities. In addition, at the top of the image we see the cross support members of the roof of the tunnel with resolved distance and the expected perspective of the imaging system. The image is made of a 12 × 12 stitch of individual galvanometer positions. At each position 1000 frames were collected at 20kHz. Future work will focus on implementing our range extension technology using polarization to use in the fog simulator.

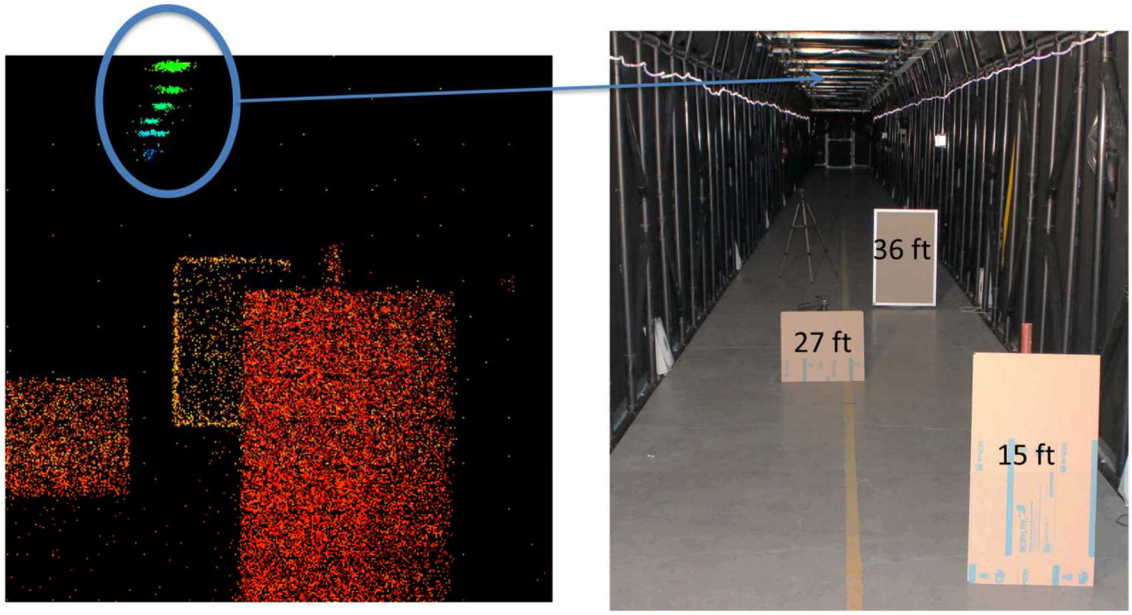

12x12 stitched range image
15ft -150ft

Figure 16: Experimental system testing with appreciable range in the fog tunnel. Targets are placed from 15-150ft. The image on the left is colored by distance away from the detector.

4. SIMULATION RESULTS: FOG AND DUST ENVIRONMENTS

Introduction:

In order to understand the physics behind the scattering of light in scattering environments such as fog and dust a rigorous simulation was designed. Results from this simulation platform for various scattering environments were performed and are presenting in this chapter. A brief overview of how the simulation works is presented in Section 1. Section 2 shows polarization persistence simulation results for a broad range of wavelengths through scattering environments of fog and dust. This section shows that circularly polarized light persists better than linearly polarized light over a broad range of infrared wavelengths for both fog and dust scattering environments. Section 3 shows simulation results for the evolution of polarized light in both isotropic and forward scattering environments. This section delves into the physics of why circular polarization persists superiorly compared to linearly polarized light in forward scattering environments.

These simulation results show the benefits of utilizing circular polarization in order to increase signal-to-noise in a LIDAR system, and thus increasing detection range.

Simulation Background:

The following simulation results were performed with a polarization-tracking Monte Carlo program. A brief overview of the simulation process with be described here in Section 1. For an exhaustive explanation of the polarization-tracking Monte Carlo program please see Ramella-Roman's Optics Express paper [3], as well as John van der Laan's graduate dissertation [4].

The simulation is very similar to a typical Monte Carlo program with one major exception, each photon's polarization state is defined by a Stokes vector which is then tracked throughout the Monte Carlo scattering process. An example of the polarization tracking Monte Carlo program is shown in Figure 17 below.

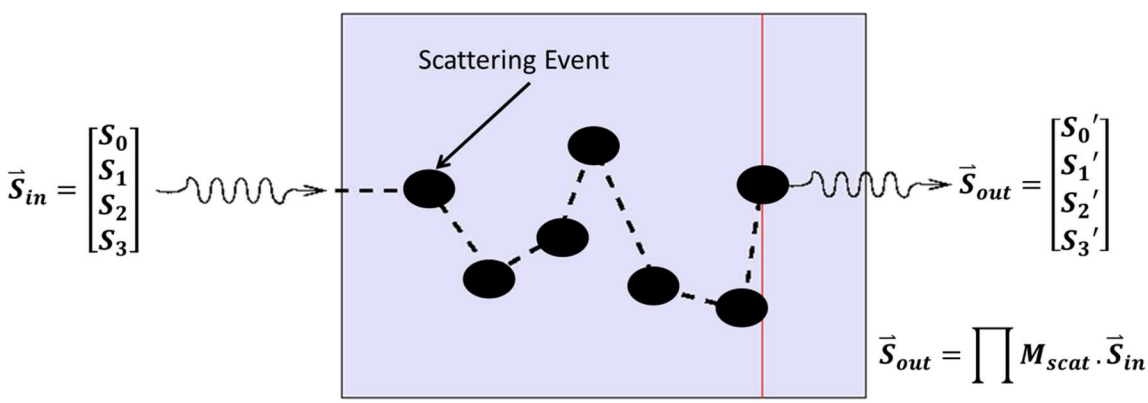

Figure 17: Polarization tracking Monte Carlo

The polarization state of the incident photons is tracked and updated after each scattering event in the simulated scattering environment. The photons are moved and when a scattering event occurs the Mueller matrix for the scattering event modifies the polarization state of the photon. This process is repeated until the photon is either reflected out of the back face of the scattering environment or transmitted through the front face of the scattering environment. The resulting

Stokes vector for either reflected or transmitted light is the result of the product of all these scattering events and thus Mueller matrix calculations. There are a number of key calculations performed during this process that are necessary to generate valid results. All of the detailed information on the simulations can be found in the previous citations mentioned.

Results

The following consists of work published in an Applied Optics paper titled "Detection range enhancement using circularly polarized light in scattering environments for infrared wavelengths" [5].

1. Introduction

Polarized light propagation in scattering environments has been of recent interest where polarization sensing techniques increase range and contrast in these environments. Polarization offers an added variable to a sensing system that can be manipulated, to better discriminate a target from a scene and sense to greater depths in scattering environments. Previous research often has developed simulations and experiments utilizing polystyrene microspheres, milk, or tissue phantoms in water as the scattering environment of interest. Passive and active incoherent, polarizing systems in underwater environments use both linear and circular polarization to reduce the effects of scattering [6]–[8]. More recently, Tyo analytically showed a narrower point spread function (PSF) due to the intensity difference between the squared linearly-polarized field components compared to the sum of the squared linearly-polarized field components. The convolution of this narrower PSF leads to improved spatial resolution in the image plane in polarization difference imaging configurations [9].

Silverman, et al. showed a factor of 2 – 3 increase in contrast using an active 544 nm polarization-modulated laser while imaging through 1 micron latex spheres in water. They investigated both linear and circular polarization showing better contrast with circular polarization [10]. Similarly, Dubreuil et al. investigated increased contrast with linear and circular polarization methods in varying concentrations of milky water solutions with polarization maintaining and depolarizing objects using a He-Ne laser for illumination [11]. Sankaran, et al. looked at both circular and linear polarized light persistence through 1) three different sizes of polystyrene microspheres (0.107, 0.48, and 1.072 microns) in water, 2) a tissue phantom with polystyrene spheres ranging from 25 to 675 nm, and 3) several samples (porcine fat blood, tendon, heart, and artery tissue) at a wavelength of 632.8 nm. Circular polarization was shown to persist for larger particle sizes of microspheres but not for all tissue samples [12], [13]. Through simulations and experiments Bartel et al. investigated the characteristics of 543 nm polarized light backscattered from polystyrene microsphere solutions with diameters of 204 nm and 2040 nm, specifically producing full backscattered Mueller matrices for the solutions [14]. Lewis, et al. published target contrast advantages of a factor of 4 for circular polarization-difference imaging versus linear polarization and a factor of 20 for circular polarization-difference imaging versus intensity imaging. They used 0.1 micron polystyrene spheres in water with a single active illumination wavelength of 632.8 nm [15]. Kartazayeva, et al. similarly investigated imaging techniques utilizing circular and linear polarization through large-diameter (10.143 microns) and small-diameter (0.202 microns) polystyrene particles with an active illumination of 632.8 nm, showing a factor of 3 increased contrast for circular polarization imaging versus linear polarization imaging [16]. Bicout, et al. showed through simulations and experiments that circular polarization persisted further than linear polarization for size

parameters of 2.69, and 5.89 of latex spheres in water [17]. Ishimaru, et al. produced similar results for a size distribution of latex particles (~ 2 microns) in water with a single illuminating wavelength of 530 nm [18].

Most of these previously published works are experimental measurements, utilizing a distinct, visible illuminating wavelength in a water environment. Three of these efforts include simulation. In contrast, our simulation research identifies broad wavelength ranges that demonstrate circular polarization's superiority in particle size and refractive index parameter sets that realistically model fog and dust in the atmosphere. Recently, Miller, et al. utilized circular polarization difference imaging techniques to increase image contrast in laboratory-generated fog scenes; however, his work was also limited to a single visible illuminating wavelength [19]. Fade, et al. experimented in outdoor fog conditions imaging a polarized incandescent source but only utilized linear polarization for both illumination and detection [20]. These recent publications add to the previously published work in this area but are still limited in their incident illuminating wavelengths. Our simulations remain unique in that they involve broad wavelength ranges and identify circular polarization's role in realistic environments, through particle size and refractive index parameter ranges.

All sensing techniques using polarization in scattering environments rely on the polarization persistence of light, often called polarization memory. Techniques typically utilize the effect of a difference between the illuminating polarization that persists to the target and the polarization response of the scattering background [21]. Circular polarization is of increasing interest due to its potentially superior persistence in scattering environments. The mechanism behind circular polarization's superior polarization persistence has been analytically explored by Xu and Alfano. They hypothesize that the two mechanisms that depolarize circularly polarized light, and therefore affect its persistence, are the randomization of the photons direction and the randomization of the helicity. They find that circular polarization persists superiorly for large particles with refractive indices close to the air environment (refractive index ~ 1) and for small, high-index contrast particles (refractive indices between 1.5 and 2) [22].

To date, no research has simulated or experimentally shown circular polarization's persistence benefits over broad wavelength ranges and over broad sensing environments. The majority of currently available experimental and simulation results, characterizing circular polarization, is limited to select wavelengths, typically in the visible spectrum, and utilizes underwater scenes with varying concentrations of polystyrene microspheres, milk, or tissue phantoms as scattering objects. In this work we quantify a broad wavelength response through infrared wavelength ranges in multiple scattering environments where circular polarization sensing outperforms linear polarization.

Using Monte Carlo simulations, we model particle sizes and refractive indices representative of fog and dust at infrared wavelengths. The persistence of circularly polarized light versus linear is shown for transmission through environments of fog and dust. Reflection results for these environments can be found in our previously published conference paper, with results that confirm these transmission results [23]. The persistence of circular polarization in scattering environments can be exploited to improve sensing and imaging range in scattering environments, important to many critical applications.

This article is organized as follows: Section 2 covers the background of polarization and the polarization Monte Carlo simulations, including validation of the simulation's performance against previously published work, Section 3 describes the environments of interest and the parameters used for each set of simulations, Section 4 presents the transmission results for each

of the environments of interest for wavelengths ranging from 0.9 to 12 microns (encompassing short-wave infrared, SWIR, mid-wave infrared, MWIR, and long-wave infrared, LWIR) for fog and 2.5 to 12 microns (encompassing MWIR and LWIR) for dust, and Section 5 concludes showing circular polarization persists better than linear polarization for certain scattering environments in all of earth's atmospheric infrared transmissible regions: SWIR (0.9-2.5 microns), MWIR (3-5 microns), and LWIR (8-12 microns).

2. Background

Traditionally, when sensing in scattering environments, the use of longer wavelengths (over visible wavelengths) is preferred due to the decrease of the scattering cross-section of the particles with increased wavelength [24]. The longer wavelengths increase the number of particles that are considered in the Rayleigh scattering regime where scattering is isotropic. As a result, infrared wavelengths are considered superior to visible wavelengths in scattering environments of smaller particle sizes and smaller optical thicknesses. For highly scattering environments with large optical thicknesses all wavelengths are detrimentally affected [25]. In order to accurately sense targets in these challenging environments, all discriminating optical parameters should be utilized. One such optical parameter, beyond the intensity and wavelength of light, is its polarization.

Polarization is defined by the oscillation plane of the electric field vector as a function of wave propagation direction. The polarization of light is described by the Stokes parameters which are a part of the 4x1 Stokes vector,

$$\vec{\boldsymbol{S}} = \begin{bmatrix} S_0 \\ S_1 \\ S_2 \\ S_3 \end{bmatrix} \propto \begin{bmatrix} I_H + I_V \\ I_H - I_V \\ I_{45} - I_{135} \\ I_R - I_L \end{bmatrix}, \tag{1}$$

where S_0 is the total intensity of the light, S_1 is the difference between linear horizontally polarized and linear vertically polarized flux, S_2 give the difference between the linear 45° polarized and linear 135° flux, and S_3 gives the difference between right and left circularly polarized flux [26]. A general Stokes vector is made up of a combination of a purely polarized portion and a completely unpolarized portion. The percentage of the total intensity that is purely polarized is defined as the Degree of Polarization (DoP).

$$DoP = \frac{\sqrt{{S_1}^2 + {S_2}^2 + {S_3}^2}}{S_0} \tag{2}$$

The DoP can vary between 0 (completely unpolarized light) to 1 (purely polarized light). Any Stokes vector with a DoP between 0 and 1 is partially polarized and can be separated into its purely polarized and unpolarized Stokes vectors shown in Equation 3.

$$\vec{\boldsymbol{S}} = \vec{\boldsymbol{S}}_{polarized} + \vec{\boldsymbol{S}}_{unpolarized}$$

$$= \begin{bmatrix} \sqrt{{S_1}^2 + {S_2}^2 + {S_3}^2} \\ S_1 \\ S_2 \\ S_3 \end{bmatrix} + \begin{bmatrix} S_0 - \sqrt{{S_1}^2 + {S_2}^2 + {S_3}^2} \\ 0 \\ 0 \\ 0 \end{bmatrix} \quad (3)$$

In highly scattering environments, photons are multiply scattered and, as a result, their polarization is modified. Individual photons polarization states are randomized through the scattering process and the resulting transmitted polarization state is subsequently depolarized. Our goal in this work is to investigate where circularly polarized light's persistence in highly scattering environments of real world interest is superior to linearly polarized light. To this end, we use a polarization tracking Monte Carlo program to investigate circularly polarized light's performance [3]. The Monte Carlo program tracks the polarization state of each photon in the simulation after every scattering event as they are propagated through a slab of scattering particles, Mie and/or Rayleigh sized. For each simulation run, one million photons of each polarization state were propagated into the slab of scattering medium orthogonal to the front face of the slab. If the photons exit the front face of the slab they are considered transmitted photons, if the photons exits the back face of the slab they are considered reflected or backscattered photons. For each simulation, a set of inputs are selected; these inputs are shown in Table 1.

Table 1: Monte Carlo inputs and definitions.

Input	*Symbol*	*(units)*
Particle Diameter	D	*(μm)*
Wavelength (vacuum)	λ_0	*(μm)*
Particle Refractive Index	$n_p - i\,k_p$	
External Medium Refractive Index	$n_m - i\,k_m$	
Relative Refractive Index	$m = \frac{n_p - i\,k_p}{n_m - i\,k_m}$	
Particle Density	ρ	*(particles/mm³)*
Slab Length	L	*(cm)*

From these inputs, the Monte Carlo utilizes Mie Scattering Theory for homogenous spherical particles to determine the single scattering properties of the scattering objects [24]. These inputs also give the overall optical thickness of the slab of scattering particles for each simulation configuration. The optical thickness, τ, is defined by the previously stated terms and the

extinction cross-section which is the sum of the scattering and absorption cross-sections, $\sigma_{ext} = \sigma_{sca} + \sigma_{abs}$, determined from Mie Scattering Theory.

$$\tau = \rho\, \sigma_{ext}\, L \qquad (4)$$

We utilized published numbers in order to verify our Monte Carlo simulation's output. Ishimaru, et. al. performed simulations looking at circular and linear polarizations transmitted DoP versus optical thickness for a specific scattering environment [18]. The environment of interest was 1.05 micron diameter latex spheres in water with an illumination wavelength of 0.53 microns. We performed similar simulations with our Monte Carlo program and we see confirmation with Ishimaru's results. Fig. 18 shows Ishimaru's results as a solid curve and a dotted curve with our corresponding simulation results shown with circles and squares.

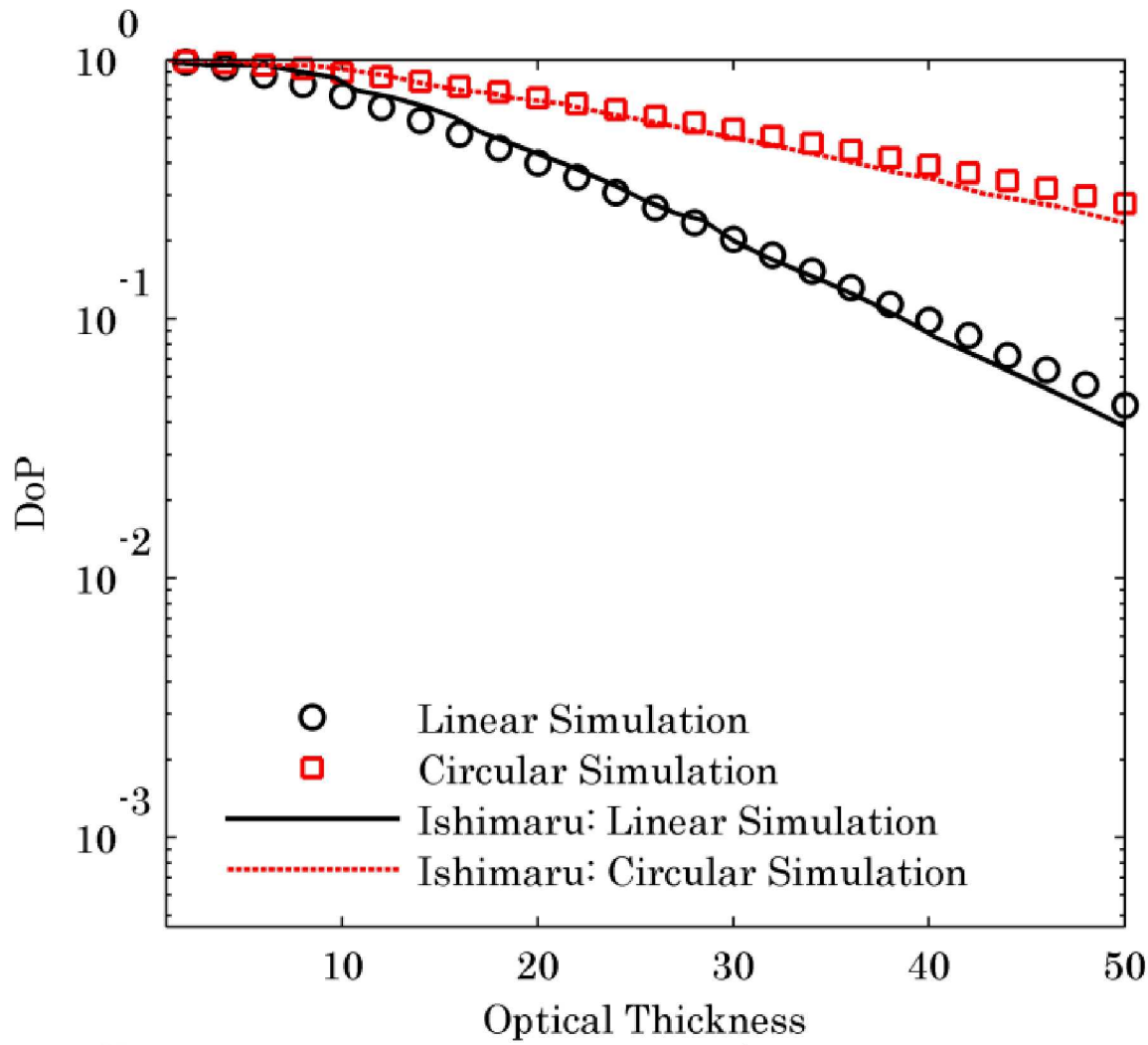

Fig. 18. Ishimaru's simulated transmission results (solid black curve and dashed red curve) [13] versus our confirming simulated transmission results (black circles and red squares) for 1.05 micron diameter latex spherical particles in water with an illumination wavelength of 0.53 microns

Before moving onto the environments of interest and our results we must define one more useful quantity. Throughout our analysis we are specifically interested in the performance difference between circular and linear incident polarization states on the slab of scattering medium. To clearly determine where circularly polarized light outperforms linearly polarized light a difference quantity is defined. The quantity, DoP_{diff}, is defined as the difference between the resulting transmitted DoP when circularly polarized light is incident versus when linearly polarized light is incident. The definition is defined in Equation 5.

$$DoP_{diff} = DoP_{circular} - DoP_{linear} \tag{5}$$

When circularly polarized light transmits with a higher DoP than linearly polarized light this quantity is positive. This quantity is negative when linearly polarized light transmits with a larger DoP. We note that the circularly polarized light persistence is generally a larger effect and over broader wavelength ranges than that of linearly polarized input. For this reason, it is of particular interest when the DoP_{diff} is positive and circularly polarized light maintains its DoP better than linearly polarized light.

3. Environments

Four realistic scattering environments were simulated: two types of fog (radiation and advection) and two types of Sahara dust (small and large). Three particle diameters were chosen from the particle size range for each environment. The particle sizes were chosen to coincide with small, large, and mean diameter sizes from the environments particle diameter distribution. All simulations were run with mono-disperse particle diameters, so this is not varying within a single run, in order to clearly isolate dependencies in performance across a wide wavelength range due to a single particle size. Simulating a size distribution will likely broaden responses as a function of wavelength, and is reserved for future work. All simulations were performed at an optical thickness, τ , of 5.

3.1 Radiation Fog

Radiation fog is the first environment simulated. Radiation fog is typically found near the ground, sometimes called ground fog, and arises when the earth cools thermally after the sun sets. The typical model for radiation fog consist of water particles with diameters smaller than 10 microns [27]–[29]. In order to simulate the range of particle sizes, three particle diameters were chosen: 1, 4, and 10 micron diameters.

3.2 Advection Fog

Advection fog was the second fog simulated. Advection fog is typically found near coastlines and marine environments. When wind moves water-dense air over colder surfaces, such as warm air traveling over cool waters, the air is cooled and advection fog is produced. Typical models of advection fog consist of larger particle sizes compared to radiation fog [29]. For our purposes we model advection fog as three particles diameters, 10, 20, and 40 microns. For both radiation and advection fog the refractive index values for water were taken from data measured and collected by Segelstein [30].

The following table describes the particle sizes that make up radiation, advection fog, and smoke in terms of the size parameter ($x = \frac{2\pi rn}{\lambda}$, where r is the particle radius, n is the refractive index of the external medium, and λ is the wavelength of the light).

		Wavelength (microns)									
		SWIR		MWIR			LWIR				
		1	2	3	4	5	8	9	10	11	12
Particle Diameter (microns)	1	3.14	1.57	1.05	0.79	0.63	0.39	0.35	0.31	0.29	0.26
	2	6.28	3.14	2.09	1.57	1.26	0.79	0.70	0.63	0.57	0.52
	3	9.42	4.71	3.14	2.36	1.88	1.18	1.05	0.94	0.86	0.79
	4	12.57	6.28	4.19	3.14	2.51	1.57	1.40	1.26	1.14	1.05
	5	15.71	7.85	5.24	3.93	3.14	1.96	1.75	1.57	1.43	1.31
	6	18.85	9.42	6.28	4.71	3.77	2.36	2.09	1.88	1.71	1.57
	7	21.99	11.00	7.33	5.50	4.40	2.75	2.44	2.20	2.00	1.83
	8	25.13	12.57	8.38	6.28	5.03	3.14	2.79	2.51	2.28	2.09
	9	28.27	14.14	9.42	7.07	5.65	3.53	3.14	2.83	2.57	2.36
	10	31.42	15.71	10.47	7.85	6.28	3.93	3.49	3.14	2.86	2.62
	11	34.56	17.28	11.52	8.64	6.91	4.32	3.84	3.46	3.14	2.88
	12	37.70	18.85	12.57	9.42	7.54	4.71	4.19	3.77	3.43	3.14
	13	40.84	20.42	13.61	10.21	8.17	5.11	4.54	4.08	3.71	3.40
	14	43.98	21.99	14.66	11.00	8.80	5.50	4.89	4.40	4.00	3.67
	15	47.12	23.56	15.71	11.78	9.42	5.89	5.24	4.71	4.28	3.93
	16	50.27	25.13	16.76	12.57	10.05	6.28	5.59	5.03	4.57	4.19
	17	53.41	26.70	17.80	13.35	10.68	6.68	5.93	5.34	4.86	4.45
	18	56.55	28.27	18.85	14.14	11.31	7.07	6.28	5.65	5.14	4.71
	19	59.69	29.85	19.90	14.92	11.94	7.46	6.63	5.97	5.43	4.97
	20	62.83	31.42	20.94	15.71	12.57	7.85	6.98	6.28	5.71	5.24
	21	65.97	32.99	21.99	16.49	13.19	8.25	7.33	6.60	6.00	5.50
	22	69.12	34.56	23.04	17.28	13.82	8.64	7.68	6.91	6.28	5.76
	23	72.26	36.13	24.09	18.06	14.45	9.03	8.03	7.23	6.57	6.02
	24	75.40	37.70	25.13	18.85	15.08	9.42	8.38	7.54	6.85	6.28
	25	78.54	39.27	26.18	19.63	15.71	9.82	8.73	7.85	7.14	6.54
	26	81.68	40.84	27.23	20.42	16.34	10.21	9.08	8.17	7.43	6.81
	27	84.82	42.41	28.27	21.21	16.96	10.60	9.42	8.48	7.71	7.07
	28	87.96	43.98	29.32	21.99	17.59	11.00	9.77	8.80	8.00	7.33
	29	91.11	45.55	30.37	22.78	18.22	11.39	10.12	9.11	8.28	7.59
	30	94.25	47.12	31.42	23.56	18.85	11.78	10.47	9.42	8.57	7.85

Radiation Fog Advection Fog Combination Fog Smoke

3.3 Small Particle Sahara Dust

The final two environments simulated were Sahara dust. The two different models illustrate small and large particles. The small particle Sahara dust sizes characterize dust that is typically suspended in various altitudes in the atmosphere. These small particle sizes are easily sent airborne and remain in the atmosphere for large distances. The diameters used for the small particle size model were 0.1, 1.5, and 6 microns [31], [32].

3.4 Large Particle Sahara Dust

The large particle Sahara dust sizes characterize dust found nearer to earth's surface [31], [32]. For the large particle size model, particle diameters of 10, 20, and 30 microns were used.

Both the small and large particle models used Sahara dust and sand refractive index information taken from Volz et. al [33]. The simulation results for Sahara dust all involve simulations of homogeneous spherical particles. The authors are aware of the fact that typical dust particles can be highly non-spherical which can be relevant for the polarization state of scattered photons.

4. Results

For each environment, one million photons of both circular and linear polarizations were launched, with normal incidence, into a slab of the specific particles. The resulting transmitted DoP was calculated and the DoP_{diff} was determined. The following figures show the DoP_{diff} versus wavelength for each environment. In order to better delineate where circularly polarized light outperforms linearly polarized light a line is plotted for a $DoP_{diff} = 0$ in the subsequent figures.

The results presented in this paper only consider the effects of absorption and scattering due to Mie scattering. The scattering particles are randomly placed in a slab of air (complex refractive index = 1.0 + i 0.0). The absorption of environmental gases, thermal emission of gases and particulates, as well as solar irradiance is not considered in these simulations although they can contribute significantly. Absorption by atmospheric gases such as CO_2, O_3, CH_4, and N_2O is a critical issue for signal persistence at infrared wavelengths. When these gases are present the absorption through the atmosphere at certain infrared wavelengths can rise to 100% even for short path lengths. Researchers that want to consider these absorption effects can simply reduce the transmitted values in each of the DoP calculations by the appropriate path length as a function of wavelength. This should not change our presented DoP_{diff} graphs except when each DoP calculation is reduced to zero.

The following results are shown for wavelengths of 1.9 to 12 microns for fog and 2.5 to 12 microns for dust. Although results are shown for all wavelengths in those ranges there are wavelengths that are not realistically usable due to atmospheric absorption from these gases [34].

4.1 Radiation Fog

The following two figures show results for radiation fog from the SWIR to the LWIR wavelengths. Fig. 19 shows circularly polarized light outperforms linearly polarized light for all three particle sizes for SWIR wavelengths. Circular polarization persists superiorly for the 1 micron particle through a wavelength of 1.9 microns. From a wavelength range of 1.9 – 2.5 microns, linear polarization persists superiorly for the 1 micron particle. The results for the 4 micron particle show some oscillation in the smaller wavelengths, but throughout the entire SWIR region circular polarization outperforms linear polarization. The 10 micron particle results show a preference for circular polarization throughout the SWIR region but this particle size shows a large amount of oscillatory behavior. At roughly a wavelength of 1.9 microns circular polarization clearly begins to persist superiorly for the 10 micron particle.

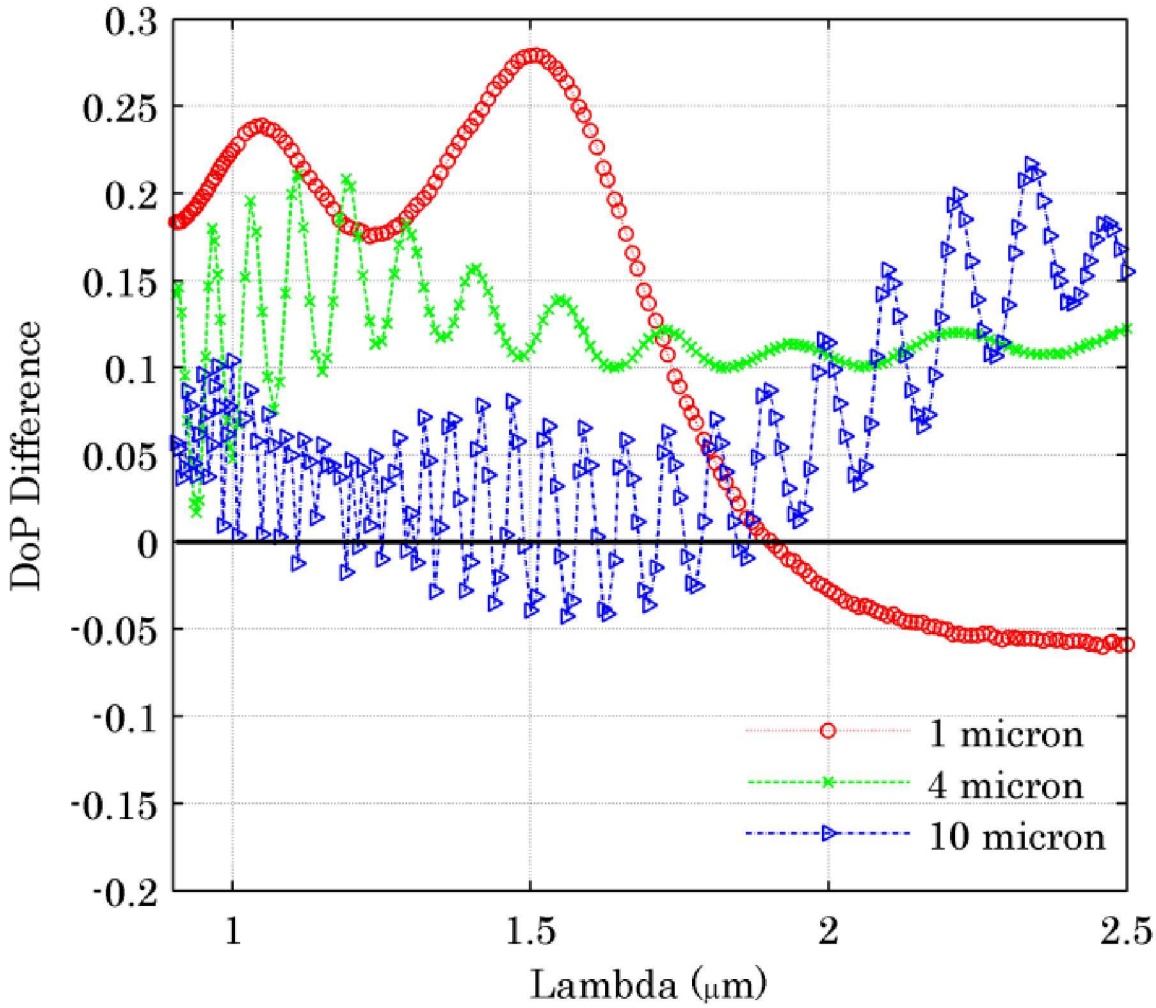

Fig. 19: Transmission DoP_{diff} results for radiation fog for SWIR wavelengths. 1 micron particle size results shown in red (circles), 4 micron particle size results shown in green (x's), and 10 micron particle size results shown in blue (triangles). A black line for DoP_{diff} = 0 delineates where linear polarization performs better (negative values) and where circular polarization performs better (positive values).

The radiation fog results for the MWIR through the LWIR are shown in Fig. 20. For both the MWIR and LWIR wavelengths, the small 1 micron particle shows preference for linearly polarized light. At a single wavelength of roughly 3 microns all three particle sizes show a preference for linearly polarized light. The two larger particle sizes show circular polarization persisting superiorly in the MWIR. The 4 micron particle has a larger DoP_{diff}, but circular polarization is clearly beneficial in this region. For the LWIR region, only the largest 10 micron particle size shows a persistence benefit for circularly polarized light. Linear polarization is preferred for both the 1 and 4 micron particles in the LWIR.

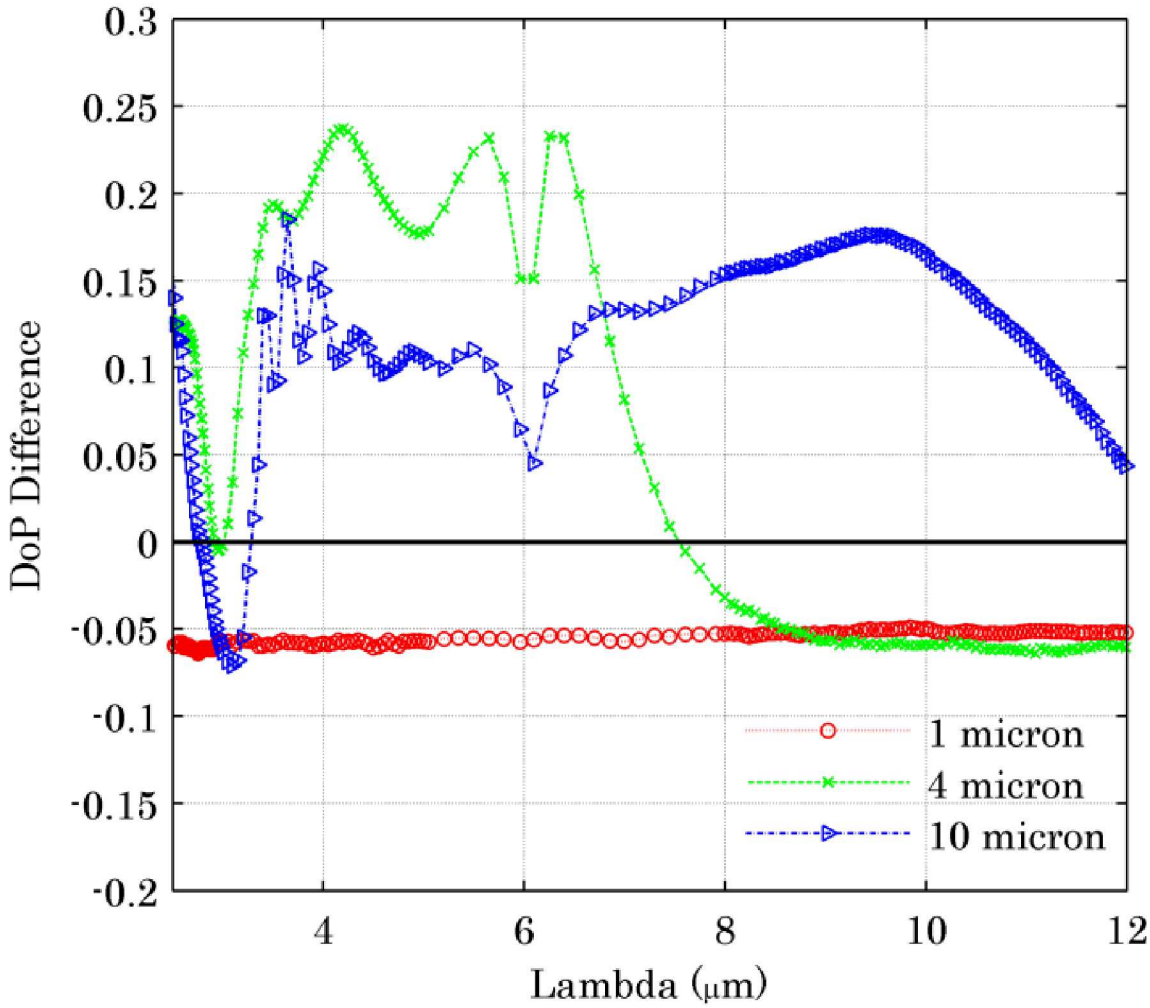

Fig. 20: Transmission DoP_{diff} results for radiation fog for MWIR through LWIR wavelengths. 1 micron particle size results shown in red (circles), 4 micron particle size results shown in green (x's), and 10 micron particle size results shown in blue (triangles). A black line for DoP_{diff} = 0 delineates where linear polarization performs better (negative values) and where circular polarization performs better (positive values).

The simulation results show clear wavelength ranges where circular polarization persists longer than linear polarization for radiation fog. The 1 micron particle shows circular polarization persists superiorly in the SWIR up to a wavelength of 1.9 microns. Circular polarization is superior for the 4 micron particle in the SWIR and MWIR regions. The 10 micron particle has a broad wavelength range where circular polarization persists better than linear. There are some oscillations in the lower end of the SWIR region but throughout the SWIR, MWIR, and the LWIR circular polarization is preferred and superior for the 10 micron particle.

4.2 Advection Fog

Results for the advection fog simulations are shown in Fig. 21 and Fig. 22. Fewer data points were generated for each particle diameter for the advection results due to increased

computation time for the larger particle sizes. For comparison, the 10 micron results for advection fog are the exact same as those for radiation fog, since the refractive index and size is the same. The additional points available in the radiation results are omitted for congruency with the other sets of data in order to maintain the same number of data points and to clarify the plots. The spectral resolution on the advection fog plots are thus lower than the radiation fog plots but the general patterns can still be observed.

The SWIR results are shown in Fig. 21. Similar to the radiation fog results, the 10 micron particle shows oscillations in the lower end of the SWIR region but is generally positive for circular polarization. The 20 and 40 micron particles show a preference for circular polarization throughout the SWIR region. Due to the lower sample size and spectral resolution it is difficult to determine with certainty whether the larger particles maintain their circular polarization persistence benefit uniformly or if the oscillations are merely sampled out.

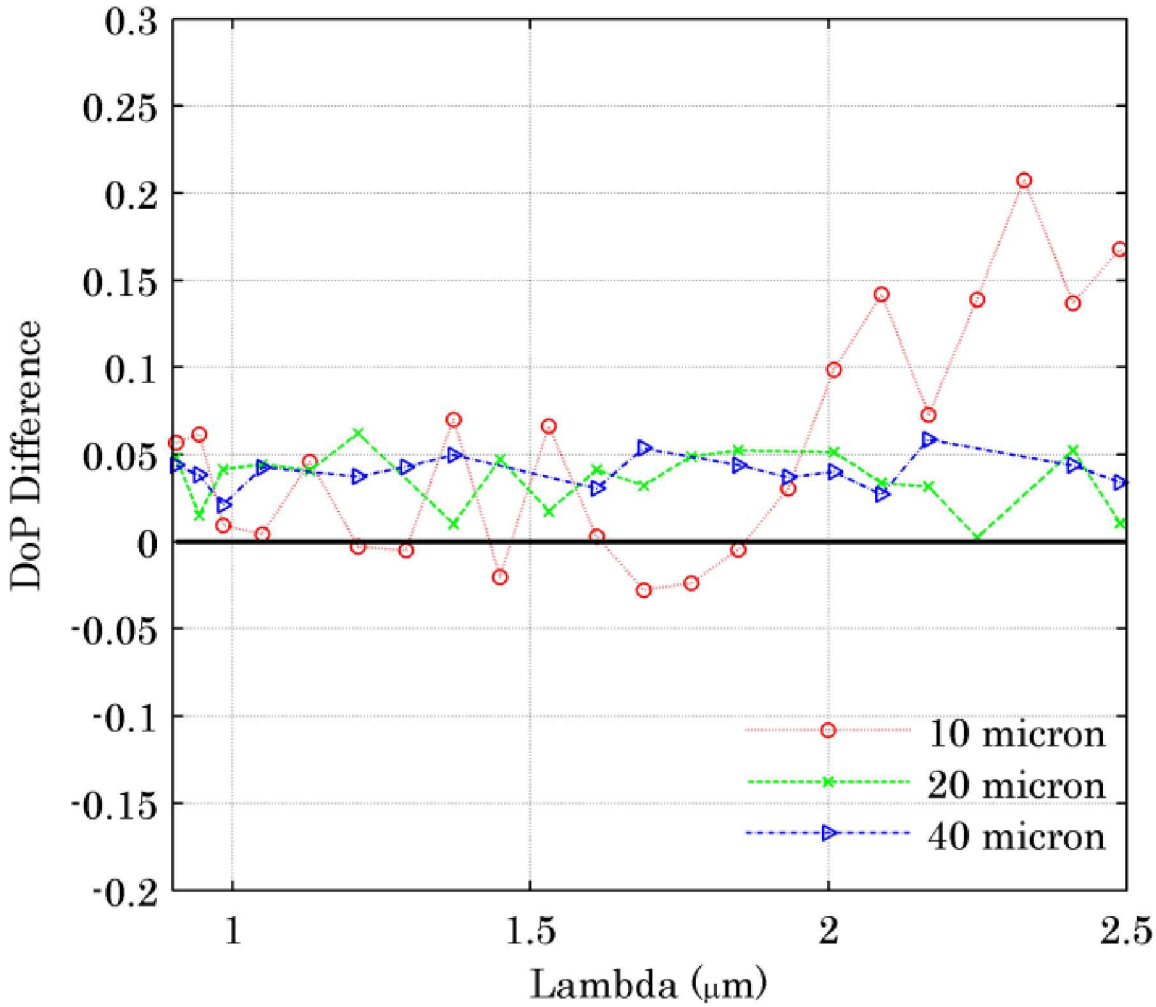

Fig. 21: Transmission DoP_{diff} results for advection fog for SWIR wavelengths. 10 micron particle size results shown in red (circles), 20 micron particle size results shown in green (x's), and 40 micron particle size results shown in blue (triangles). A black line for DoP_{diff} = 0 delineates where linear polarization performs better (negative values) and where circular polarization performs better (positive values).

The MWIR and LWIR advection results are shown in Fig. 22. Similar to the radiation fog results, all three particle sizes show a preference for linear polarization at a single wavelength of 3 microns. As in the radiation fog case, the 10 micron particle clearly shows superior persistence for circular polarization throughout the MWIR and LWIR regions. There is some oscillatory behavior in the 3-4 micron wavelength range but after 4 microns the 20 micron particle shows a preference for circular polarization through to the end of the LWIR. The 40 micron particle is more limited in wavelengths showing beneficial persistence for circular polarization. There are multiple wavelength ranges in the MWIR. Generally, circular is preferred from 3.5-5 microns, with a dip at 4.7 microns where circular and linear are equal in persistence. Circular polarization has increased persistence for the 40 micron particle through almost all of the LWIR, 7-11 microns.

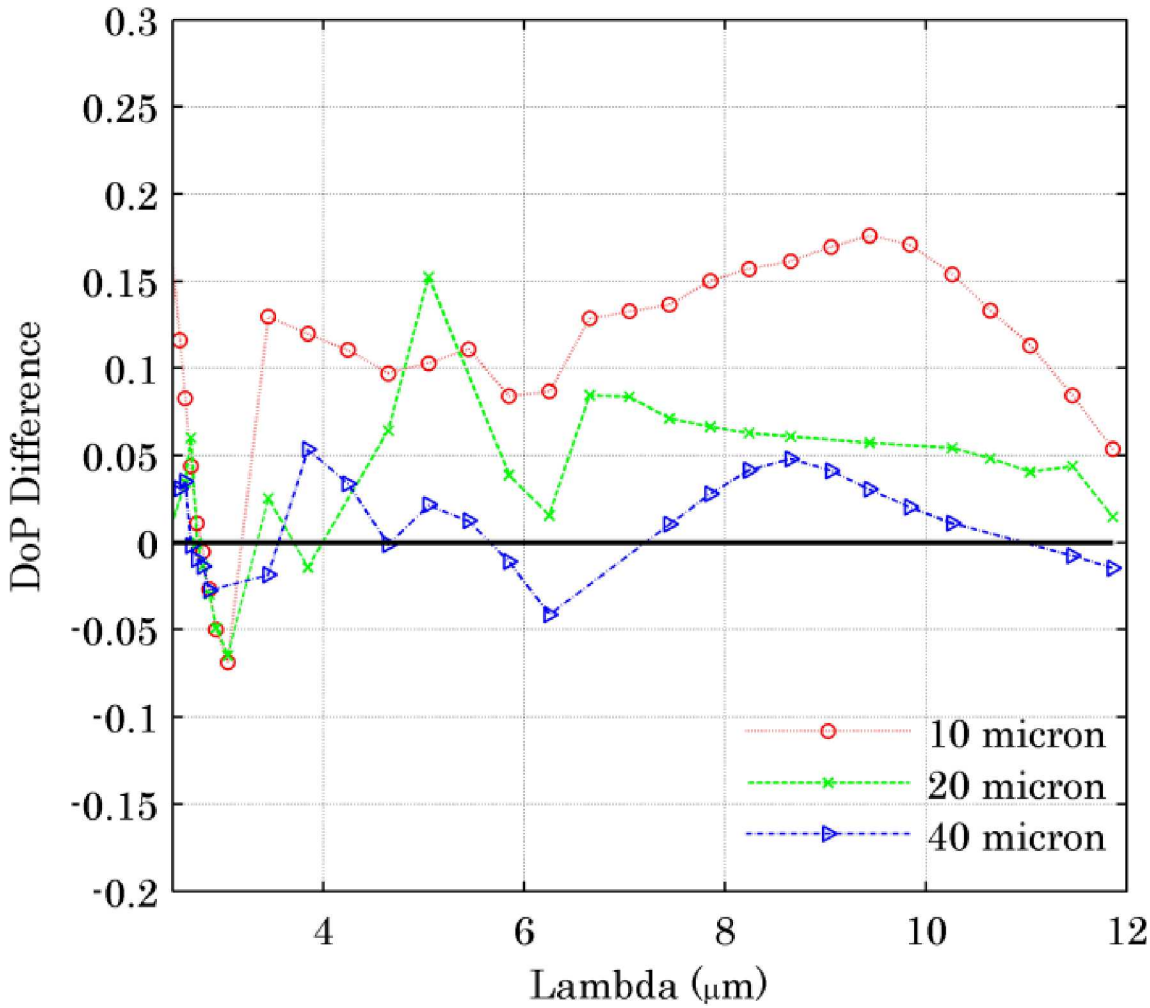

Fig. 22: Transmission DoP_{diff} results for advection fog for MWIR through LWIR wavelengths. 10 micron particle size results shown in red (circles), 20 micron particle size results shown in green (x's), and 40 micron particle size results shown in blue (triangles). A black line for DoP_{diff} = 0 delineates where linear polarization performs better (negative values) and where circular polarization performs better (positive values).

Advection fog shows multiple clear wavelength ranges where circular polarization persists longer than linear polarization. There are some oscillations in the SWIR region but generally all particle sizes show a preference for circular polarization. The MWIR region is mixed. Circular polarization is preferred for the 10 micron particle through the entire region, the 20 micron particle is positive after a wavelength of 4 microns, and the 40 micron particle oscillates but generally is positive for wavelengths greater than 3.5 microns in the MWIR. Throughout the LWIR regime all particle sizes show superior circular polarization persistence. All the particles show positive DoP_{diff} from 7-11 microns. The 40 micron particle is the only particle that shows any preference for linear polarization in the LWIR and it is only for wavelengths of 11-12 microns. In general, we can expect transmitted circular polarization to persist longer than linear polarization for the LWIR region from 7 to 11 microns with advection fog scattering particles with diameters spanning 10 and 40 microns.

4.3 Small Particle Sahara Dust

As there is no refractive index data available from Volz, et al. for SWIR wavelengths, the results for Sahara dust were generated for the MWIR and LWIR regions only, using the available refractive index data [33].

Fig. 23 shows the results for the small particle Sahara dust model. Linear polarization dominates for the very small particle sizes of 0.1 and 1.5 microns. The 1.5 micron particles show possible promise at lower wavelengths. Transmitted circular polarization persists much better for the 1.5 micron particle from 2.5-3.25 microns. This performance may be positive in the SWIR region as well but is left for future investigation. For the larger 6 micron diameter particles, circular polarization persists better than linear throughout the MWIR region as well as the low and high end of the LWIR region. Between a wavelength of 9 and 10.5 microns all three particle sizes show a persistence benefit for linear polarization.

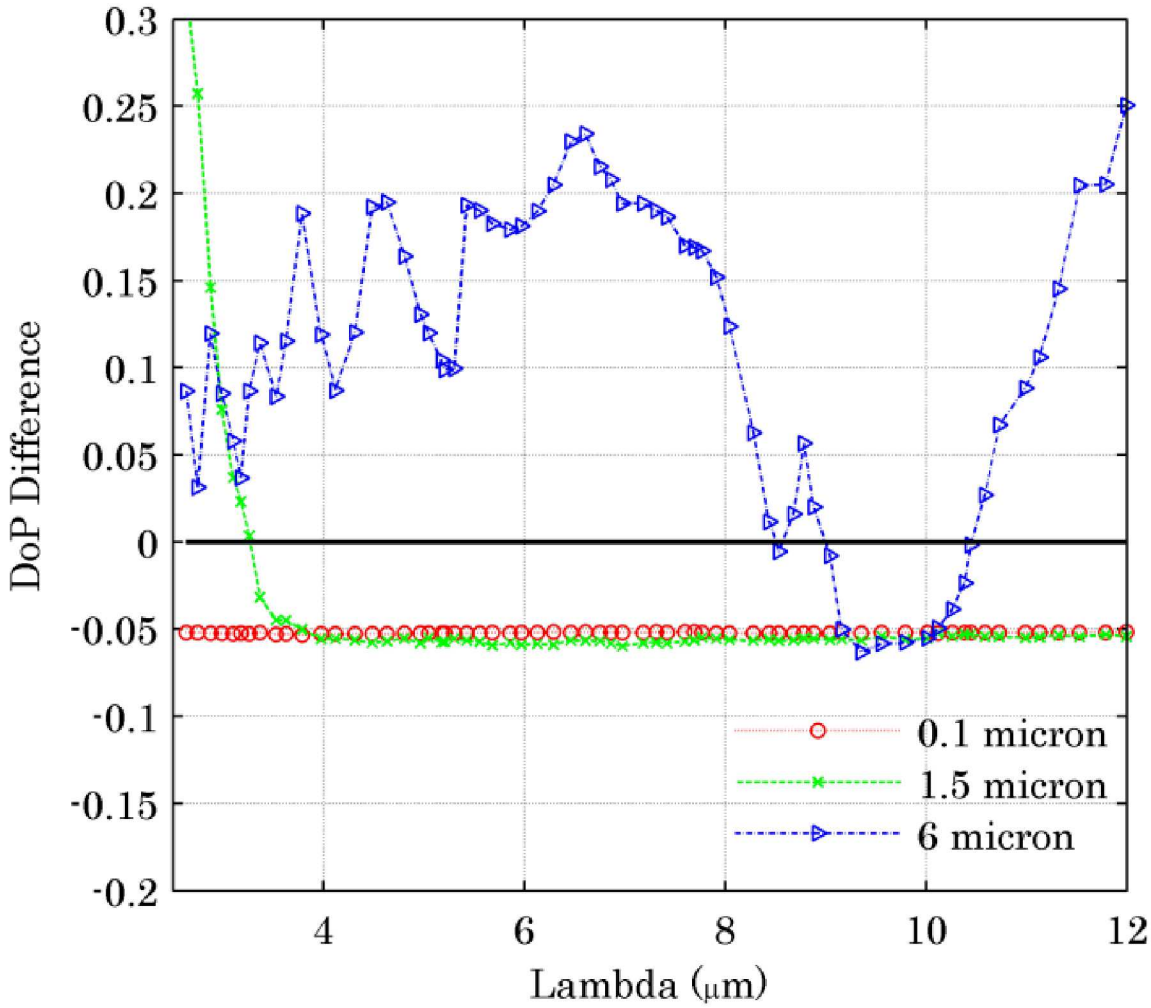

Fig. 23: Transmission DoP_{diff} for small particle diameters of Sahara Dust for MWIR through LWIR wavelengths. . 0.1 micron particle size results shown in red (circles), 1.5 micron particle size results shown in green (x's), and 6 micron particle size results shown in blue (triangles). A black line for DoP = 0 delineates where linear polarization performs better (negative values) and where circular polarization performs better (positive values).

In summary for small particle Sahara dust, linear polarization persists for the smallest 0.1 micron particle through all wavelengths simulated. Circular polarization persistence dominates for the 1.5 micron particle from 2.5 – 3.25 microns wavelength range, but continues with a smaller linear persistence from 3.25 – 12 microns wavelength range, similar to the 0.1 microns particle size. Note that all particle sizes, for a wavelength range of 9 - 10.5 microns, maintain a linear polarization persistence. Finally, the 6 micron Sahara dust particles show a large response for two broad wavelength ranges (2.5 – 9 microns and 10.5 – 12 microns) where circular polarization persists longer than linear polarization.

4.4 Large Particle Sahara Dust

The results for the large particle Sahara dust model for the MWIR through the LWIR are shown in Fig. 24. The 10 micron particle oscillates in the MWIR region but shows some preference for transmitted circular polarization from 3.5 to 5 microns. Circular polarization again persists superiorly in the low and high ends of the LWIR region. Specifically, circular polarization is preferred up to wavelengths of 8.75 microns and from 11.25 to 12 microns. The 20 micron particle has a small wavelength range where circular polarization superiorly persists. The wavelength range is from a wavelength of 3.25 to 5.5 microns. The 20 micron particle also has a positive DoP_{diff} value from 7.5 to 8.5 microns but generally linear polarization persists better in the LWIR for this particle size. The results for the 30 micron particle are nearly identical to the 20 micron particle results. The wavelength ranges are slightly smaller and the overall performance is smaller than with the 20 micron particle.

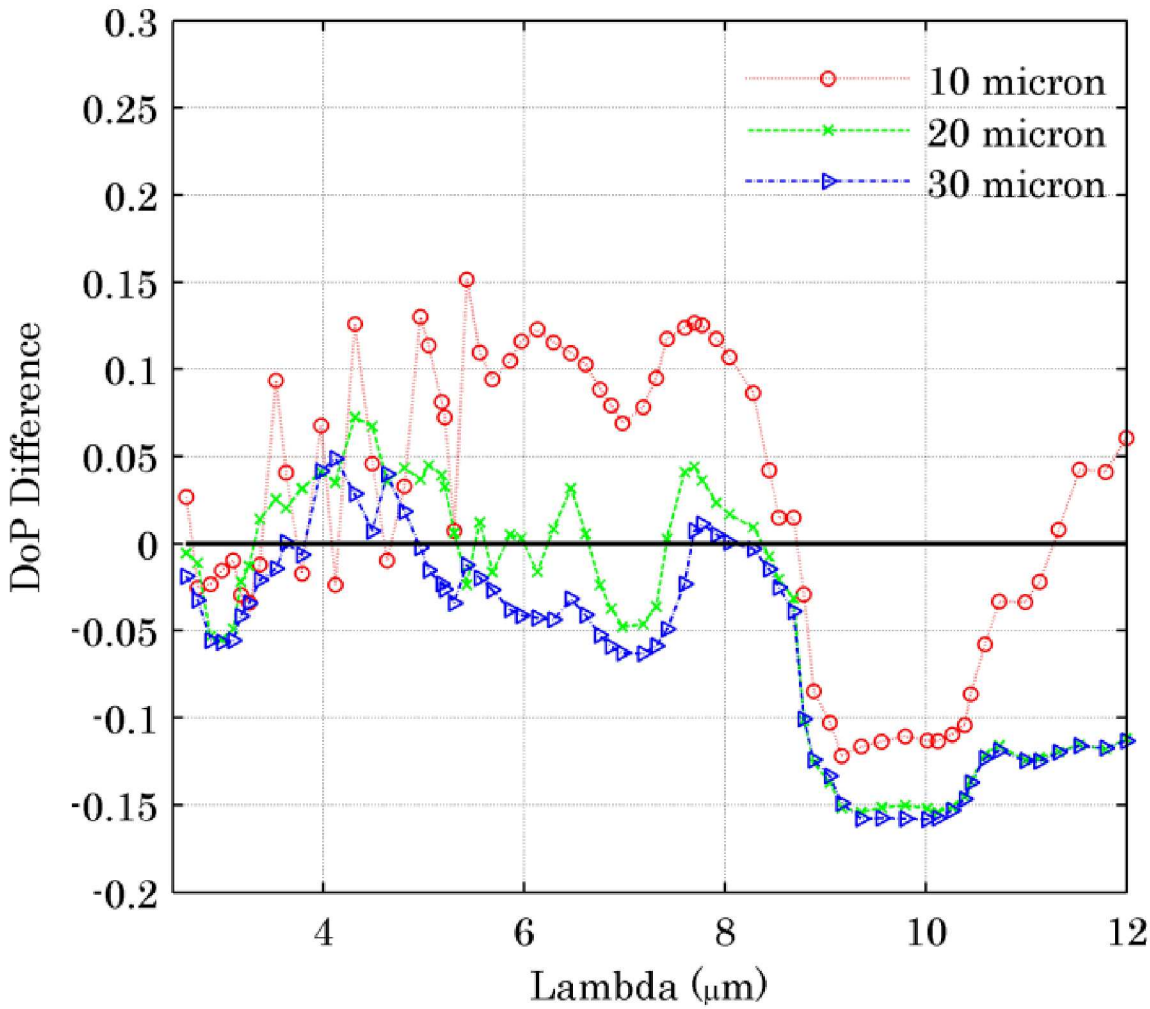

Fig. 24: Transmission DoP_{diff} for large particle diameters of Sahara Dust for MWIR through LWIR wavelengths. 10 micron particle size results shown in red (circles), 20 micron particle size results shown in green (x's), and 30 micron particle size results shown in blue (triangles). A black line for DoP_{diff} = 0 delineates where linear polarization performs better (negative values) and where circular polarization performs better (positive values).

In summary, for large particle Sahara dust environments, linear polarization shows the dominant persistence benefits for all three particle sizes for a wavelength range of 8.75 - 12 microns. Circular polarization persists superiorly for the 10 micron particle size across a broad wavelength range of 3.5 – 8.75 microns. Otherwise, responses are small and mixed for the 20 micron and 30 micron particle sizes below a wavelength of 8.75 microns.

5. Conclusions

Through the use of polarization-tracking Monte Carlo simulations we have shown that there are clear, broad wavelength ranges where transmitted circular polarization maintains its illuminating polarization state superiorly compared to linear polarization for highly scattering environments representative of fog, including radiation and advection fog. We also examined small and large particle Sahara dust and found that circular polarization maintains its illuminating polarization state, compared to linear polarization, with larger response and over broader wavelength ranges than with linear polarization, but only for limited particle sizes. All four realistic environments show wavelength ranges where circular polarization can be utilized to increase detection range. Radiation fog has wavelength ranges available in the entire IR spectrum. All three particle sizes simulated (1, 4, and 10 microns) show a preference for circular polarization in the SWIR, the 4 and 10 micron particles show a preference in the MWIR, and the 10 micron particle exhibits superior persistence for circular polarization in the LWIR. All three particle sizes in the advection fog model (10, 20, and 40 microns) show a preference for circular polarization at SWIR and LWIR wavelengths.

The persistence of circular polarization is positive but not as pronounced for the two dust model particle size regimes (small and large Sahara dust). Here, the 6 micron particle size results from the small particle Sahara dust shows persistence benefits for the broad wavelength ranges of 2.5 - 9 microns and 10.5 - 12 microns. Also in the large Sahara dust simulation, circular polarization persists superiorly for the 10 micron particle size across a broad wavelength range of 3.5 – 8.75 microns.

This work breaks from previously published works and offers new insight into potential realistic environments with broad wavelength ranges of interest where circular polarization can be utilized to increase detection range. Most previous research focused on singular wavelengths in the visible region with underwater scattering environments typically utilizing readily available polystyrene microspheres, milk, or tissue phantoms as scattering objects. We have produced simulation results supporting broad wavelength responses for particle sizes and refractive indices representative of natural scattering environments, especially noting where circular polarization persists with a larger response and through broader wavelength ranges than linear polarization. This work should inspire continued interest in circular polarization's benefits in various applications involved in scattering environments, specifically increasing detection range. Future work includes simulating with polydisperse distributions of scattering particles, collecting scattered photons as a function of field of view, and measuring in real-world scattering environments all utilizing active illuminating circular polarization.

5. SIMULATION RESULTS: EVOLUTION IN SCATTERING ENVIRONMENTS

The following section consists of work published in an Optics Express paper titled "Evolution of circular and linear polarization in scattering environments" [35].

Introduction:

In this work, the evolution of circularly and linearly polarized light as it scatters throughout a variety of scattering environments is fully investigated. In particular, we show circularly polarized light exhibits superior persistence for forward-scattering particle environments. Circularly polarized light's increased persistence compared to linearly polarized light, often called polarization memory, is of importance for many sensing techniques in scattering environments but until now this scattering evolution has not been detailed. This work presents simulation results showing the evolution of polarized light in scattering environments of forward and isotropically (Rayleigh regime) scattering particles for both forward and backscattered photons.

The use of polarized light in scattering environments, specifically the difference between circularly and linearly polarized light's interactions in scattering environments, is of interest. Previous research has shown benefits for the use of both linear and circular polarization for sensing in specific scattering environments, often showing increased performance benefits for circularly polarized techniques [7], [15], [16], [21], [36], [37]. Previous work has focused on isolated visible wavelengths and underwater scattering environments. We recently published unique simulation results showing superior persistence for circular polarization versus linear polarization in scattering environments of fog and dust over broad wavelength ranges at infrared wavelengths [5], [23], [38]. Sensing in scattering environments utilizing polarization relies on the polarization persistence, or polarization memory, of the light. The mechanism of circular polarization's increased persistence has been theoretically hypothesized; it is proposed that circular polarization depolarizes due to the randomization of the photon's direction and the randomization of the helicity [22], [39]. Xu and Alfano find the benefits for circular polarization are greatest for large particles with refractive indices close to the air environment (refractive index ~ 1) and for small, high-index contrast particles (refractive indices between 1.5 and 2) [22]. Xu and Alfano's work, as well as Bicout et al.'s preceding work, focuses on the analytical uncoiling length and circular depolarization length as their metrics [17]. These works do not present how polarized light evolves in scattering environments toward this increased persistence for circular polarization.

A number of groups have investigated the temporal response of polarized light pulses in scattering environments. Ishimaru et al. performed simulations for polarized pulses of light incident on a slab of latex scattering particles in water for an angularly limited exit beam at a wavelength of 0.53 μm [18]. The solution's size distribution was nearly monodisperse with a mean particle diameter of 2.019 microns. Their results show circular polarized light has a larger Degree of Polarization (DoP) over time for photons exiting the slab into a narrow forward half angle of 3 degrees. As in this work, Ishimaru et al. show that the DoP for circularly polarized pulses decreases more gradually than it does for linearly polarized pulses for the forward direction. Ishimaru's work shows circular polarized pulses maintain their DoP longer in time than linearly polarized pulses transmitted through the slab but offers no insight in how or when the polarized states are modified throughout the environment. Kim and Moscoso simulated the temporal variations of backscattered flux for incident circularly polarized pulses [40]. They

investigated scattering environments of latex spheres with monodisperse particle distributions of 0.076 μm, 0.189 μm, and 0.303 μm with an illumination wavelength of 633 nm. For the smallest particle size, the dominant backscattered flux is from the opposite handedness circular polarization. For the larger two particle sizes, the initial backscattered state is the opposite handedness but almost immediately the backscattered flux is dominated by the initial incident handedness. Finally, Cai et al. show temporal results for simulations of particle diameters of 0.1 μm, 0.213 μm, 0.855 μm and 8 μm and experiments with particle diameters of 0.213 μm and 8 μm, all at an illuminating wavelength of 610 nm [41]. They generally conclude that circularly polarized pulsed light, of the same handedness dominates backscattered light when the scattering particles are larger than the incident wavelength. When the scattering particles are smaller than the wavelength (Rayleigh regime) the opposite is shown to be the case. These works are all limited to the temporal variation of backscattered light.

Finally, researchers are investigating depolarization and enpolarization, from various scattering processes including scattering from rough surfaces, disordered media, speckle patterns, inhomogeneities, and other complex media [42]–[48].

To date, no research has examined the evolution of incident polarized light, as a function of scattering event for both forward and backscattered photons. In this work we present simulation results for scattering environments of polystyrene microspheres in water. Specifically, we look at monodisperse particle distributions with particle diameters of 0.1 μm, 2.0 μm, and 3.0 μm at an incident wavelength of 543.5 nm. These parameters correspond to isotropic scattering (0.1 μm Rayleigh regime) as well as forward-scattering particles (2.0 μm and 3.0 μm). The parameters are representative of radiation and advection fog at infrared wavelengths. This work was initiated with our recent conference paper which was limited to a single forward-scattering size parameter [49]. Monte Carlo simulations, presented here, for these scattering environments illustrate the evolution of circularly and linearly polarized incident light using the Poincaré sphere after successive scattering events throughout the scattering environment. Circular polarization persists through a larger number of scattering events for both forward and backscattered photons for all of the large particle scattering environments. These results quantify circular polarization's smooth and slow degradation as a function of scattering event, compared to linear polarization's abrupt degradation through a scattering environment.

This article is organized as follows: Section 2 covers the background of polarization, polarization-tracking Monte Carlo simulations, and the representation of polarization on the Poincare sphere, Section 3 presents the Monte Carlo simulation results for linearly polarized light scattering in forward and isotropic scattering environments, Section 4 presents Monte Carlo simulation results for circularly polarized light in the isotropic and forward-scattering environments, comparing these results to those presented for linearly polarized light, and Section 5 concludes, showing circular polarization persists superiorly for forward and backscattered photons in all of the forward-scattering environments.

Background:

The fraction of measured light that is purely polarized is the Degree of Polarization (DoP). The DoP is defined using the Stokes parameters (S_0, S_1, S_2, S_3),[50]

$$DoP = \frac{\sqrt{{S_1}^2 + {S_2}^2 + {S_3}^2}}{S_0}. \tag{2}$$

The DoP ranges from 0 for completely unpolarized light to 1 for purely polarized light. A Stokes vector with a DoP between 0 and 1 is partially polarized. The Poincaré sphere can represent any possible polarization state or Stokes vector [50], [51]. For example, vertical linear polarization is indicated on the Poincare sphere in Figure 25 with an orange sphere.

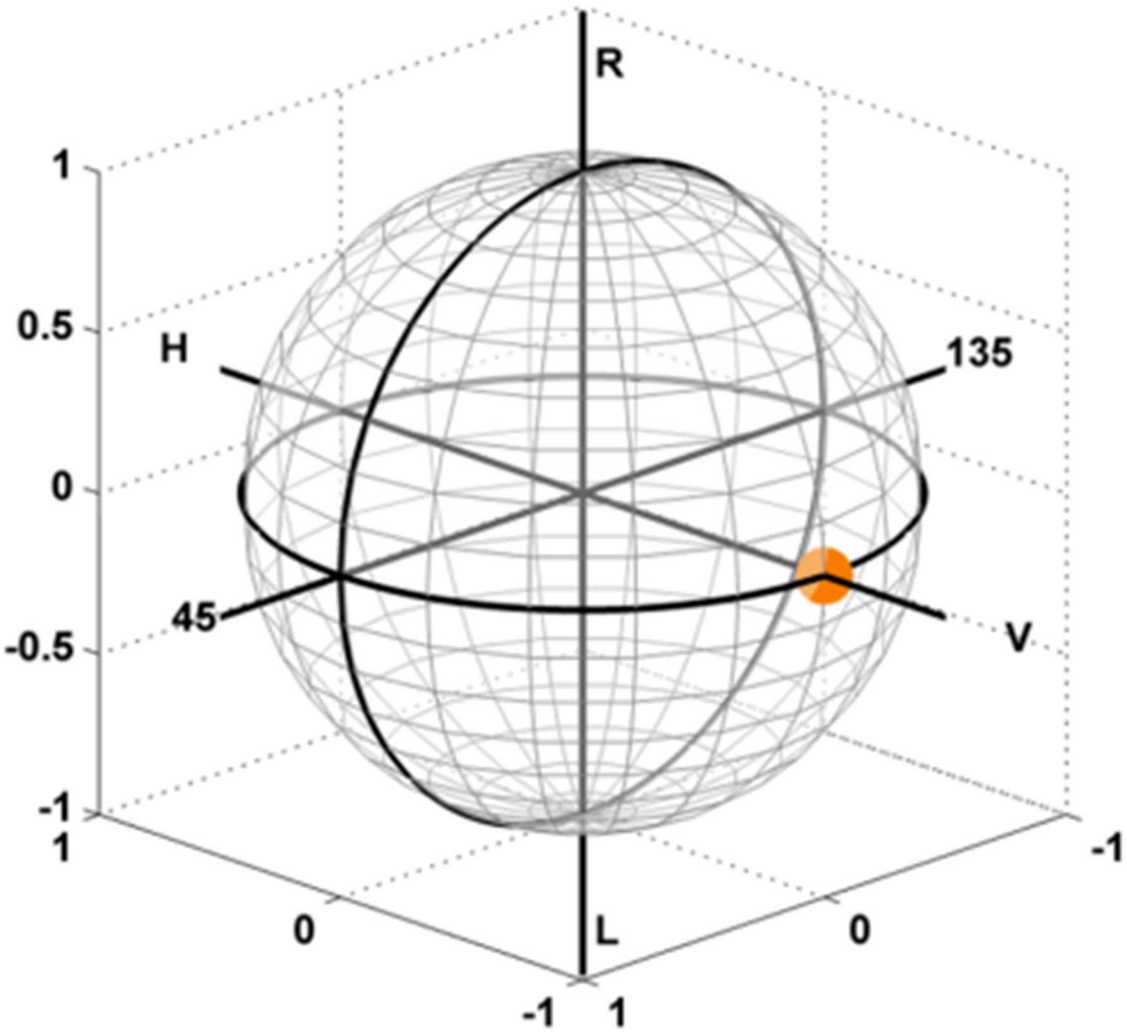

Figure 25: Poincaré sphere representation of vertical linearly polarized incident light. (Orange sphere represents location.)

The goal of this work is to investigate the evolution of circularly and linearly polarized light's polarization state in scattering environments. To this end, we use a polarization-tracking Monte Carlo program for all our simulation results [3]. Both circularly and linearly polarized photons (one million of each polarization state for each simulation) are propagated perpendicular to the face of a slab of scattering media. Rigorous Mie scattering theory is utilized for each

simulated scattering event. Scattering particles are modeled as homogenous refractive index (1.597 for polystyrene) spheres. For all the individual scattering events, the polarization and angular scattering properties of a single scattering event are calculated for all incident polarization states and angles [24]. Two parameters of the scattering particles are used within the calculations, the size parameter and the relative refractive index. The relative refractive index is the ratio of the particle's refractive index to the refractive index of the external medium. The size parameter of the scattering particle is a ratio of the particle's size and index, to the incident wavelength. In Equation 3, x is the size parameter, a is the radius of the scattering particle, n is the real refractive index of the external medium (not the particle medium), and λ_0 is the vacuum wavelength of the light.

$$x = \frac{2\,\pi\,\mathrm{a}\,\mathrm{n}}{\lambda_0}, \tag{3}$$

The particle diameters 0.1 μm, 2.0 μm, and 3.0 μm and the incident wavelength of 543.5 nm used in these simulations correspond to unitless size parameters 0.77, 15.4, and 23.1. Results for a particle size of 1.0 μm, corresponding to a size parameter of 7.7, can be found in our recent conference paper [49]. Scattering environments with size parameters in these ranges encompass a wide range of natural environments, such as radiation and advection (marine) fog. These particle sizes and the resulting scattering environments cover both isotropically (Rayleigh regime) and forward-scattering situations.

The Monte Carlo simulation tracks the location and polarization state of each photon. Tracking is performed for the location of each photon before and after each scattering event as well as for the polarization state of each photon before and after each scattering event. An initial Stokes vector sets the photon's initial polarization state. The polarization state of each photon is modified and its Stokes vector is updated after each scattering event. It is important to note, the Stokes parameters of individual photons in the Monte Carlo simulation are single instantaneous "independent light streams" and are thus purely polarized (DoP = 1) [52], [53]. The ensemble of the individual photons Stokes parameters, called the cumulative Stokes state throughout this paper, represents the measureable polarization state and can be purely polarized, partially polarized, or completely unpolarized (0 <= DoP <= 1).

Forward-scattered photons are those that are scattered to a location further into the scattering slab than the scattering event location. Conversely, backscattered photons are those that are scattered to locations closer to the input face of the slab. The density of particles for each simulation was such that a sufficient number of scattering events would occur for each incident photon, resulting in an optical thickness of 10 [5], [24].

Linearly Polarized Initial Illumination

The vertical linearly polarized state of the incident photons is plotted on the Poincaré sphere in Figure 25. The initial Stokes state of the incident photons is located at the center of the large orange sphere. All one million photons for this polarization state started in this position on the Poincaré sphere.

In order to reduce the clutter of the plots in the following figures, we choose the first one hundred thousand photons from the incident one million for each plot. The Stokes parameters for each of the one hundred thousand photons are plotted on the Poincaré sphere after a specified number of scattering events. Forward-scattered photons are colored red and backscattered photons are colored blue in the following figures. All the photons' Stokes parameters are

ultimately transformed into the global reference frame set by the initial slab geometry and the initial polarization states. The following figures illustrate the resulting scattered Stokes parameters after 1, 2 and 10 scattering events for each environment. Each individual photon's Stokes polarization state is plotted on the surface of the Poincaré sphere since they are purely polarized. The cumulative Stokes state, for all the forward or backscattered photons of the incident one million photons, is shown as a large sphere in either orange or purple, respectively. The cumulative Stokes state is located inside or very close to the surface of the Poincaré sphere since it is generally partially polarized.

The following results are split into two sets: 1) for the forward-scattering particle environments, and 2) for the isotropic (Rayleigh regime) scattering particle environment.

A) Forward-scattering Environments: Linear Polarization

The normalized angular scattering for each particle is shown on the polar plots in Figure 26. These plots illustrate the differences between the angular scattering properties of each particle size. The particle is placed at the center of the plot and the plots show how likely it is, for incident radiation from the 180 degree location, to scatter at each angle. The scattering from radiation perpendicularly polarized to the page is plotted in solid black; a dashed blue curve corresponds to parallel oriented incident radiation. For these forward-scattering particles, the blue and black curves are nearly indistinguishable and the blue curves are not visible on the plots. As is evident in the plots, the probability to scatter backwards is very small for these environments. Less than 1 percent of all the incident photons are backscattered after any single scattering event for the forward-scattering particle environments.

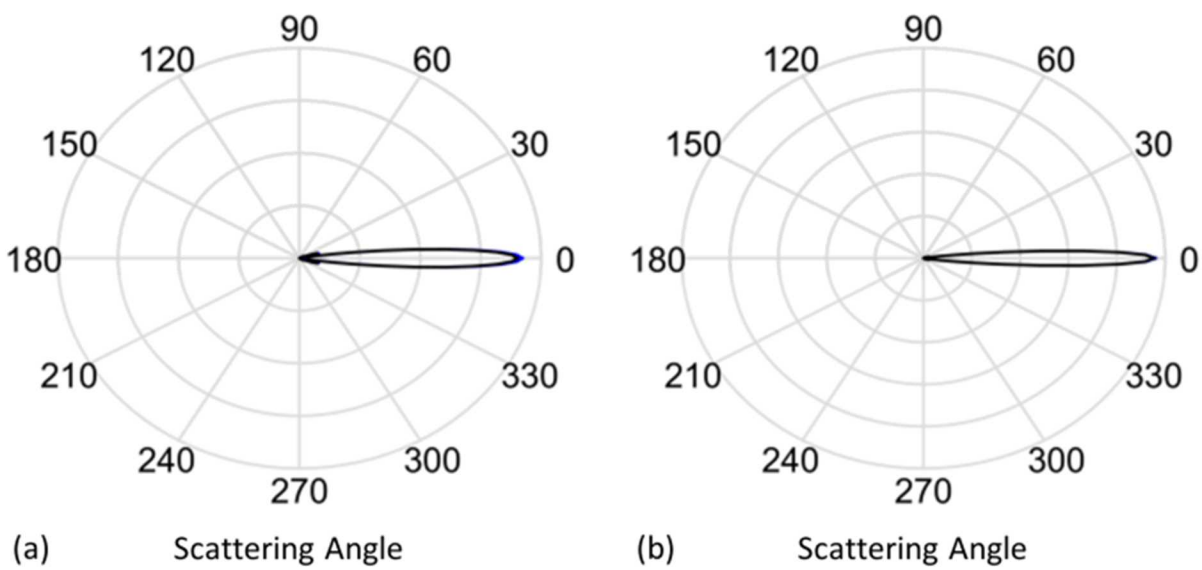

Figure 26: Scattering profiles for particle sizes of (a) 2.0 μm and (b) 3.0 μm. Perpendicular and parallel incident polarization states scattering are plotted as black and blue curves. For these forward-scattering particles, the blue and black curves are indistinguishable and the blue curves are not visible on the plots.

Figure 27 and Figure 28 show the results for incident linearly polarized scattered photons after one (a), two (b), and ten (c) scattering events for the forward-scattering particle sizes 2.0

µm (Figure 27) and 3.0 µm (Figure 28). After one scattering event (a), forward-scattered photons (red) for the particles remain close to their initial location on the Poincaré sphere. The forward-scattered Stokes parameters initially spread equally along the equator and in the direction of the poles for both particle sizes. The cumulative Stokes state for the forward-scattered photons (orange) is nearly purely polarized for the each of the particle sizes. The backscattered photons Stokes parameters (blue) are spread around the Poincaré sphere. As the particles size increases more of the backscattered photons gain ellipticity. This is especially evident when comparing the results presented here and those in our previous conference paper. [49] Although there are more elliptical states for increasing sizes, the cumulative backscattered photons' Stokes state (purple) is highly depolarized and has little to no ellipticity. The resulting cumulative backscattered depolarized state is close to the origin of the Poincaré sphere it still has a small preference for vertical linear polarization. Vertical linearly polarized light tends to remain nearly purely polarized if forward-scattered after one scattering event. After a single scattering event, backscattered photons are highly depolarized. Both the forward and backscattered photons' Stokes parameters are spread around the Poincaré sphere more after two scattering events than after one scattering event. After two scattering events (b), the cumulative forward-scattered Stokes state is still highly polarized. This state remains close to the initial polarization's location on the Poincare sphere. It is hard to see in the figures but the cumulative backscattered Stokes state is slightly more depolarized than after one scattering event. Forward-scattered photons' Stokes parameters for both particle sizes spread more around the equator than toward the poles. After ten scattering events (c) the individual photons' polarization states are highly spread around the Poincaré sphere. Backscattered Stokes parameters increasingly spread around the Poincare sphere as the particle size grows. The cumulative backscattered state is located near the origin, DoP ~ 0, nearly completely depolarized for both particle sizes. Although it is not visible in the figures, the cumulative forward-scattered state is inside the surface of the Poincaré sphere and has depolarized. The depolarization of the vertical linearly polarized forward-scattered photons tends to spread along the equator more than toward the poles. This preference to spread along the equator is present for all the forward-scattering particle sizes. For the forward-scattering environments, linear polarization depolarizes into other linear polarization states faster and more readily than into elliptical polarization states.

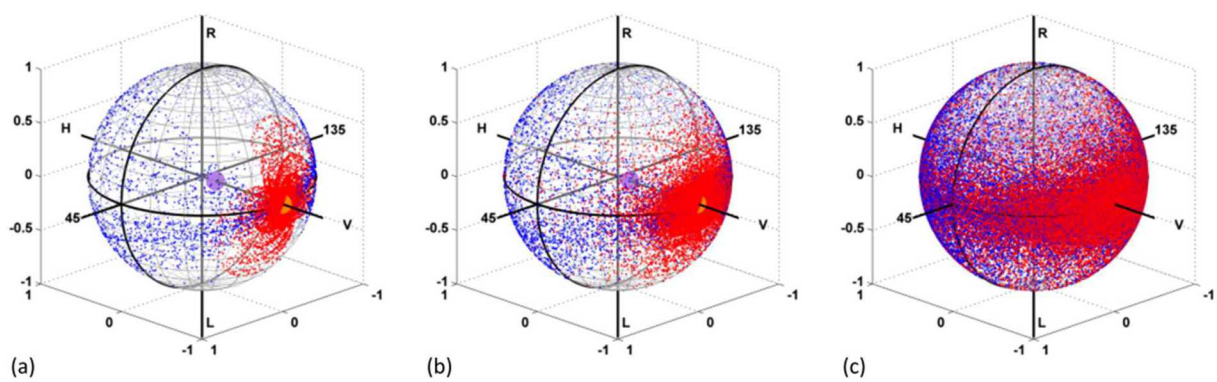

Figure 27: Scattered Stokes parameter values for incident linearly polarized light after (a) 1, (b) 2, and (c) 10 scattering events for a scattering environment consisting of particles with diameter 2.0 µm and an illuminating wavelength of 543.5 nm. This figure shows the first 100,000 photons' resulting Stokes parameters after each scattering event; forward-scattered photons are shown in red and backscattered photons are shown in blue. The

resulting cumulative Stokes state, for the forward or backscattered photons, is shown as large orange or purple spheres.

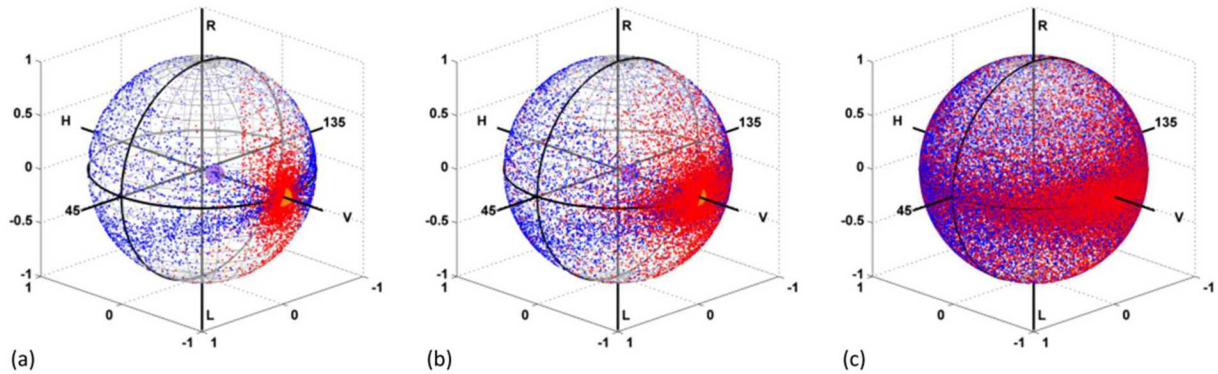

Figure 28: Scattered Stokes parameter values for incident linearly polarized light after (a) 1, (b) 2, and (c) 10 scattering events for a scattering environment consisting of particles with diameter 3.0 μm and an illuminating wavelength of 543.5 nm. This figure shows the first 100,000 photons' resulting Stokes parameters after each scattering event; forward-scattered photons are shown in red and backscattered photons are shown in blue. The resulting cumulative Stokes state, for the forward or backscattered photons, is shown as large orange or purple spheres.

B) Isotropically Scattering Environment (Rayleigh Regime): Linear Polarization

The normalized angular scattering for the 0.1 μm particle is shown on the polar plots in Figure 29. This plot is similar in design to the plots in Figure 26. However, for the isotropic scattering particle, the parallel and perpendicular polarizations scattering are distinct. The isotropic scattering particle has a much larger amount of backscattering compared to the forward-scattered particles. After any single scattering event, roughly 42 percent of the incident photons will be backscattered for the isotropically scattering environment.

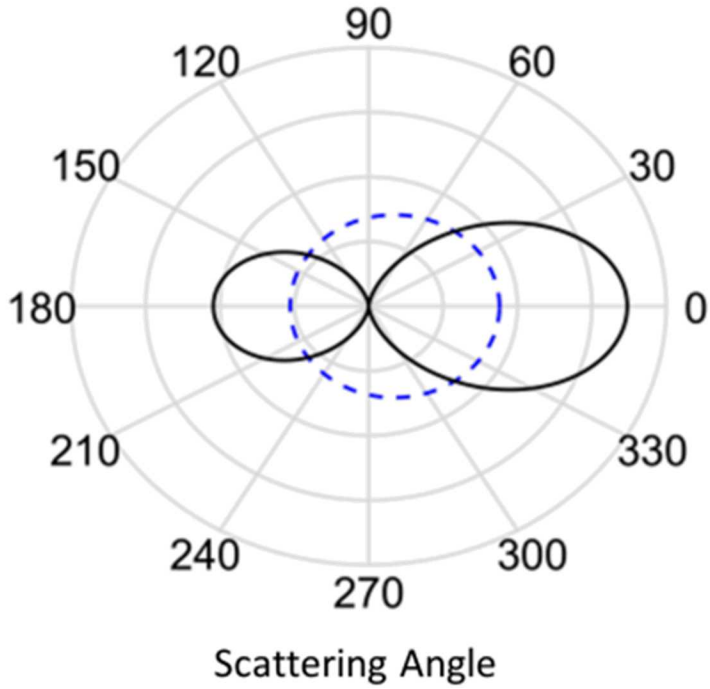

Figure 29: Scattering profile for a particle size of 0.1 μm. Perpendicular and parallel incident polarization states scattering are plotted as a solid black and dashed blue curves.

Figure 30 shows the results for incident linearly polarized scattered photons after one (a), two (b), and ten (c) scattering events for the isotropic scattering particle size 0.1 μm. The results for the isotropic scattering environment are drastically different than the forward-scattering environments. After the first scattering event (a), forward (red) and backscattered (blue) photons remain along the equator of the Poincaré sphere, thus linearly polarized states. The cumulative forward (orange) and backscattered (purple) Stokes states are slightly depolarized for the isotropic scattering environment. Although there appear to be a multitude of states around the equator, the cumulative states show the majority of the scattered photons remain near the initial location on the Poincaré sphere but have moved just inside the surface of the sphere, DoP < 1. After two scattering events (b), the photons Stokes parameters remain near the equator but the cumulative forward and backscattered Stokes states are more depolarized and move toward the center of the Poincaré sphere. Both the cumulative forward and backscattered Stokes states depolarize along the S_1 axis. After ten scattering events (c), the forward and backscattered states are evenly distributed around the equator of the Poincaré sphere. The cumulative forward and backscattered Stokes state are both at the origin and thus completely depolarized, DoP = 0.

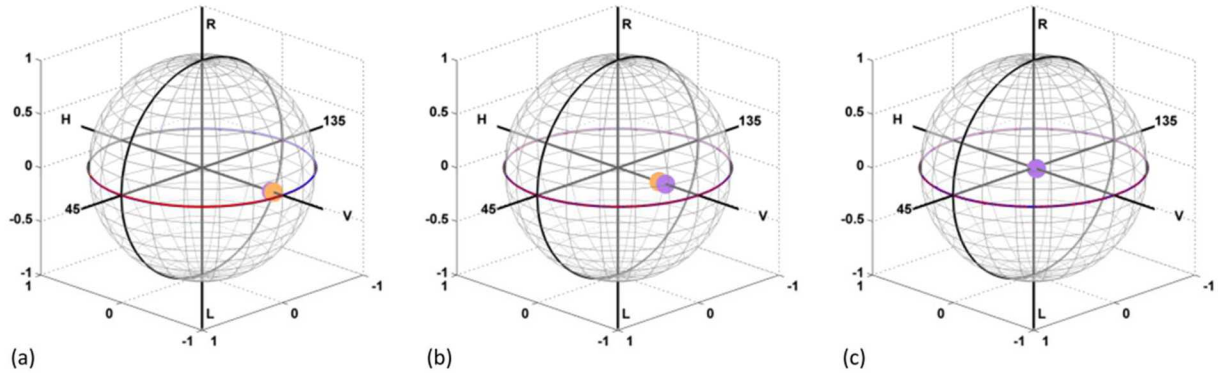

Figure 30: Scattered Stokes parameter values for incident linearly polarized light after (a) 1, (b) 2, and (c) 10 scattering events for a scattering environment consisting of particles with diameter 0.1 μm and an illuminating wavelength of 543.5 nm. This figure shows the first 100,000 photons' resulting Stokes parameters after each scattering event; forward-scattered photons are shown in red and backscattered photons are shown in blue. The resulting cumulative Stokes state, for the forward or backscattered photons, is shown as large orange or purple spheres.

Circularly Polarized Initial Illumination

The incident right circularly polarized state for this next set of simulations is located at the positive z axis of the Poincaré sphere. The incident photon's initial polarization state is plotted on the Poincaré sphere in Figure 31. The initial Stokes state is located at the center of the large orange sphere. All one million photons for this circular polarization state started in this position on the Poincaré sphere.

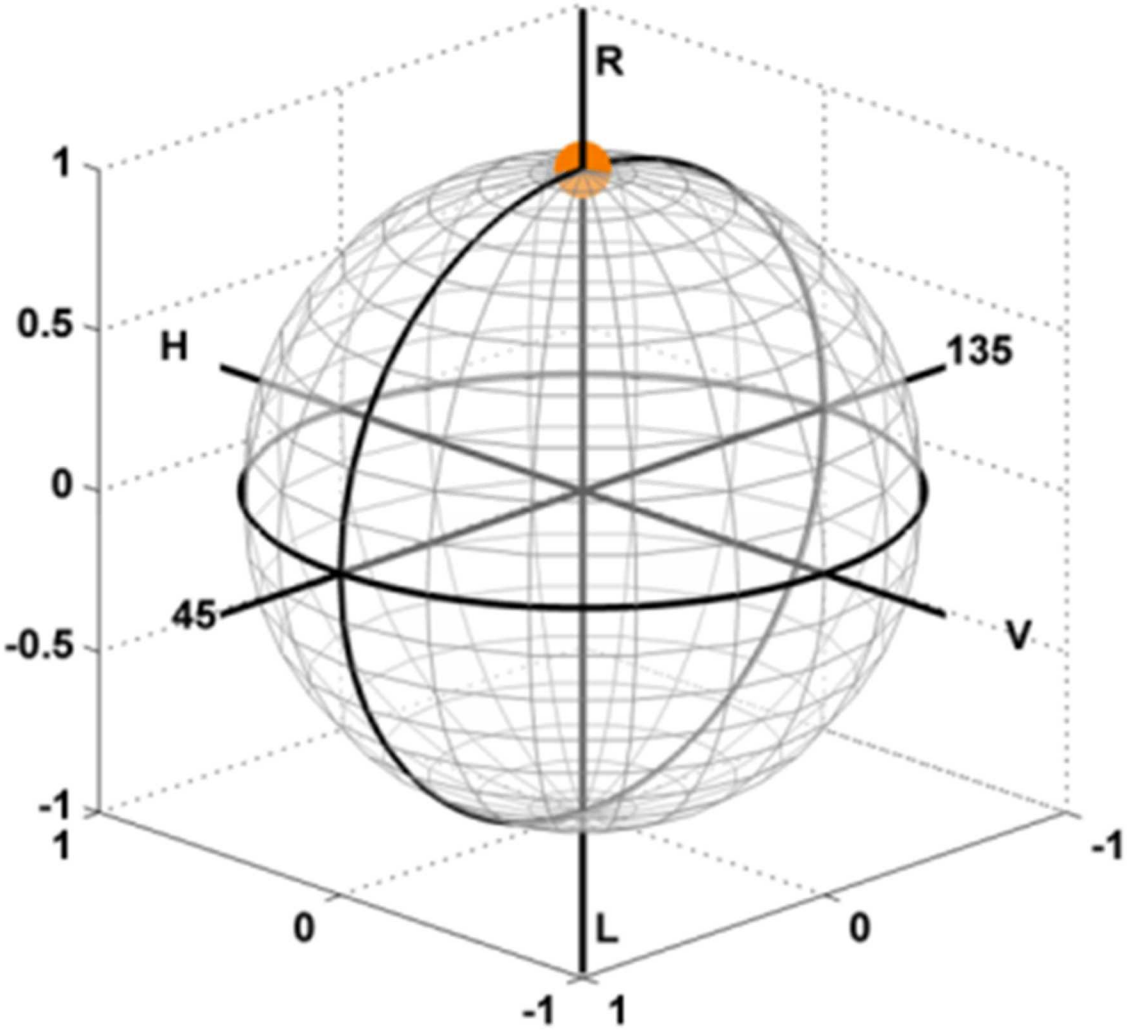

Figure 31: Poincaré sphere representation of right circularly polarized incident light. (Orange sphere represents location.)

As in the previous linear polarization case, we chose the first one hundred thousand photons, from the incident one million, for each of the following plots. The same plotting scheme is utilized: red for individual forward-scattered photons, blue for individual backscattered photons, the orange sphere represents the cumulative Stokes state for forward scattering, and the purple sphere represents the cumulative Stokes state for backscattering.

A) Isotropically Scattering Environment (Rayleigh Regime): Circular Polarization

Figure 32 shows the results for incident circularly polarized scattered photons after one (a), two (b), and ten (c) scattering events for the isotropic scattering particle size 0.1 µm. After the first scattering event (a), the forward (red) scattered photons maintain their right handedness but are spread around the entire positive S_3 hemisphere. Conversely, the backscattered (blue) photons reverse handedness and spread around the entire negative S_3 hemisphere. Both forward and backscatter states modify to a plethora of polarization states. Although it is not apparent from the plot, the cumulative forward (orange) and backscattered (purple) Stokes states are only somewhat depolarized. The cumulative states are on the S_3 axis but have moved just below the surface of the Poincaré sphere. The backscattered cumulative state has also flipped handedness. After two scattering events (b), the forward and backscattered photons Stokes parameters are intermixed on the entire Poincaré sphere. The forward and backscatter photons are no longer clearly separated by handedness. The cumulative forward and backscattered Stokes states are now highly depolarized. The cumulative forward-scattered Stokes state is still right-handed and the cumulative backscattered Stokes state is still left-handed. After ten scattering events (c), both forward and backscattered photons have migrated toward the equator and have lost most of their handedness. The cumulative forward and backscattered Stokes states are completely depolarized and located at the origin, DoP = 0. As the number of scattering events increases, circularly polarized photons evolve into a collection of linearly polarized states, resulting in completely depolarized cumulative forward and backscattered states.

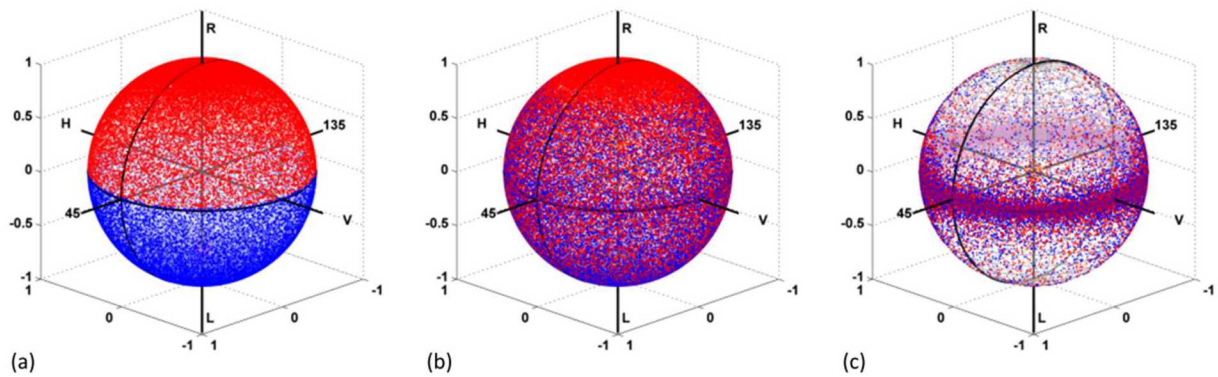

Figure 32: Scattered Stokes parameter values for incident circularly polarized light after (a) 1, (b) 2, and (c) 10 scattering events for a scattering environment consisting of particles with diameter 0.1 µm and an illuminating wavelength of 543.5 nm. This figure shows the first 100,000 photons' resulting Stokes parameters after each scattering event; forward-scattered photons are shown in red and backscattered photons are shown in blue. The resulting cumulative Stokes state, for the forward or backscattered photons, is shown as large orange or purple spheres.

The plots in Figure 30 and Figure 32 show linear and circular polarization's modification due to the isotropically scattering environment after individual scattering events. The evolution of the cumulative forward and backscattered DoP plots, as a function of scattering event, are shown in Figure 33.

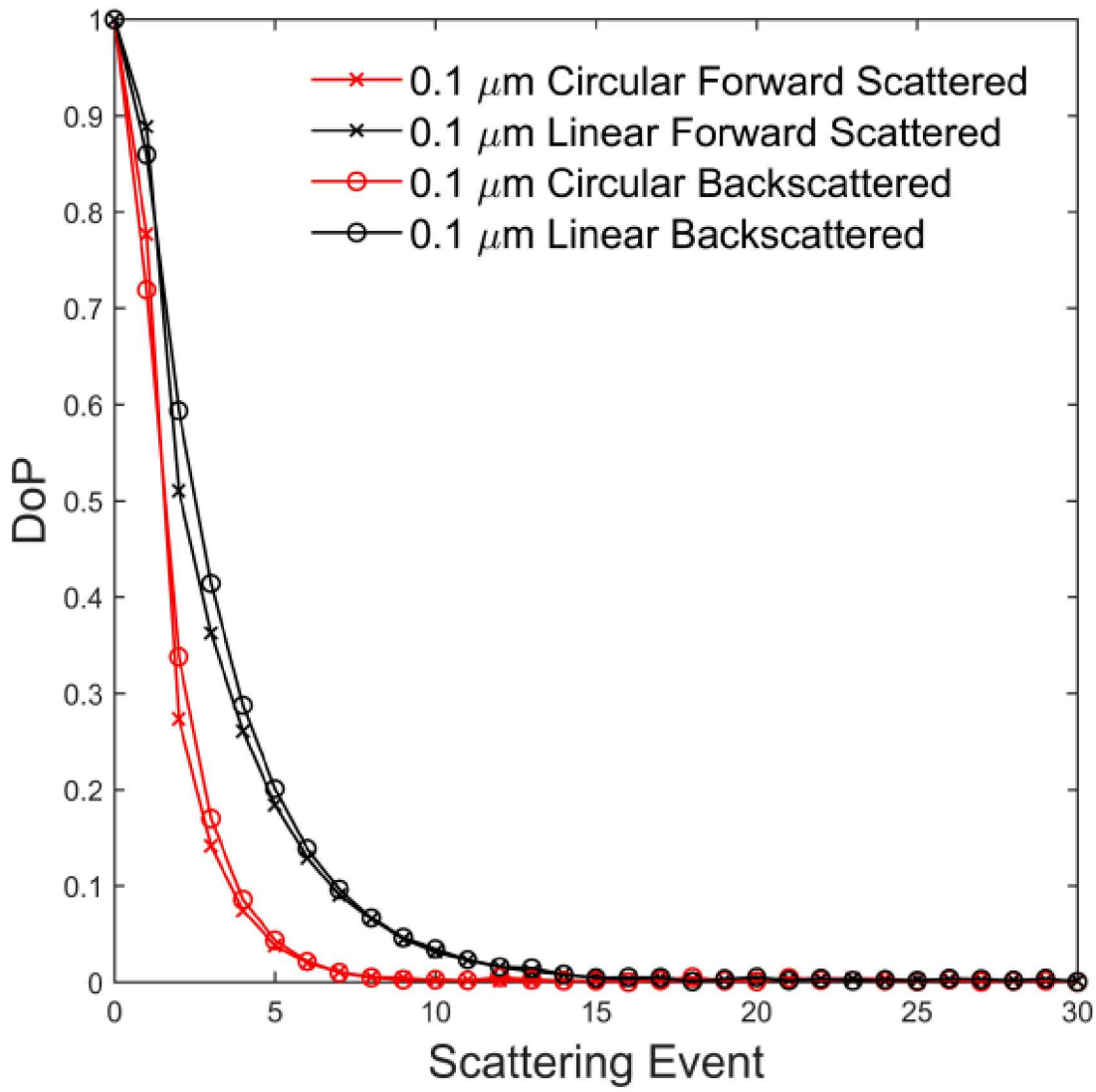

Figure 33: Cumulative DoP, for forward (x's) and backscattered (o's) photons, from circularly (red) and linearly (black) polarized incident polarization states versus number of scattering events. Both linear and circular forward and backscattered photons depolarize rapidly as a function of scattering event. Circularly polarized light is completely depolarized after merely eight scattering events while linear polarization is completely depolarized after fourteen scattering events.

The initial DoP for forward or backscattered photons in this plot is set to 1, purely polarized. Even though linear polarization is superior for this isotropic scattering environment, both linear and circular forward and backscattered photons depolarize rapidly as a function of scattering event. Circularly polarized light is completely depolarized after merely eight scattering events while linear polarization is completely depolarized after fourteen scattering events.

B) Forward-scattering Environments: Circular Polarization

Figure 34 and Figure 35 show the results for incident circularly polarized scattered photons after one (a), two (b), and ten (c) scattering events for the forward-scattering particle sizes 2.0 μm (Figure 34) and 3.0 μm (Figure 35). The forward-scattering environments for both the linear as well as circular incident polarizations exhibit a very different behavior than the isotropic case. For this incident circular polarization, after the first scattering event (a), forward-scattered photons remain close to their initial pole location on the Poincaré sphere. The forward-scattered photons' cumulative Stokes state is nearly purely polarized, DoP ~ 1. The backscattered photon's Stokes parameters are spread out around the Poincaré sphere more than the forward-scattered photons, but the Stokes parameters remain in the same handedness. As the forward-scattering particle size increases the backscattered Stokes parameters fill more of the hemisphere. The resulting cumulative backscattered Stokes state is depolarizing. Circularly polarized light tends to remain nearly purely polarized if forward-scattered but is slightly depolarized if backscattered. Remember that after one scattering event, just over 1 percent of the incident photons are backscattered for each of the forward-scattering particle environments as was illustrated in Figure 26. After two scattering events (b), the photons' Stokes parameters for both forward and backscattering are spread around the Poincaré sphere slightly more so than after one scattering event. The cumulative forward-scattered Stokes state for all the forward-scattering particle environments remain close to the initial polarization's location and is still nearly purely polarized. The forward-scattered photons' Stokes parameters remain in a cap packed near the R pole, spreading down from the pole location. The cumulative backscattered Stokes state is slightly more polarized after two scattering events than after one scattering event. Photons that are backscattered largely maintain right-handed helicity but fill more of the hemisphere than after one scattering event. After ten scattering events (c), the forward-scattered photons' Stokes parameters are spread out on the Poincare sphere more so than after two scattering events. Even with this increased spreading, the Stokes parameters remain in a cap near the R circular pole and are still highly polarized. The backscattered Stokes parameters are more spread out and nearly fill the entire upper hemisphere. Although it is not visible in the figures, the cumulative forward-scattered Stokes state is located just under the R pole cap and is highly polarized. The cumulative backscattered Stokes state is also highly polarized. Circularly polarized incident light maintains a high DoP, for both forward and backscattered photons, through a large number of scattering events for the forward-scattering environments.

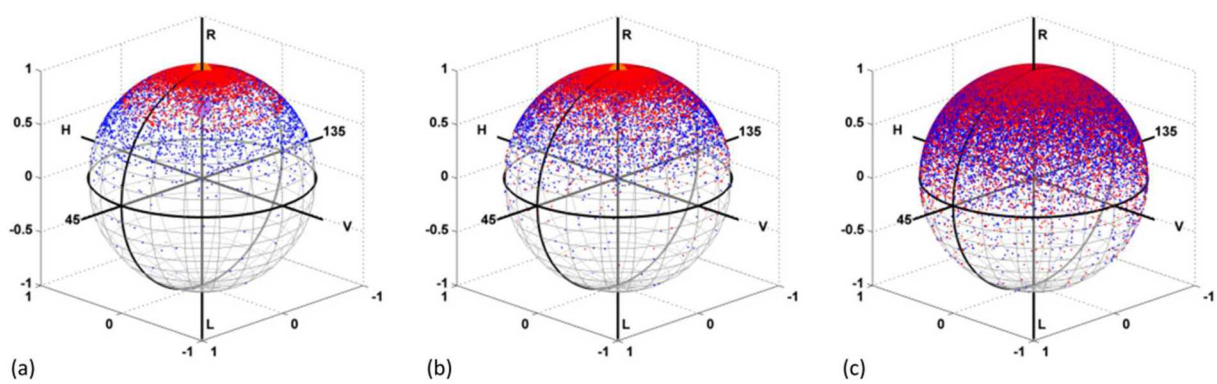

Figure 34: Scattered Stokes parameter values for incident circularly polarized light after (a) 1, (b) 2, and (c) 10 scattering events for a scattering environment consisting of

particles with diameter 2.0 μm and an illuminating wavelength of 543.5 nm. This figure shows the first 100,000 photons' resulting Stokes parameters after each scattering event; forward-scattered photons are shown in red and backscattered photons are shown in blue. The resulting cumulative Stokes state, for the forward or backscattered photons, is shown as large orange or purple spheres.

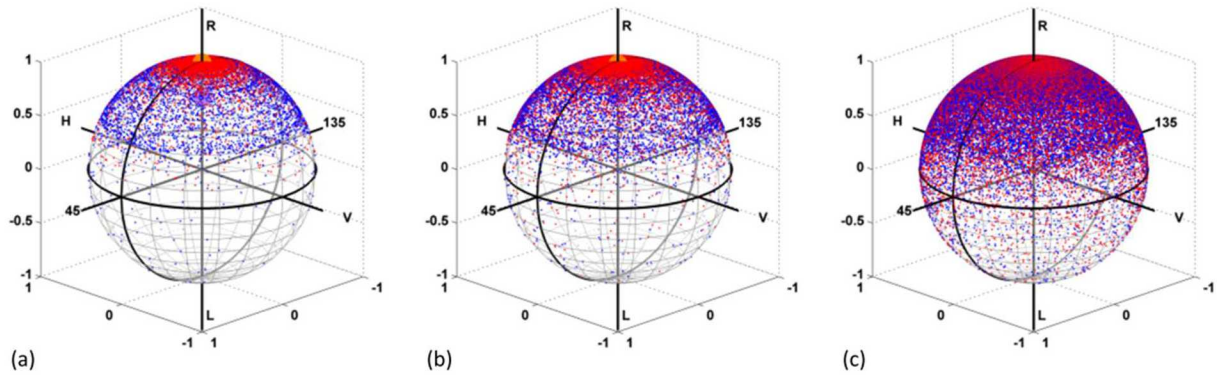

Figure 35: Scattered Stokes parameter values for incident circularly polarized light after (a) 1, (b) 2, and (c) 10 scattering events for a scattering environment consisting of particles with diameter 3.0 μm and an illuminating wavelength of 543.5 nm. This figure shows the first 100,000 photons' resulting Stokes parameters after each scattering event; forward-scattered photons are shown in red and backscattered photons are shown in blue. The resulting cumulative Stokes state, for the forward or backscattered photons, is shown as large orange or purple spheres.

The plots in Figure 27 and Figure 28 and Figure 34 and Figure 35 show linear and circular polarization's modification due to the forward-scattering environments after individual scattering events. The evolution of the cumulative forward and backscattered DoP plots, as a function of scattering event, are shown in Figure 36.

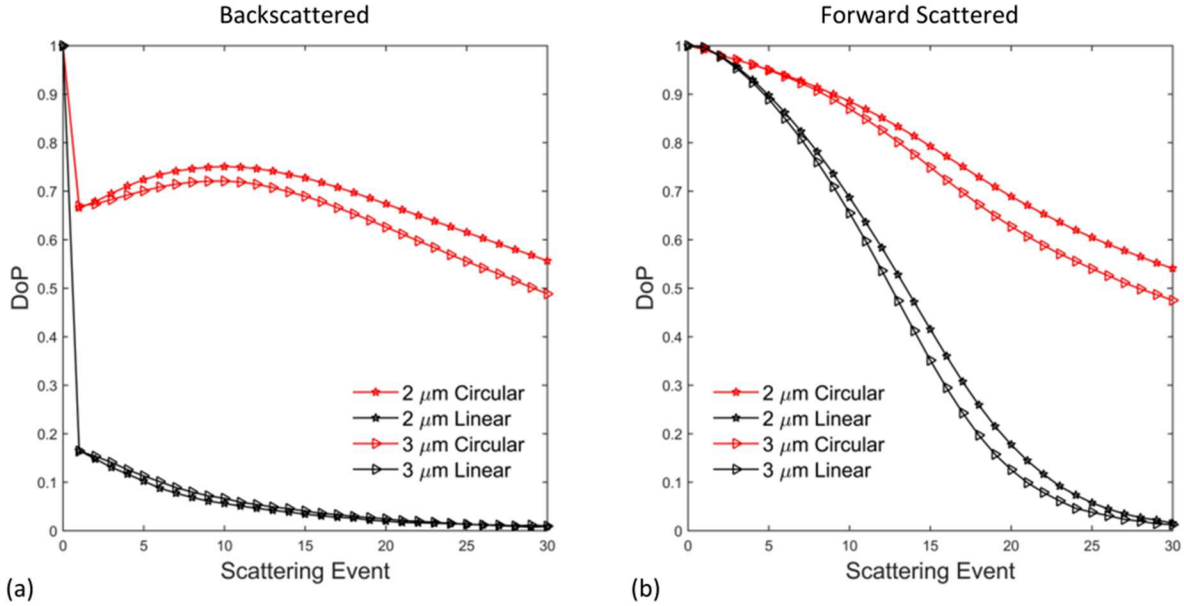

Figure 36: Cumulative DoP, for (a) backscattered and (b) forward-scattered photons, from circularly (red) and linearly (black) polarized incident polarization states versus number of scattering events. The two particle sizes are plotted as follows: 2.0 μm is plotted with

stars and 3.0 μm is plotted with triangles. Forward and backscattered light from incident circularly polarized light for the forward-scattering environments maintains its DoP and therefore persists through a larger number of scattering events.

Figure 36 clearly shows that circular polarization maintains its DoP better than linear polarization. For the forward-scattering environments, circular polarization persists through increasing scattering events better than linear polarization for either forward or backscattered photons. In the figure, the initial DoP for forward or backscattered photons is set to 1, purely polarized. In Figure 36 (a), after only one scattering event backscattered linear polarized light is highly depolarized. Backscattered circular polarized light is also depolarized after one scattering event, although not to the extent of linear polarization. As the number of scattering events increases, linearly polarized light's DoP decreases to a completely unpolarized state. Conversely, backscattered circular polarized light's DoP increases as the number of scattering events increases. After about ten scattering events, circular polarized backscattered light peaks to its largest DoP. After this, circular backscattered photon's DoP begins to decrease but remains highly polarized even after 30 scattering events. It is difficult to understand the significance of this initial depolarization and then increase in DoP for backscattered circular polarized photons from the forward-scattering environments since the relative number of backscattered photons is so small. After one scattering event just over 1 percent of the light is backscattered for these forward-scattering environments. After successive scattering events the number of backscattered photons increases and there are a larger number of photons for the ensemble cumulative Stokes state. In Figure 36 (b), circularly incident forward-scattered photons remain highly polarized through a larger number of scattering events. The linearly polarized incident photons remain highly polarized for small numbers of scattering events but depolarize more quickly than circularly polarized photons. Circular polarization remains largely polarized as the number of scattering events increases while linear polarization depolarizes quickly by evolving into a plurality of linearly polarized states. Overall, forward and backscattered light from incident circularly polarized light for the forward-scattering environments maintains its DoP and therefore persists through a larger number of scattering events.

Conclusions

This work quantitatively and qualitatively presents the evolution of linear and circularly polarized light as it scatters throughout both isotropic (Rayleigh regime) and forward-scattering environments. Circularly polarized light persists through a larger number of scattering events longer than linearly polarized light for all forward-scattering environments. In this forward-scattering environment, circular polarization's increased persistence occurs for both forward and backscattered light. The simulated forward-scattering environments modeled polystyrene microspheres in water with particle diameters of 2.0 μm and 3.0 μm. The scattering profiles of these environments are consistent with advection (marine) and radiation fog at infrared wavelengths. The evolution of the polarization states as they scatter throughout the various environments are illustrated on the Poincaré sphere after one, two, and ten scattering events.

We also model a more isotropically scattering environment with a 0.1 μm particle diameter. In this isotropic scattering regime circularly and linearly polarized light depolarize rapidly. Linear polarization persists better for this isotropic environment. Incident linearly polarized light depolarizes into various other linearly polarized states while incident circularly

polarized light depolarizes into a multitude of elliptical states initially and then evolves into more and more linear polarized states.

For all of the forward-scattering environments, circular polarization maintains a high degree of polarization, and remains in a range of states near the incident polarization state, throughout a large number of scattering events. Linear polarization depolarizes more rapidly into other linearly polarized states than into elliptical states, leading to a more highly depolarized cumulative state compared to that of circular polarization. This work shows clearly that circular polarization is superior to linear polarization in maintaining its DoP as a function of scattering event, and persisting through the larger forward-scattering particle environments. Circularly polarized light slowly, and smoothly degrades from its initial state, maintaining the same handedness, while linearly polarized light abruptly depolarizes into a plethora of other linear polarization states. This work quantifies the polarization persistence and memory of circularly polarized light in forward-scattering environments; and for the first time, details the evolution of both circularly and linearly polarized states through scattering environments.

6. EXPERIMENTAL RESULTS: POLYSTYRENE MICROSPHERES IN WATER

Introduction:

The following chapter is a set of experimental results for polarization persistence in a laboratory scattering environment. Included are confirming simulation results for the same environments. This chapter presents experimental and simulation results for polarization persistence measures made through a laboratory scattering environment consisting of polystyrene microspheres in water. These experiments show that circular polarization maintains its degree of polarization better than linear polarization for the forward scattering environment. This confirms what we showed in Chapter 3 and 4. Throughout the experimental process and subsequent simulations, we also show that circular polarization is more tolerant of variations in the optical system measuring persistence. Circular polarization proves to not only persist better than linear polarization but also be more flexible to use in a range of optical systems without degraded performance.

The following chapter is taken directly from a submitted paper that will be published in Applied Optics with the title "Effects of collection geometry variations on linear and circular polarization persistence in both isotropic-scattering and forward-scattering environments" [54].

1. Introduction:

Optical sensing in environments such as fog and dust are challenging due to the highly scattering nature of these environments. Polarized light's persistence through highly scattering environments can mitigate these effects and increase sensing range and target detection. The persistence of polarized light is not only dependent on the scattering environment but also the optical collection system. In this work we present simulation and experimental results showing circular polarization is more tolerant of optical collection geometry variations, such as field of view and collection area, than linear polarization for forward-scattering environments. Additionally, we present results for an isotropic-scattering (Rayleigh regime) environment. For the isotropic-scattering environment, linear polarization has a small persistence benefit over circular polarization but both polarization states are susceptible to optical collection geometry variations. We have previously shown, through simulation, that circular polarization maintains its degree of polarization (DoP) and thus persists better than linear polarization in forward-scattering environments such as fog [23], [38], [49]. Our work showed circular polarization's increased persistence for fog and dust environments over broad wavebands in the infrared, and the evolution of circular and linear polarization as light is scattered throughout isotropic-scattering and forward-scattering environments [4], [5], [35]. The results presented here experimentally confirm our previous simulation results as well as demonstrate that circular polarization is much more tolerant of variations in the optical collection geometry. These results show that circular polarization is ideal for use with a range of optical configurations when measurement of signal persistence is important.

There is limited previous work investigating the variation in polarization persistence for varying collection geometries in scattering, or turbid, environments. The majority of publications focus on medical applications such as imaging through tissue. Ghosh, et al. investigated the effects of changes in the collection half angle when measuring depolarization in tissue phantoms [55]. They experimentally measured the transmitted DoP for incident linear and circular polarization through four solutions of polystyrene microspheres in water. Two mean

particle diameters were investigated, 0.11 and 1.08 μm, with different optical thicknesses, 8.3 for the 0.11 μm diameter and 15 for the 1.08 μm diameter. The optical thickness was maintained but two cuvettes were used with different lengths corresponding to 5 and 10 mm. This meant each sample had different scattering coefficients in order to maintain the same optical thickness. Collection half angles were varied from 2.5 to 16.4 degrees for the transmitted DoP measurements. Ghosh, et al.'s results show the DoP decreases for all samples and polarization states as the collection angle increased. They also showed that the depolarization was more pronounced for circular polarized light with the smaller particle size (isotropic-scattering) but the opposite was true for the larger size (forward-scattering). These results are a starting point but are limited to small collection angles. Moreover, the effects of varying collection angle and collection area are not investigated separately.

Similarly, Gomes, et al. [56], Gomes, et al. [57], and Turzhitsky, et al. [58] all investigated effects of varying collection geometries, both collection angles and collection area, on penetration depth and depolarization ratio when utilizing backscattered polarization-gating. Their results utilize polarization Monte Carlo simulations with various scattering environments that simulate tissue characteristics and examine only linearly polarized light. They showed that the penetration depth decreases with increasing collection half-angle, and increases with increasing collection area. Similar results are shown for the depolarization ratio. These works investigate the variations in collection half-angle and collection area but are limited to linearly polarized light, as well as backscattered polarization signals.

This work presents collection geometry variations of transmitted polarization persistence for both linear and circular polarized light, in both isotropic-scattering and forward-scattering environments. This article is organized as follows: Section 2 covers background on polarization, the Monte Carlo simulations we perform, and a description of the simulation and experimental scattering environments; Section 3 describes the simulation results for varying collection geometries in both isotropic-scattering and forward-scattering environments; Section 4 presents the experimental setup and results; and Section 5 ends with some final conclusions.

2. Background:

The Stokes formalism to define polarization is used throughout this work due to the need to describe depolarized signals. Polarization of light is defined by the Stokes parameters (S_0, S_1, S_2, and S_3) which are a part of the Stokes vector,

$$\vec{\boldsymbol{S}} = \begin{bmatrix} S_0 \\ S_1 \\ S_2 \\ S_3 \end{bmatrix} = \begin{bmatrix} \langle E_\parallel E_\parallel^* + E_\perp E_\perp^* \rangle \\ \langle E_\parallel E_\parallel^* - E_\perp E_\perp^* \rangle \\ \langle E_\parallel E_\perp^* + E_\perp E_\parallel^* \rangle \\ i \langle E_\parallel E_\perp^* - E_\perp E_\parallel^* \rangle \end{bmatrix} \propto \begin{bmatrix} I_H + I_V \\ I_H - I_V \\ I_{45} - I_{135} \\ I_R - I_L \end{bmatrix}. \tag{1}$$

The S_0 Stokes parameter corresponds to the total intensity of the light signal, S_1 defines the preference for horizontal or vertically linearly polarized light, S_2 defines the preference for linearly polarized light at an angle of plus or minus 45 degrees, and lastly S_3 defines the preference for the light to be right or left circularly polarized. The Stokes vector describes all types of light whether it is polarized, unpolarized, or something in-between which is called partially polarized. In order to determine how polarized a light signal is the Degree of Polarization (DoP) is used. The DoP determines the percentage of the light that is purely polarized and defined by the equation,

$$DoP = \frac{\sqrt{{S_1}^2 + {S_2}^2 + {S_3}^2}}{S_0}. \quad (2)$$

Purely polarized light has a DoP equal to 1 and completely depolarized light has a DoP equal to 0. Thus, partially polarized light has a DoP greater than 0 and less than 1. When purely polarized light transmits into a scattering environment it can be depolarized. The transmitted DoP defines the amount of the incident light that persists in the intended incident polarization state.

In this work we investigate the effect optical system characteristics, such as collection angle and collection area, have on polarization persistence measurements. In order to simulate a wide range of characteristics a polarization-tracking Monte Carlo program was utilized. The background of the Monte Carlo simulation have been described in detail previously and will not be described thoroughly here [3], [5], [24], [35], [59]. Overall, the simulation tracks the cumulative polarization state of incident photons as they scatter throughout the scattering environment until they are collected by a defined optical system. The scattering environment has a defined length but the lateral extent of the scattering environment is infinitely wide.

2.1 Simulation and Experimental Scattering Environment:

We investigated two scattering environments for both simulation and experiment. These environments correspond to isotropic-scattering (Rayleigh-regime) and forward-scattering environments. The scattering environments consisted of polystyrene microspheres in water. Polystyrene microspheres with a mean diameter of 0.0824 μm and a standard deviation of 0.006 μm were used for the isotropic-scattering environment and microspheres with a mean diameter of 1.925 μm and standard deviation of 0.042 μm were used for the forward-scattering environment. The simulation and experimental wavelength was 543.5 nm, the wavelength of a green HeNe laser. Polystyrene's refractive index at this wavelength is 1.597 [60]. The size parameter of a scattering environment determines whether it is isotropic-scattering or forward-scattering; and is defined as,

$$x = \frac{2\pi a n}{\lambda}, \quad (3)$$

where a is the radius of the scattering particle, n is the refractive index of the external medium, and λ is the vacuum wavelength of the incident light [24]. Environments with size parameters less than 1 are considered isotropic-scattering environments while environments with size parameters larger than 1 are considered forward-scattering environments. The size parameters for our simulation and experimental scattering environments are 0.635 and 14.83, respectively.

3. Simulation Results

We performed simulations for incident linear and circular polarization persistence through the previously defined scattering environments. The sensitivity or tolerance to varying the collection geometry was investigated by simulating four different collection half-angles, or angular half field of views (HFOV), and four different collection area radii. For each polarization state and each environment the HFOV was varied from 10 to 70 degrees by 20 degree increments. Similarly, the radius of collection was varied from 0.25 cm to 2cm.

3.1 Isotropic-scattering environment: 0.0824 μm diameter polystyrene microspheres in water

Figure 37 (incident linear polarization) and Figure 38 (incident circular polarization) show the Monte Carlo simulation results for varying collection geometries for the isotropic-scattering environment. Each figure consists of four graphs corresponding to increasing angular collection: a) 10° HFOV, b) 30° HFOV, c) 50° HFOV, and d) 70° HFOV. Each graph has four plots corresponding to increasing circular collection areas with radii 0.25, 0.5, 1, and 2 cm.

For the isotropic-scattering environment, both polarization states are affected by varying the collection HFOV and the collection area. As the collection HFOV increases, the DoP decreases for both linear and circular polarization states. As the HFOV increases a larger number of multiply scattered photons are collected. This is also the case as the collection radius is increased, but the collected DoP decreases more rapidly for larger collection areas compared to increasing the HFOV. The isotropic-scattering environment scatters photons over broad angles. For larger collection radii, a larger number of collected photons are those that scattered off the incident beam's axis.

Regardless of the collection geometry, circular polarized light exhibits slightly smaller signal persistence than linear polarization for the isotropic-scattering environment in these results. Both circular and linear polarizations are affected by the variation of the optical collection area and collection angle, although the collection area has a larger effect. The isotropic-scattering environment scatters photons at large angles and thus more depolarized photons are scattered off the axis of the incident beam.

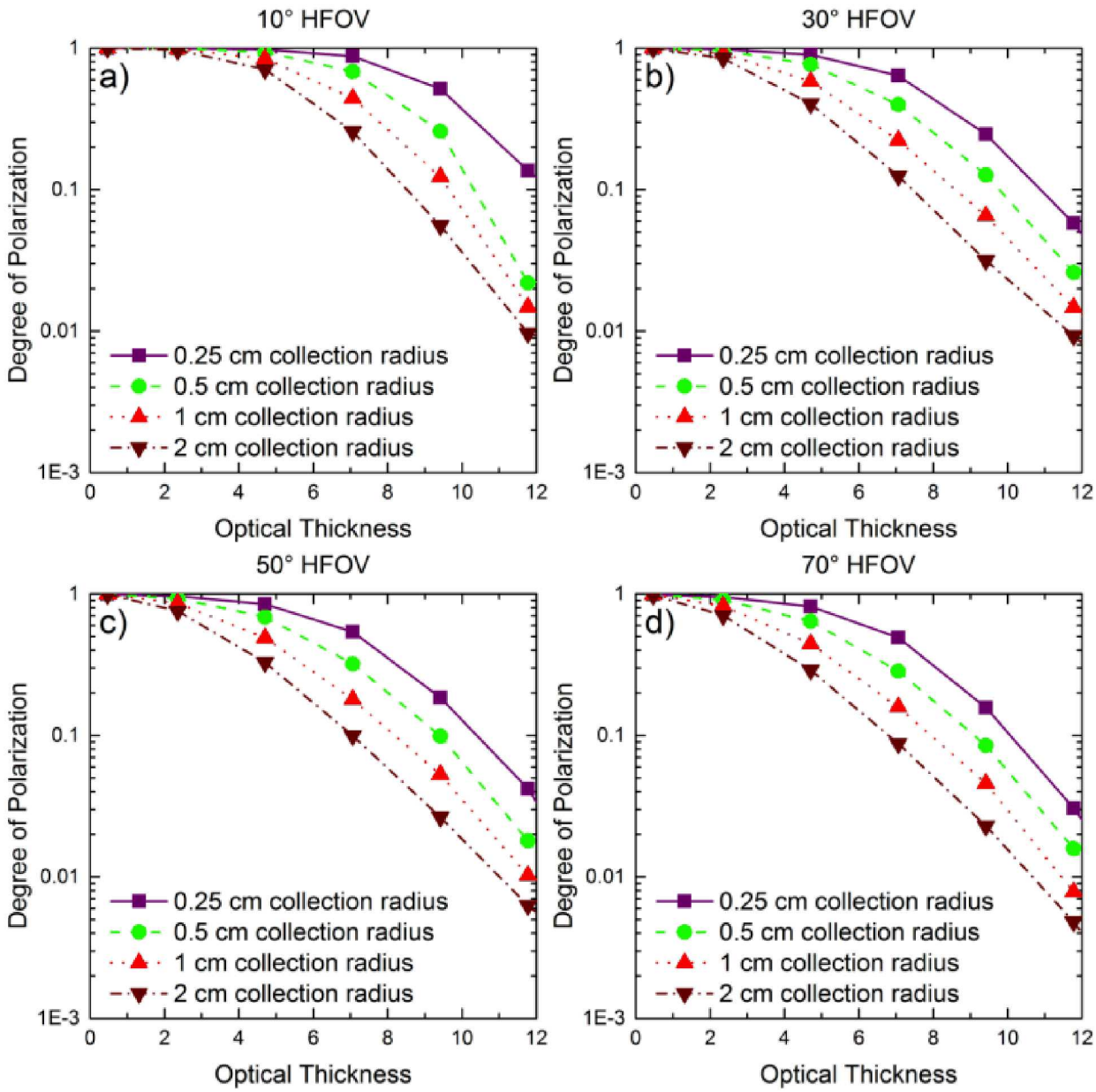

Figure 37: DoP versus optical thickness changes with variation of the angular and area collection geometry for incident linearly polarized light for an isotropic-scattering environment of 0.0824 μm polystyrene microspheres in water. Radial area collection variation from 0.25 to 2 cm on the output face for a) 10° HFOV, b) 30° HFOV, c) 50° HFOV, and d) 70° HFOV.

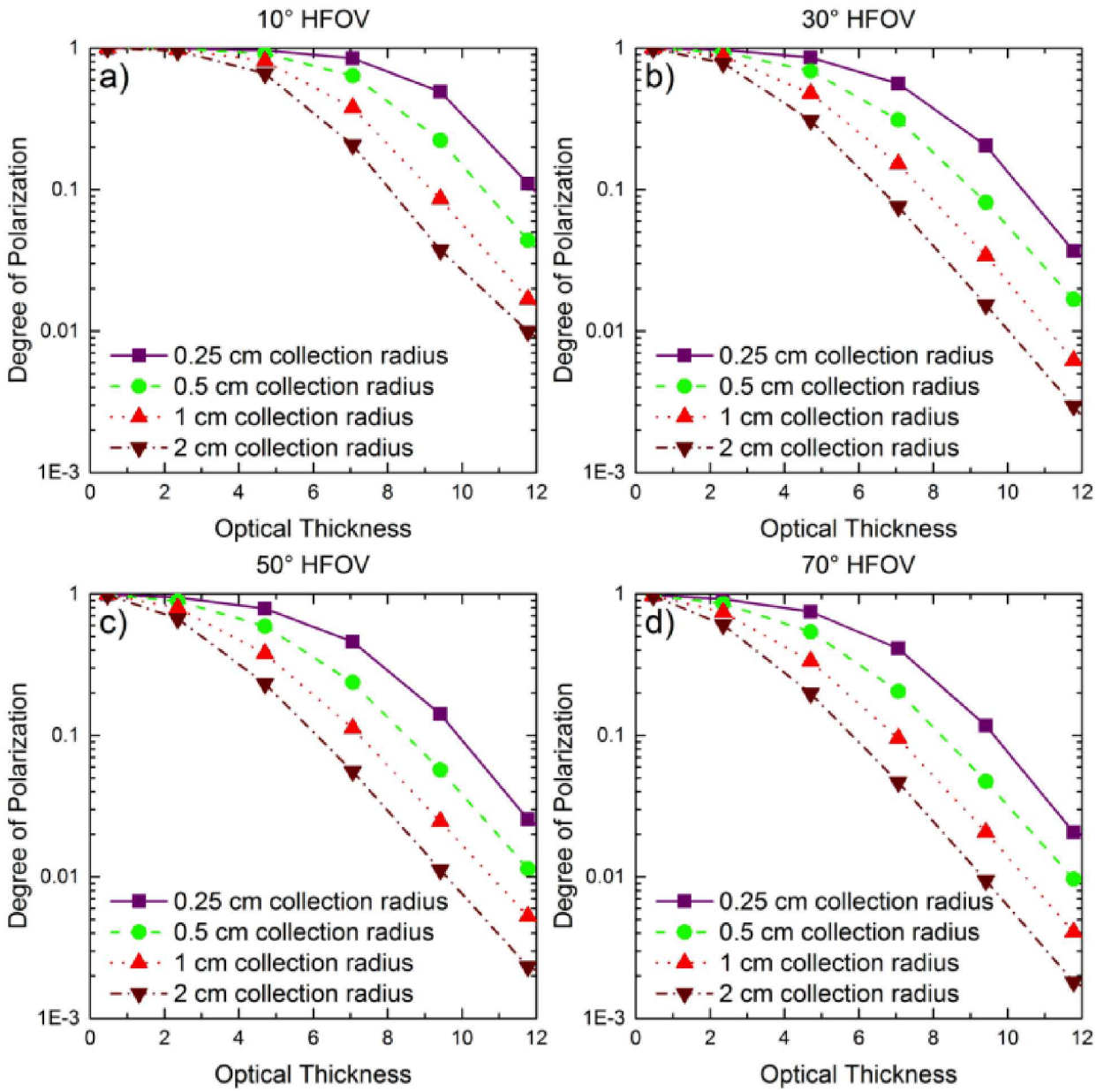

Figure 38: DoP versus optical thickness changes with variation of the angular and area collection geometry for incident circularly polarized light for an isotropic-scattering environment of 0.0824 µm polystyrene microspheres in water. Radial area collection variation from 0.25 to 2 cm on the output face for a) 10° HFOV, b) 30° HFOV, c) 50° HFOV, and d) 70° HFOV.

3.2 Forward-scattering environment: 1.925 µm diameter polystyrene microspheres in water

Figure 39 (incident linear polarization) and Figure 40 (incident circular polarization) show the Monte Carlo simulation results for varying collection geometries for the forward-scattering environment. The figure layouts are the same as those in the previous isotropic-scattering section.

The forward-scattering environment simulation results differ significantly from the isotropic-scattering case. In the forward-scattering environment, both variation of the HFOV and

the collection area decreases the collected DoP for linearly polarized light. The effect of these variations is smaller for the forward-scattering environment than the isotropic-scattering environment. As the collection HFOV increases, the collected DoP decreases but the change is small. Conversely, increasing the collection area radii causes a larger change in the collected DoP. Collection radii less than 0.5 cm show little variation, but as the collection radius increases beyond 0.5 cm the collected DoP decreases rapidly.

Circular polarization exhibits a very different behavior than linear polarization in the forward-scattering environment. When the collection HFOV and collection area are varied the collected DoP shows almost no change. The four graphs in Figure 40 look nearly identical. As the HFOV is increased the collected DoP is nearly unchanged. Circularly polarized photons multiply scattered at large angles in the forward-scattering environment remain highly polarized. Similarly, there is very small variation in the collected DoP when the collection area is increased. There is a nearly insignificant decrease in the collected DoP, less than 0.1, as the collection area is increased. Collection geometry variations hardly affect the collected DoP for incident circularly polarized light in a forward-scattering environment.

For the forward-scattering environment, we have shown that circular polarization is more tolerant of variations in the collection geometry than linear polarization. Linear polarization is more susceptible to variations in the collection area. Linear polarized photons that are scattered off the axis of the incident beam greatly affect the collected DoP. Circular polarization's superior persistence in the forward-scattering environment allows it to be more tolerant of both collection area and collection HFOV changes.

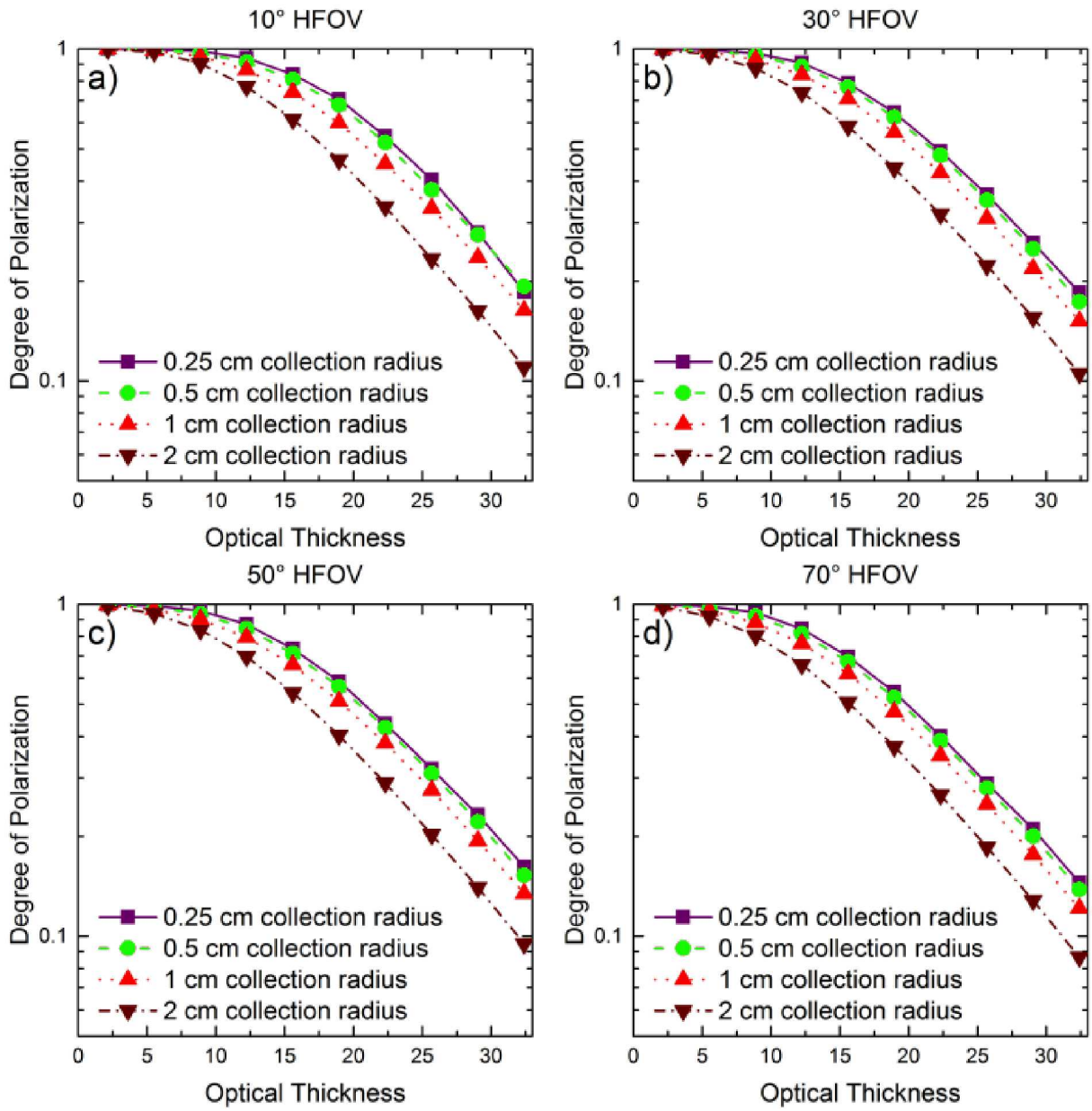

Figure 39: DoP versus optical thickness changes with variation of the angular and area collection geometry for incident linearly polarized light for a forward-scattering environment of 1.925 μm polystyrene microspheres in water. Radial area collection variation from 0.25 to 2 cm on the output face for a) 10° HFOV, b) 30° HFOV, c) 50° HFOV, and d) 70° HFOV.

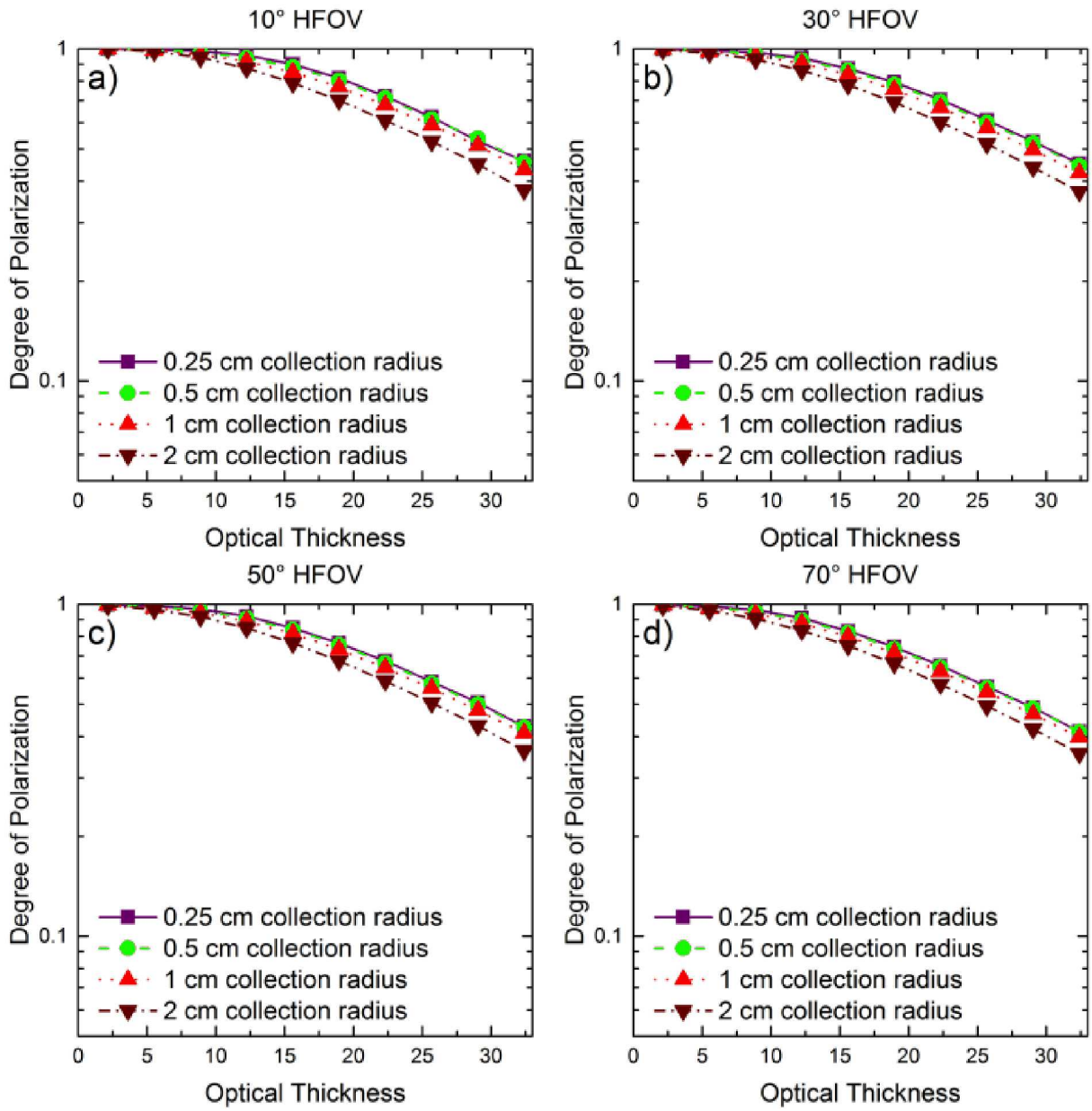

Figure 40: DoP versus optical thickness changes with variation of the angular and area collection geometry for incident circularly polarized light for a forward-scattering environment of 1.925 µm polystyrene microspheres in water. Radial area collection variation from 0.25 to 2 cm on the output face for a) 10° HFOV, b) 30° HFOV, c) 50° HFOV, and d) 70° HFOV.

4. Experimental setup and results

We performed polarization persistence measurements for both the isotropic-scattering and forward-scattering environments with circular and linear polarized illumination. The experimental setup for both polarizations is shown in Figure 41. A 5 mW HeNe laser with a wavelength of 543.5 nm acted as the illumination source. The laser was optically chopped at a frequency of 200 Hz and a lock-in amplifier was used to recover extremely small signals when the optical thickness of the scattering environment was large. Polarization generating optics

consisting of a polarizing beam cube and a quarter-wave retarder (labeled λ/4) set the incident polarization state. Upon exiting the polarizing beam cube, the laser's polarization state was vertically linearly polarized. Linearly polarized light is generated when the quarter-wave retarder's fast axis is aligned vertically; otherwise, circularly polarized light is generated when the quarter-wave retarder's fast axis is 45° from vertical. The desired polarized light is then incident normal to the front face of a glass cuvette. The front and back optical faces of the cuvette have dimensions 1 cm wide by 4 cm high. The cuvette has a length of 3 cm.

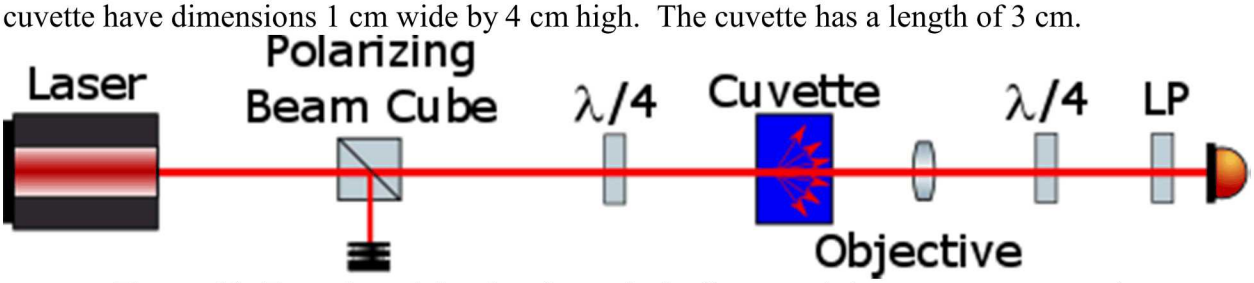

Figure 41: Experimental setup for polarization persistence measurements

The previously mentioned scattering environments, isotropic-scattering and forward-scattering polystyrene microspheres, fill the cuvette. A total volume of 6 mL of deionized water and polystyrene microsphere solution were used for each experiment. The optical thickness of the scattering environment was changed by using increasing densities of polystyrene microspheres. The optical thickness is a convenient way to compare different types and densities of scattering environments. Optical thickness, τ, is defined as,

$$\tau = \rho \sigma_{ext} L, \tag{4}$$

where ρ is the density of polystyrene microspheres, σ_{ext} is the Mie scattering extinction cross-section of the scattering particles, and L is the overall length of the scattering environment[24]. Light that propagates through the scattering environment and exits the back face of the glass cuvette was collected by an objective lens. The objective lens was a Mitutoyo infinity-corrected lens with a numerical aperture of 0.42. The objective collects scattered light which exits the back face of the cuvette in a circular collection radius of 100 μm and a HFOV of 24.83°. Collected light is collimated after passing through the objective. Polarization state analyzing optics determine the polarization of the collected light. The four Stokes parameter values are determined with a rotating quarter-wave retarder, fixed-polarizer polarimeter[50]. The polarimeter consists of a 1 cm square silicon PIN diode detector.

4.1 Isotropic-scattering environment: 0.0824 μm diameter polystyrene microspheres in water

The following results show the transmitted DoP, and thus persistent signal, of both linearly and circularly polarized light through increasing optical thicknesses of the isotropic-scattering environment of polystyrene microspheres in water. Simulation results from the same scattering environment at the same optical thicknesses are compared to the experimental results. The experimental and simulation results for the isotropic-scattering environment are shown in Figure 42.

For the isotropic-scattering environment, even after low numbers of scattering events, photons are scattered at large angles. For this environment, linearly polarized light persists better than circularly polarized light, although this is a small measured effect. Both polarization states are depolarized as the optical thickness is increased. Circularly polarized light is depolarized more than linearly polarized light but both polarization states decrease at roughly the same rate.

The simulation results are much more highly depolarized than the experimental results even at low optical thicknesses. The simulation results also show a larger separation between the DoP values for each polarization state compared to the experimental results. Despite these variations, linearly polarized light persists better than circularly polarized light though the isotropic-scattering environment, but the effect is small. The discrepancy between the simulation and experimental results is likely due to the experimental scattering environment's constraints. As stated, the cuvette used was very skinny in the lateral dimensions compared to the infinitely wide simulation environment. The length of the simulation and experimental scattering environments were the same. In the simulations, a large number of photons scattered outside the bounds of the physical cuvette dimensions are able to return. These multiply scattered photons can scatter back into the collection geometry of the objective lens. This results in a larger depolarized signal in the simulation results compared to the experimental results. Simulation results collect many more multiply-scattered, highly-depolarized photons than the experimental case for the isotropic-scattering environment. In the experimental case, collected photons are scattered only a few times, or not at all. The experimental cuvette walls limit the number of scattering events that any photon can encounter.

The cuvette's experimental constraint is why, for small optical thicknesses, simulation results for the isotropic-scattering environment have very low DoPs. As previously shown, both linear and circular polarization are susceptible to changes in the collection geometry; these experimental results also show that the polarization states measured persistence is affected by the size of the scattering environment itself. Overall, the trends seen in simulation and experiment are similar, but the experimental results are not able to match those found with an infinite slab width simulation. Linear polarization persists better than circular polarization for the isotropic-scattering environment. Persistence measurements are only able to measure photons with small numbers of scattering events with the constrained environmental dimensions, resulting in measuring only photons that are scattered over a small range of forward angles with high DoPs.

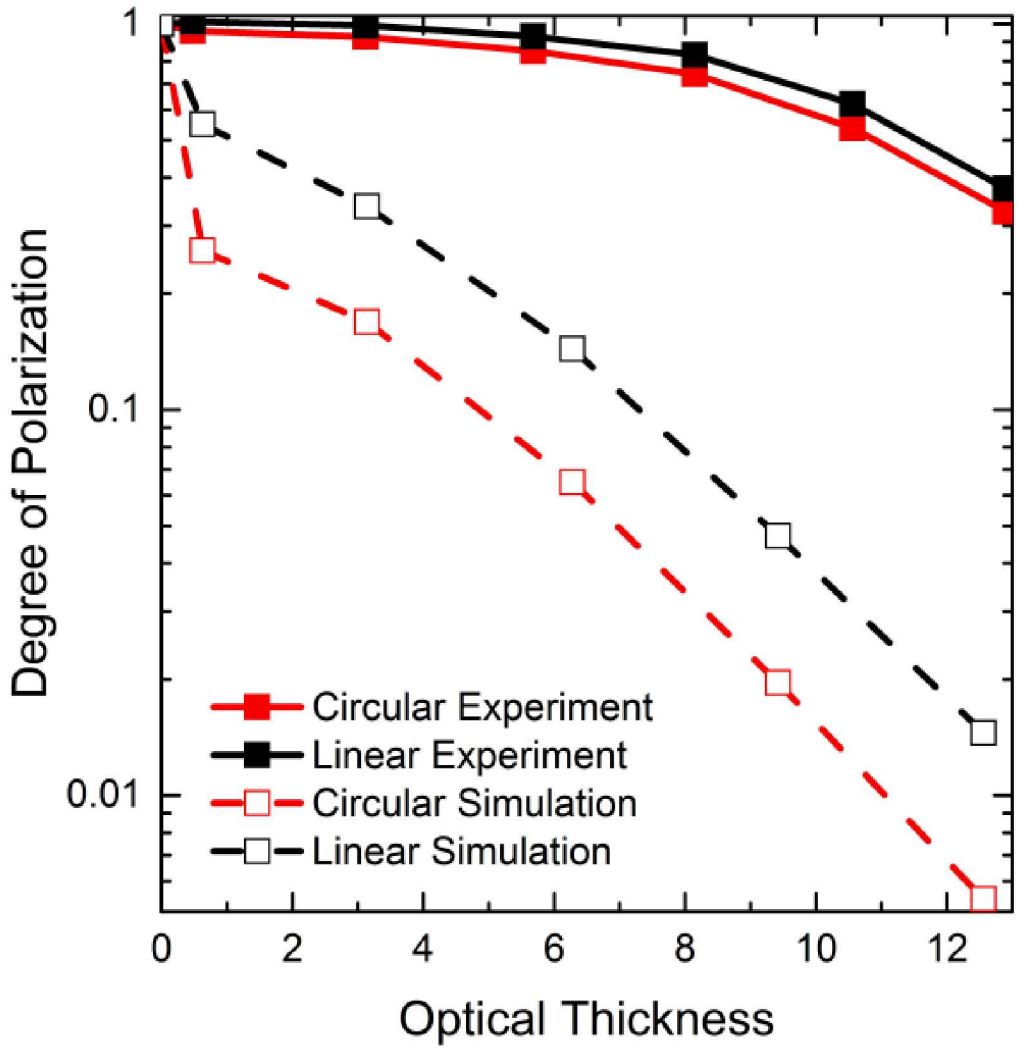

Figure 42: DoP versus optical thickness for measured and simulated isotropic-scattering environments of 0.0824 µm polystyrene spheres in water.

4.2 Forward-scattering environment: 1.925 µm diameter polystyrene microspheres in water

Experimental and simulation results for the forward-scattering environment of 1.925 µm diameter polystyrene microspheres in water are shown in Figure 43. For the forward-scattering environment, circularly polarized light persists longer than linearly polarized light. This is the case for both experimental and simulation results. The measured linear polarization's DoP is higher than that found via simulation. Similar to the isotropic-scattering case, this discrepancy is most likely due to the dimensional constraints of the cuvette used in the measurements. A comment from Freund and Kaveh regarding the polarization memory work of MacKintosh et al. addresses a similar discrepancy[39], [61]. Freund and Kaveh express that the walls of a cuvette can cause internal surface reflections that are not taken into account in simulations. The

reflections from the surfaces of the cuvette will re-inject certain portions of the scattered light and can be polarization dependent. These internal reflections are not taken into account by the simulations. It is again hypothesized here that the cuvette walls allow photons to be collected with fewer scattering events than is found in the simulations. This limits the depolarization of the measured scattered light. As Section 3 showed, circular polarization is more tolerant of changes in the collection geometry, and shown here the environmental extent. Thus, the effect of the cuvette are not as detectable for circularly polarized light in the forward-scattering environment compared to linear polarized light. Overall, circularly polarized light persists longer than linearly polarized light and is more tolerant of the experimental cuvettes surfaces for the forward-scattering environment.

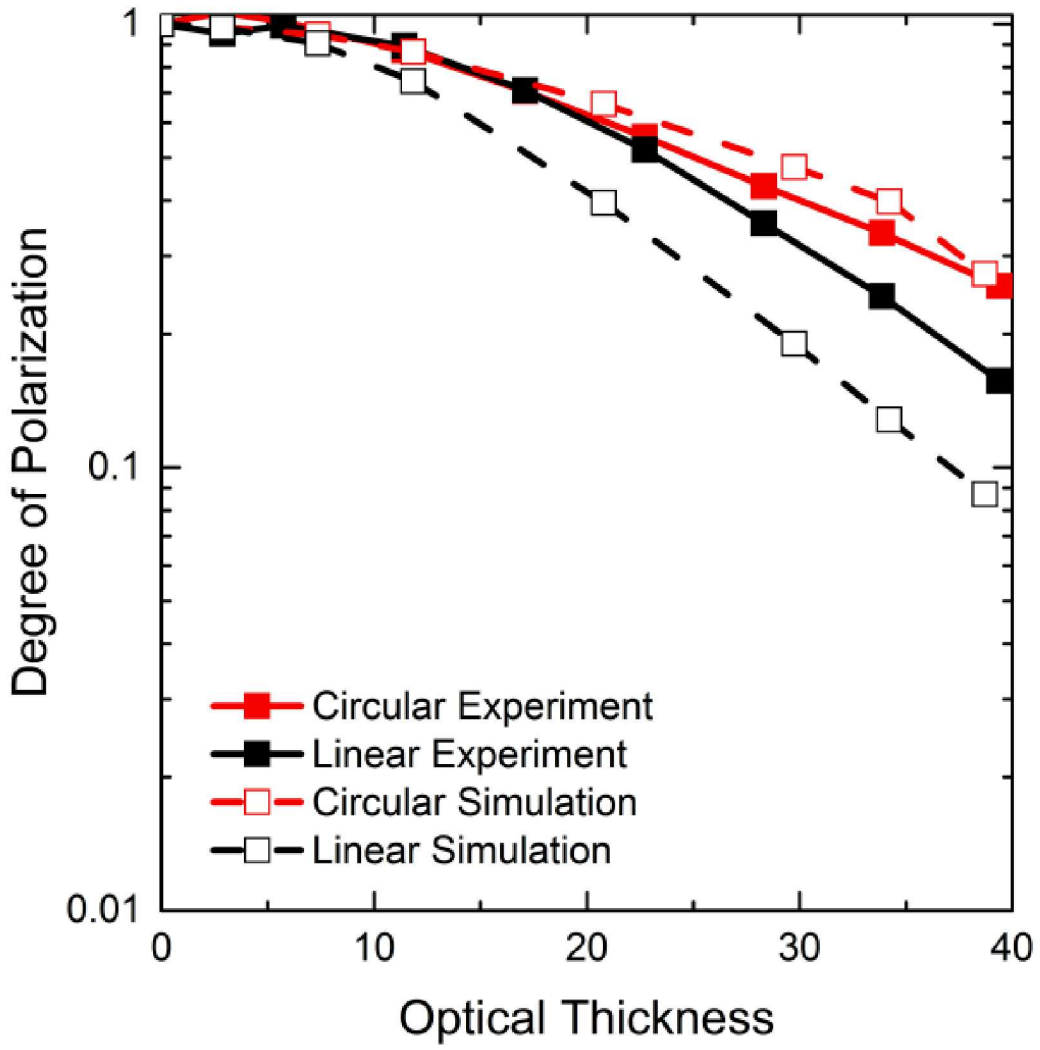

Figure 43: DoP versus optical thickness for measured and simulated forward-scattering environments of 1.925 µm polystyrene spheres in water.

5. Conclusions

We have shown circular polarization persists superiorly compared to linear polarization by a factor of 2-3 for highly scattering environments. This large increase in signal persistence can increase optical sensing range and target detection in critical environments such as fog. For the forward-scattering environment, circularly polarized light maintains its DoP through increasing optical thicknesses much better than linearly polarized light. The opposite is true for the isotropic-scattering environment; linear polarization maintains a slightly higher DoP. We show this in measurements and in simulations made with polystyrene microspheres in water with particle diameters of 0.0824 and 1.925 μm and an illuminating wavelength of 543.5 nm. Experimental and simulation results for these individual environments confirm similar trends. We hypothesize that the limited extent of the experimental cuvette's volume, compared to the infinite lateral extent in simulation, can account for the difference observed in measured and simulated DoP values. Future simulation analysis will take into account the limited environmental extent of the experimental cuvette as well as incorporate the Fresnel reflections from the cuvette walls.

Additionally, simulations for varying collection geometries, field of view and collection area, show different behaviors for polarization persistence measurements in isotropic-scattering or forward-scattering environments. Both linearly and circularly polarized light are shown to be susceptible to variations in the collection geometry and environmental extent for the isotropic-scattering environment. Similar susceptibilities are shown for linearly polarized light in the forward-scattering environment, although the effect is smaller. Uniquely, circular polarization is nearly unaffected by changes in the field of view and/or the collection area for the forward-scattering environment. Circular polarization proves to be more tolerant of variations in the field of view, collection area, and environmental extent compared to linear polarization. Circular polarization is thus more flexible and ideal for use in a wide range of optical system designs for forward-scattering environments.

7. EXPERIMENTAL RESULTS: SANDIA FOG FACILITY

Introduction:

This chapter describes experimental measurements made in Sandia's fog generation facility. This section presents the first polarization persistence measurements performed in the newly online facility. The initial experimental results were performed with a visible laser transmission and collection system. Circular polarization proved to perform better than linear polarization in these tests but visible wavelengths are not the ideal measurement wavelength. Simulation results for polarized persistence through a MODTRAN fog distribution model are also presented in this chapter. These simulations show that circular polarization's benefits will be more prevalent for Sandia's fog in the mid-wave infrared or long-wave infrared regimes.

Experimental Results in Sandia's Fog Facility

Sandia's Aerosol group (Org. 6633) currently has a fog generating facility that has a maximum path length of 180 feet. We performed polarization persistence measurements in the fog facility. The experimental setup is shown in Figure 44. The setup consists of two enclosed boxes with transmit and receive optical components. The path length, and thus the optical thickness, of the fog mixture was defined by the separation distance between the two boxes. The transmit box consists of a laser source and polarization generating optics. The laser source is a visible HeNe laser with a wavelength of 543.5 nm. An optical chopper is used to chop the laser at a frequency of roughly 1 kHz. A lock-in amplifier connects to this chopper and the signal detector in the receive box in order to recover the small collected scattered signal. A half-wave retarder and a polarizing beam cube act as a variable attenuator and set the initial polarization state to vertically linearly polarized. The output polarization state was then set by a quarter-wave retarder. Vertical linear polarized light was transmitted if the retarder's fast-axis was set vertically aligned with the initial vertical linear polarized light. Circular polarized light is transmitted when the retarder's fast-axis is set 45 degrees off from the vertical linear polarized lights oscillation. Only these two polarization states are transmitted through the fog allowing us to compare linear and circular polarization persistence through the fog mixture. The polarized laser light is then collimated and the beam is expanded with a 5x beam expander. The light exits the transmit box through a hydrophobic optical window. The polarized light is scattered by the fog and then collected and analyzed by the receive box. Similar to the transmit box the receive box has a hydrophobic optical window. The optical window has a diameter of 3 inches. The scattered light is then collected by collection optics. The light then is analyzed with a polarization analyzer that rejects light that is not polarized in the initial polarization state. The polarization analyzer consists of a quarter-wave retarder and a linear polarizer. The polarization analyzer rejects all light that is not vertically linearly polarized when vertical linear polarized light is transmitted into the fog, and similarly only right circular polarized light is collected when right circular polarization is incident to the fog.

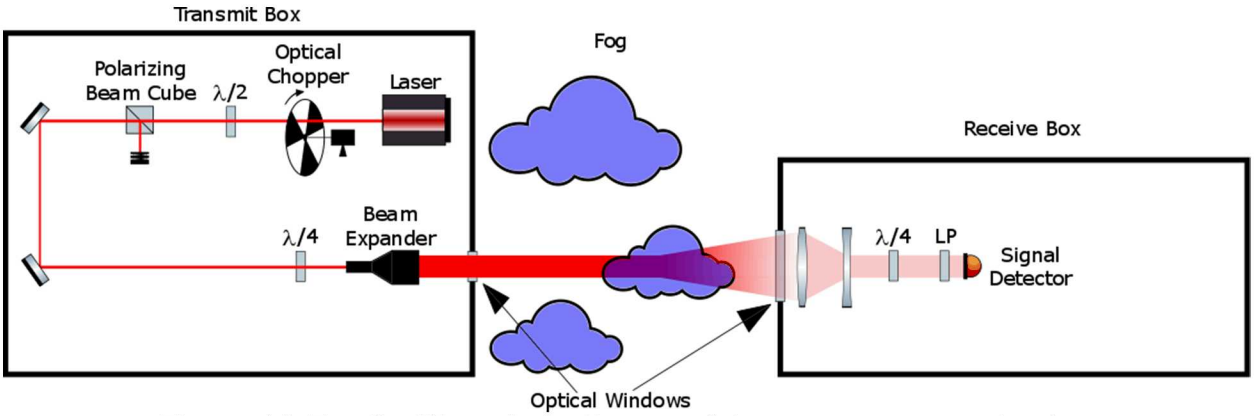

Figure 44: Fog facility polarization persistence measurement setup

The fog generated in Sandia's fog facility has until now not been characterized. Utilizing a Spraytec Instruments Malvern particle sizer the particle size distribution Sandia's generated fog was measured. Measured particle distributions for two different testing days are shown in Figure 45. The particle distributions are compared to a MODTRAN particle size model for radiation fog. The figure shows that the mean particle diameter for Sandia's fog facility is roughly 1 to 3 microns. The mean particle diameter for the MODTRAN radiation fog model is 4 microns. The MODTRAN model has a larger range of particle diameters but for scattering physics purposes the MODTRAN model and the measured particle distributions in Sandia's fog facility are very close.

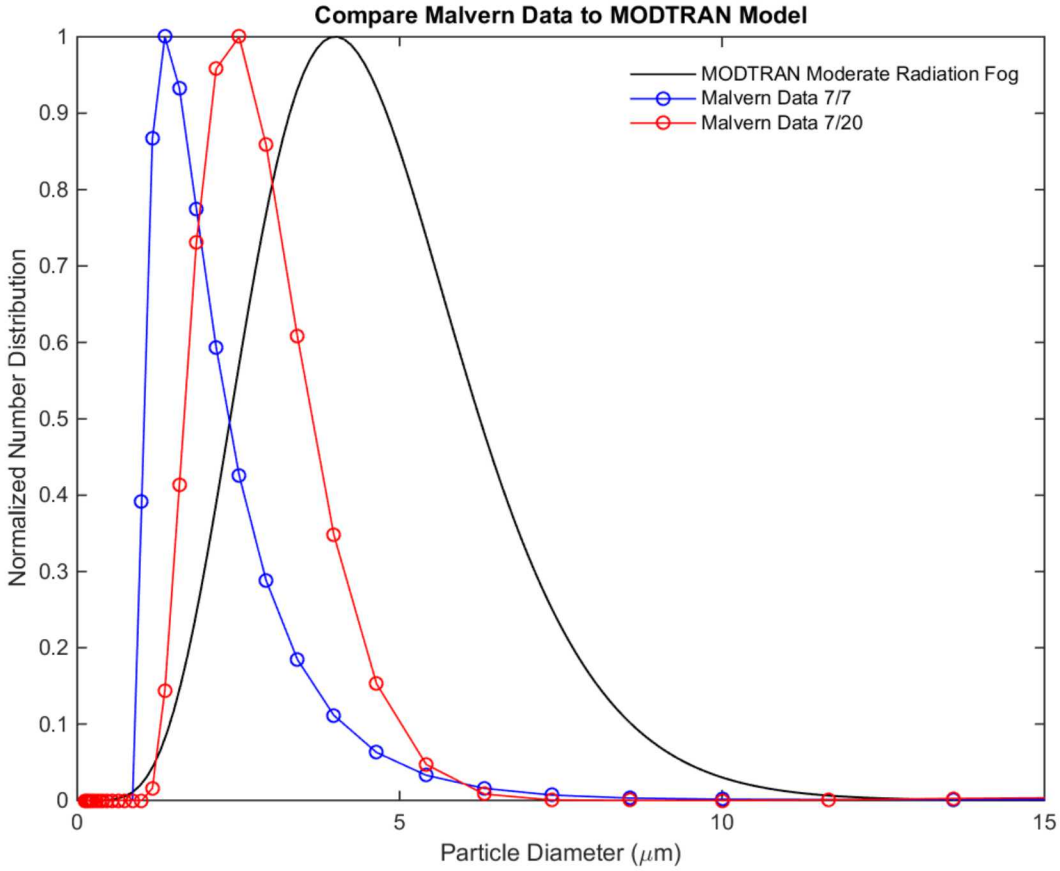

Figure 45: Particle size distributions for Sandia's fog facility compared to the MODTRAN radiation fog model

Simulations for a range of wavelengths for the MODTRAN radiation fog model were performed with the previously mentioned polarization-tracking Monte Carlo program. The degree of polarization difference for transmitted polarized light is shown in Figure 46. The simulation results show promised for circular polarization over a broad range of wavelengths for this fog model. Positive values of the DoP_{diff} means circularly polarized light persisted superiorly compared to linearly polarized light. The ideal wavelengths for the largest differences between linear and circular polarization are found in the MWIR and the low end of the LWIR. The predicted benefit for circular polarization at our experimental visible wavelength is less than five percent.

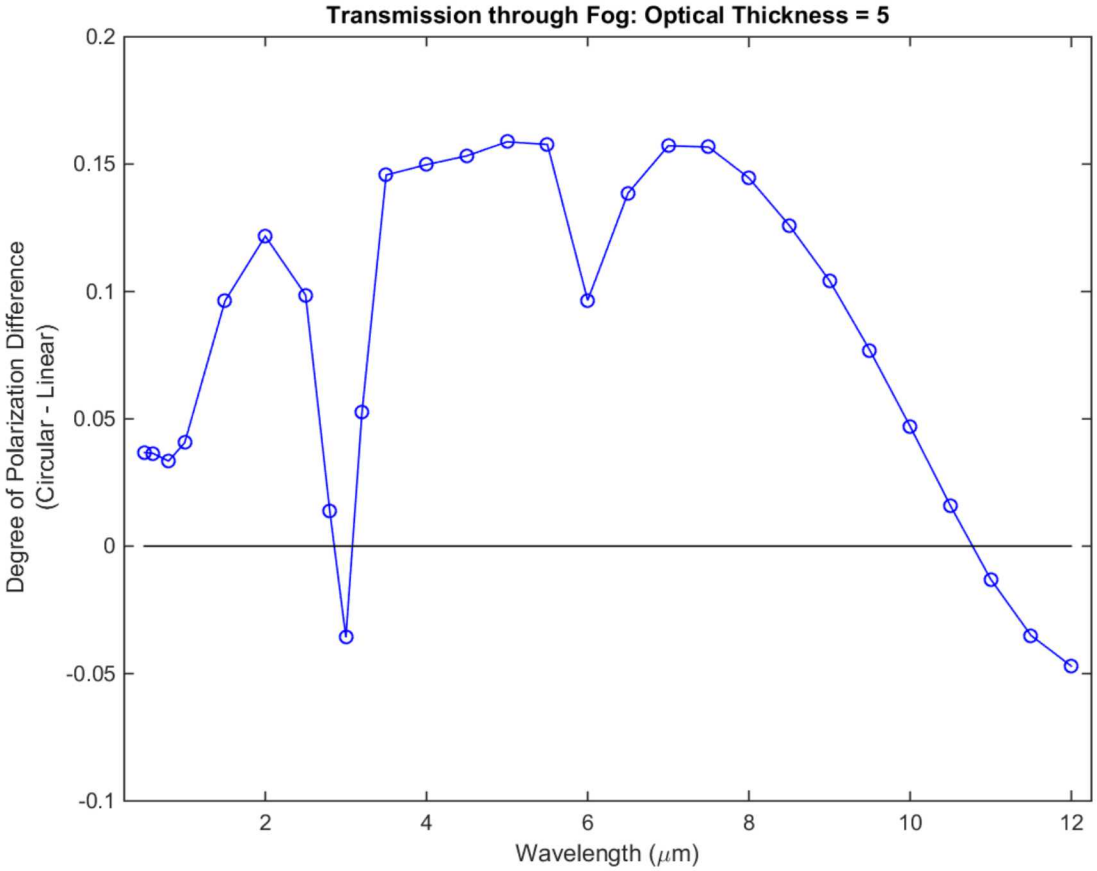

Figure 46: Degree of Polarization difference for polarized light transmission through a MODTRAN radiation fog model with an optical thickness of 5.

Transmitted polarization persistence measurements were performed for both linear and circular polarization over path lengths of 10, 20, 30, and 40 feet. The following figures show results for each path length.

10-foot Path Length:

Figure 47 shows the signal voltage collected over time for the 10 foot path length measurements. One hundred measurements were performed with a sample frequency of 12.5 seconds. This sample frequency is dictated by the rotation of the polarization analyzing optics for each polarization state. Within the same figure the second plot is the difference of the circular and linear signal values for each sample number. If the signal difference is positive then circular polarization has a higher signal transmitted than linear polarization, and vice versa if the signal difference is negative. Overall, the signal difference for circular and linear polarization is merely 0.5 percent. This results shows that there is insufficient path length to measure the polarization persistence effect.

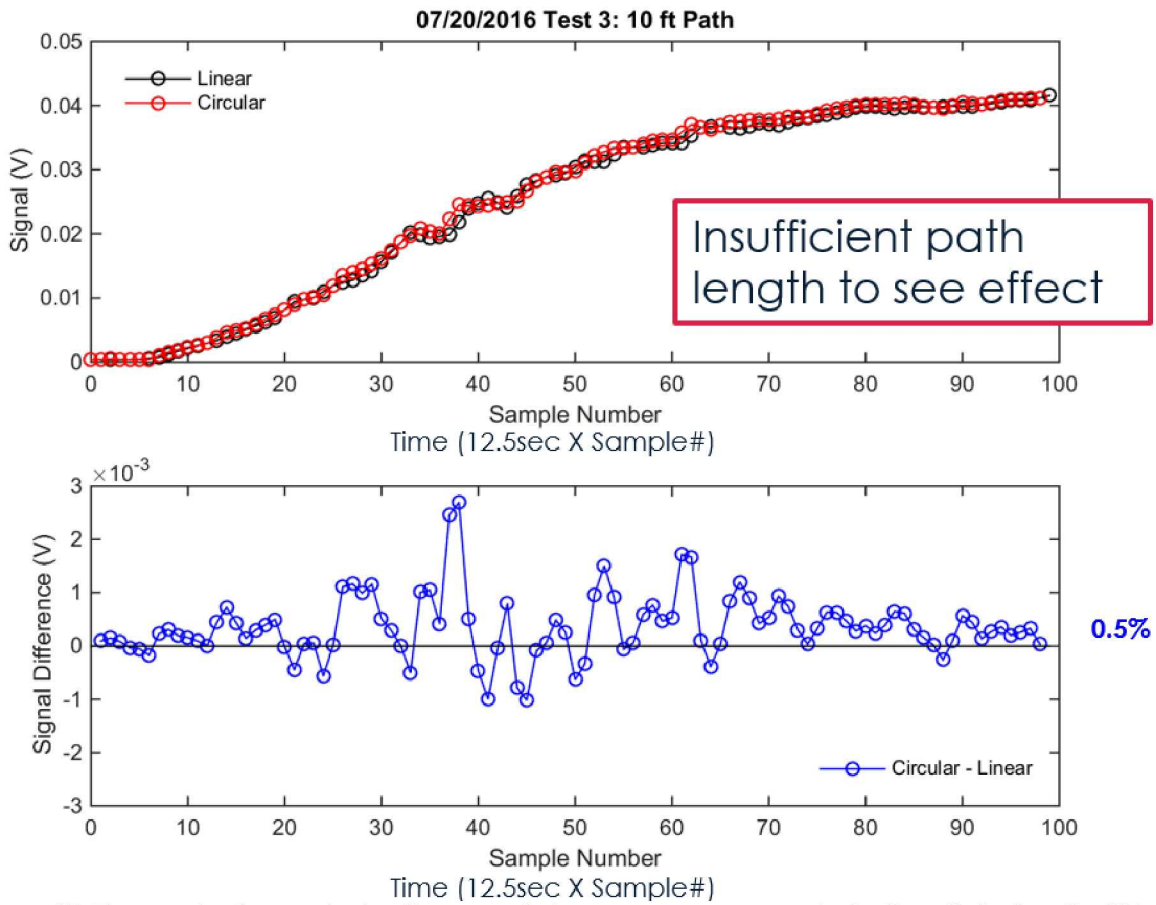

Figure 47:Transmission polarization persistence measurements in Sandia's fog facility for a path length of 10 feet

20-foot Path Length:

Figure 48 shows the signal voltage and signal difference for transmission through the fog for a path length of 20 feet. In the first half of the samples the density of the fog is such that the signal is very weak and have a lot of noise. After roughly 50 samples circular polarization show a clear increased persistence compared to linear polarized light. Overall, the difference between circular and linear polarization is on average 4.1 percent. This matches closely to what we expect based on the previously shown simulation results.

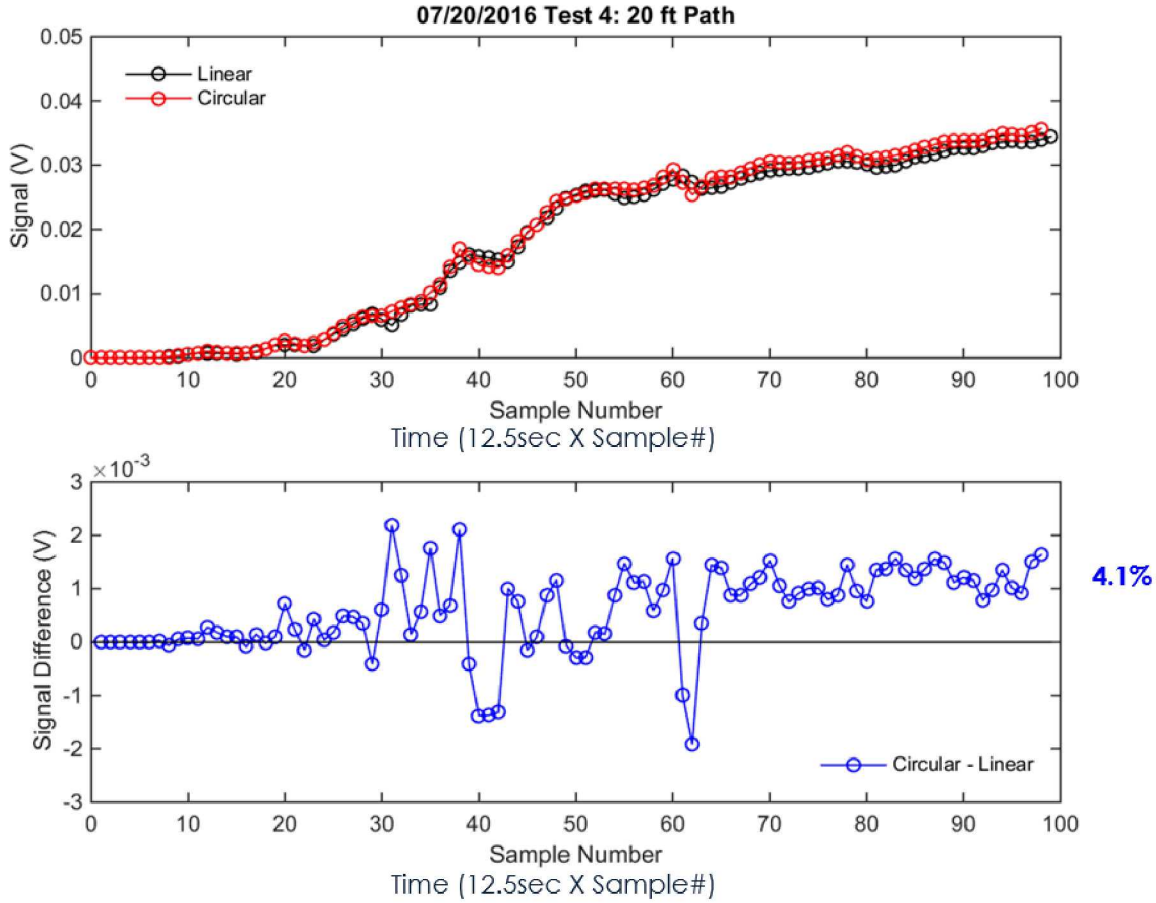

Figure 48:Transmission polarization persistence measurements in Sandia's fog facility for a path length of 20 feet

30-foot Path Length:

Figure 49 shows the measurement results for the 30 foot path length. Similar to the 20 foot results the signal difference is most apparent after roughly 50 samples. The results for the 30-foot case is very similar to the 20-foot case. The signal difference between circular and linear polarization is a mean value of 5.6 percent. This is slightly larger than the 20-foot case but still matches the expected signal difference predicted in simulations.

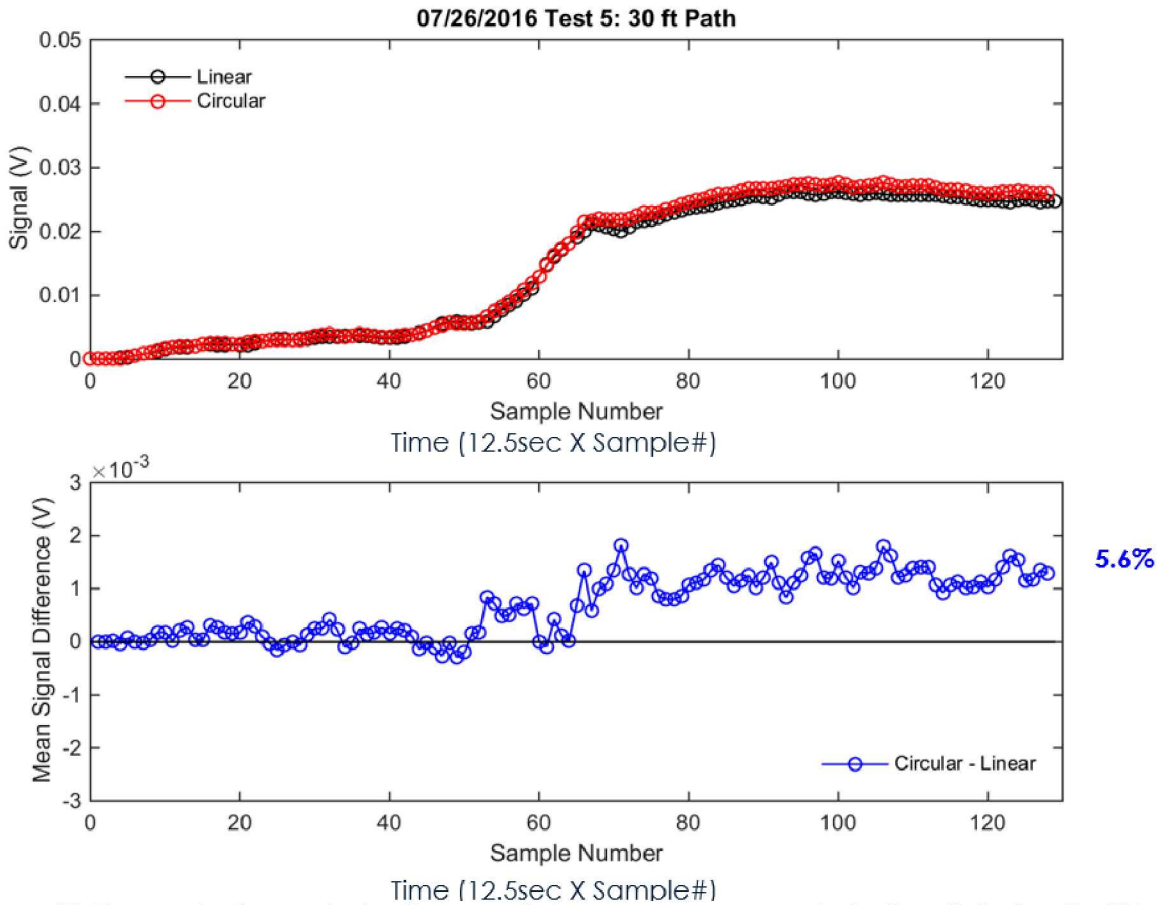

Figure 49:Transmission polarization persistence measurements in Sandia's fog facility for a path length of 30 feet

40-Foot Path Length:

Lastly, Figure 50 shows the experimental results for the 40-foot path length case. Once again this case shows similar results to the 20 and 30-foot path lengths. With the longer path length, the time to get sufficient signal is longer than the other cases. The signal difference between circular and linear polarization is smaller for this case with a mean value of 2.8 percent.

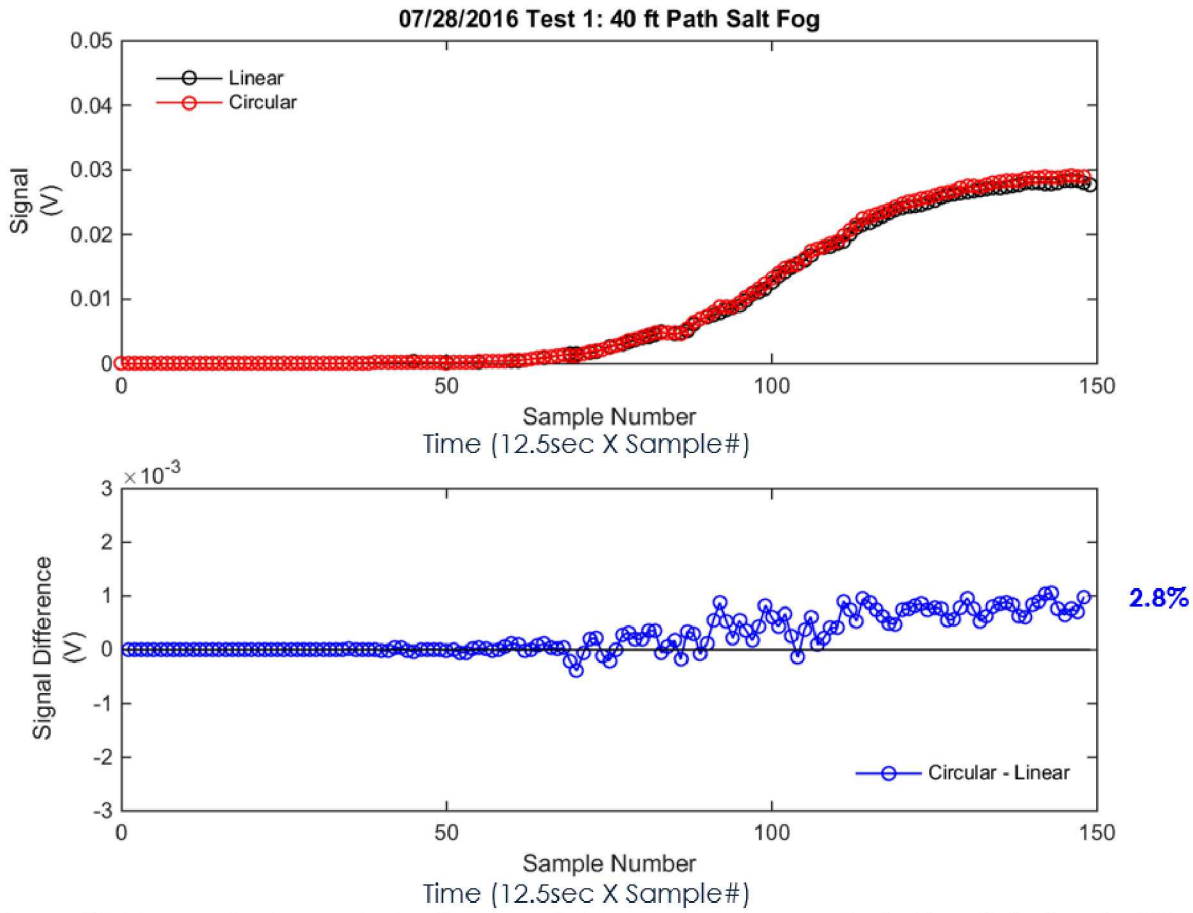

Figure 50:Transmission polarization persistence measurements in Sandia's fog facility for a path length of 40 feet

Conclusions:

Overall, circular polarization persists through the Sandia generated fog roughly 5 percent better than linear polarization for path lengths greater than 10 feet. This persistence benefit was predicted through polarization-tracking simulations and is within the range expected. Circular polarization clearly persists better than linear polarization in real world fog environments. Moving to longer wavelengths in the infrared are expected to produce much larger benefits for circular polarization.

The results presented throughout this chapter show that circularly polarized light is superior to linearly polarized light for signal persistence and tolerance to optical system variation. This makes circular polarized light ideal for use in LIDAR systems in typical denied environments, such as fog and dust.

8. CONCLUSIONS

LIDAR is an important technology that has far reaching implications in a number of important fields. However, due to the scattering of light it is limited to operating in clear conditions. Here, we have identified improved optical propagating wavelength and polarization state regimes that should open an operating window for LIDAR in obscured environments. Opening the operating window will be of great interest to airborne intelligence, surveillance, and reconnaissance for tactical situation awareness in denied environments. This addresses the US Special Operations Forces identified challenge of LIDAR in all environments, day and night. Additionally this work will have broad impact over a range of DOE and intelligence airborne and satellite programs. Our work had 2 primary focuses: 1) imaging LIDAR applications and 2) the operation of LIDAR in scattering environments (particularly fog). This was done in order to push towards an "all-weather" imaging LIDAR capability. Our work on imaging LIDAR has brought an important capability to Sandia for novel ISR platforms. Previous work focused on the use of linearly polarized light in laboratory scattering environments such as polystyrene microspheres in water. Here we investigated the application of both linear and circular polarization covering broad wavelength ranges and various scattering conditions. We have shown increased persistence of circular polarization which will manifest as an increased fidelity in range and discrimination for real world applications.

REFERENCES

[1] P. F. McManamon, "Review of ladar: a historic, yet emerging, sensor technology with rich phenomenology," *Opt. Eng.*, vol. 51, no. 6, pp. 60901–60913, 2012.

[2] R. M. Marino and W. R. Davis, "Jigsaw : A Foliage-Penetrating 3D Imaging Laser Radar System," *Lincoln Lab. J.*, vol. 15, no. 1, pp. 23–36, 2005.

[3] J. C. Ramella-Roman, S. A. Prahl, and S. L. Jacques, "Three Monte Carlo programs of polarized light transport into scattering media: part I.," *Opt. Express*, vol. 13, no. 25, pp. 10392–405, Dec. 2005.

[4] J. D. van der Laan, "Evolution and persistence of circular and linear polarization in scattering environments," University of Arizona, 2015.

[5] J. D. van der Laan, D. A. Scrymgeour, S. A. Kemme, and E. L. Dereniak, "Detection range enhancement using circularly polarized light in scattering environments for infrared wavelengths," *Appl. Opt.*, vol. 54, no. 9, pp. 2266–2274, Mar. 2015.

[6] G. D. Gilbert and J. C. Pernicka, "Improvement Of Underwater Visibility By Reduction Of Backscatter With A Circular Polarization Technique," *Proc. SPIE*, vol. 7. pp. 15–25, 1966.

[7] G. D. Gilbert and J. C. Pernicka, "Improvement of underwater visibility by reduction of backscatter with a circular polarization technique.," *Appl. Opt.*, vol. 6, no. 4, pp. 741–6, Apr. 1967.

[8] S. Q. Duntley, "Underwater visibility and photography," in *Optical Aspects of Oceanography*, Academic Press, 1974, pp. 138–149.

[9] J. S. Tyo, "Enhancement of the point-spread function for imaging in scattering media by use of polarization-difference imaging," *J. Opt. Soc. Am. A*, vol. 17, no. 1, pp. 1–10, Jan. 2000.

[10] M. P. Silverman and W. Strange, "Object delineation within turbid media by backscattering of phase-modulated light," *Opt. Commun.*, vol. 144, no. 1–3, pp. 7–11, Dec. 1997.

[11] M. Dubreuil, P. Delrot, I. Leonard, A. Alfalou, C. Brosseau, and A. Dogariu, "Exploring underwater target detection by imaging polarimetry and correlation techniques.," *Appl. Opt.*, vol. 52, no. 5, pp. 997–1005, Feb. 2013.

[12] V. Sankaran, K. Schönenberger, J. T. Walsh, and D. J. Maitland, "Polarization discrimination of coherently propagating light in turbid media.," *Appl. Opt.*, vol. 38, no. 19, pp. 4252–61, Jul. 1999.

[13] V. Sankaran, J. T. Walsh, and D. J. Maitland, "Comparative study of polarized light propagation in biologic tissues.," *J. Biomed. Opt.*, vol. 7, no. 3, pp. 300–6, Jul. 2002.

[14] S. Bartel and A. H. Hielscher, "Monte Carlo simulations of the diffuse backscattering mueller matrix for highly scattering media.," *Appl. Opt.*, vol. 39, no. 10, pp. 1580–8, Apr. 2000.

[15] G. D. Lewis, D. L. Jordan, and P. J. Roberts, "Backscattering target detection in a turbid medium by polarization discrimination.," *Appl. Opt.*, vol. 38, no. 18, pp. 3937–44, Jun. 1999.

[16] S. Kartazayeva, X. Ni, and R. Alfano, "Backscattering target detection in a turbid medium by use of circularly and linearly polarized light.," *Opt. Lett.*, vol. 30, no. 10, pp. 1168–70, May 2005.

[17] D. Bicout, C. Brosseau, A. Martinez, and J. Schmitt, "Depolarization of multiply scattered

waves by spherical diffusers: Influence of the size parameter," *Phys. Rev. E*, vol. 49, no. 2, pp. 1767–70, 1994.
[18] A. Ishimaru, S. Jaruwatanadilok, and Y. Kuga, "Polarized pulse waves in random discrete scatterers.," *Appl. Opt.*, vol. 40, no. 30, pp. 5495–502, Oct. 2001.
[19] D. Miller and E. L. Dereniak, "Selective polarization imager for contrast enhancements in remote scattering media.," *Appl. Opt.*, vol. 51, no. 18, pp. 4092–102, Jun. 2012.
[20] J. Fade, S. Panigrahi, A. Carré, L. Frein, C. Hamel, F. Bretenaker, H. Ramachandran, and M. Alouini, "Long-range polarimetric imaging through fog.," *Appl. Opt.*, vol. 53, no. 18, pp. 3854–65, Jun. 2014.
[21] J. S. Tyo, D. L. Goldstein, D. B. Chenault, and J. A. Shaw, "Review of passive imaging polarimetry for remote sensing applications.," *Appl. Opt.*, vol. 45, no. 22, pp. 5453–69, Aug. 2006.
[22] M. Xu and R. Alfano, "Circular polarization memory of light," *Phys. Rev. E*, vol. 72, no. 6, p. 65601, Dec. 2005.
[23] J. D. van der Laan, D. A. Scrymgeour, S. A. Kemme, and E. L. Dereniak, "Range and contrast imaging improvements using circularly polarized light in scattering environments," *Proc. SPIE*, vol. 8706. p. 87060R, 2013.
[24] C. Bohren and D. Huffman, *Absorption and scattering of light by small particles*. New York, New York, USA: John Wiley & Sons, Inc., 1983.
[25] K. Beier and H. Gemperlein, "Simulation of infrared detection range at fog conditions for Enhanced Vision Systems in civil aviation," *Aerosp. Sci. Technol.*, vol. 8, no. 1, pp. 63–71, Jan. 2004.
[26] R. A. Chipman, "Polarimetry," in *Handbook of Optics*, 1995, p. Vol. 2, Chap. 22.
[27] M. Al Naboulsi, H. Sizun, and F. de Fornel, "Fog attenuation prediction for optical and infrared waves," *Opt. Eng.*, vol. 43, no. 2, p. 319, Feb. 2004.
[28] D. Deirmendjian, "Scattering and polarization properties of water clouds and hazes in the visible and infrared," *Appl. Opt.*, vol. 3, no. 2, p. 187, 1964.
[29] D. L. Hutt, "Estimation of aerosol microphysical parameters from visible and infrared extinction measurements," *Proc. SPIE*, vol. 2828. pp. 503–514, 1996.
[30] D. Segelstein, "The complex refractive index of water," University of Missouri, 1981.
[31] B. Weinzierl, A. Petzold, M. Esselborn, M. Wirth, K. Rasp, K. Kandler, L. Schütz, P. Koepke, and M. Fiebig, "Airborne measurements of dust layer properties, particle size distribution and mixing state of Saharan dust during SAMUM 2006," *Tellus B*, vol. 61, no. 1, pp. 96–117, Feb. 2009.
[32] A. Ivanov, "Polarization of light and its use in various problems of optics of scattering media," *Opt. Spectrosc.*, vol. 107, no. 2, pp. 171–183, Sep. 2009.
[33] F. E. Volz, "Infrared optical constants of ammonium sulfate, sahara dust, volcanic pumice, and flyash.," *Appl. Opt.*, vol. 12, no. 3, pp. 564–8, Mar. 1973.
[34] L. S. Rothman, I. E. Gordon, Y. Babikov, A. Barbe, D. C. Benner, P. F. Bernath, M. Birk, L. Bizzocchi, V. Boudon, L. R. Brown, A. Campargue, K. Chance, E. A. Cohen, L. H. Coudert, V. M. Devi, B. J. Drouin, A. Fayt, J.-M. Flaud, R. R. Gamache, J. J. Harrison, J.-M. Hartmann, C. Hill, J. T. Hodges, D. Jacquemart, A. Jolly, J. Lamouroux, R. J. Le Roy, G. Li, D. A. Long, O. M. Lyulin, C. J. Mackie, S. T. Massie, S. Mikhailenko, H. S. P. Müller, O. V Naumenko, A. V Nikitin, J. Orphal, V. Perevalov, A. Perrin, E. R. Polovtseva, C. Richard, M. A. H. Smith, E. Starikova, K. Sung, S. Tashkun, J. Tennyson, G. C. Toon, V. G. Tyuterev, and G. Wagner, "The HITRAN2012 molecular spectroscopic

database," *J. Quant. Spectrosc. Radiat. Transf.*, vol. 130, no. 0, pp. 4–50, 2013.
[35] J. D. van der Laan, J. B. Wright, D. A. Scrymgeour, S. A. Kemme, and E. L. Dereniak, "Evolution of circular and linear polarization in scattering environments," *Opt. Express*, vol. 23, no. 25, pp. 31874–31888, Dec. 2015.
[36] G. D. Gilbert, "The effects of particle size on contrast improvement by polarization discrimination for underwater targets.," *Appl. Opt.*, vol. 9, no. 2, pp. 421–8, Feb. 1970.
[37] J. G. Walker, P. C. Chang, and K. I. Hopcraft, "Visibility depth improvement in active polarization imaging in scattering media.," *Appl. Opt.*, vol. 39, no. 27, pp. 4933–41, Sep. 2000.
[38] J. D. van der Laan, D. A. Scrymgeour, S. A. Kemme, and E. L. Dereniak, "Increasing detection range and minimizing polarization mixing with circularly polarized light through scattering environments," *Proc. SPIE*, vol. 9099. p. 909908, 2014.
[39] F. MacKintosh, J. Zhu, D. Pine, and D. Weitz, "Polarization memory of multiply scattered light," *Phys. Rev. B*, vol. 40, no. 13, pp. 9342–9345, 1989.
[40] A. D. Kim and M. Moscoso, "Backscattering of circularly polarized pulses.," *Opt. Lett.*, vol. 27, no. 18, pp. 1589–91, Sep. 2002.
[41] W. Cai, X. Ni, S. Gayen, and R. Alfano, "Analytical cumulant solution of the vector radiative transfer equation investigates backscattering of circularly polarized light from turbid media," *Phys. Rev. E*, vol. 74, no. 5, p. 56605, Nov. 2006.
[42] J. Sorrentini, M. Zerrad, G. Soriano, and C. Amra, "Enpolarization of light by scattering media," *Opt. Express*, vol. 19, no. 22, pp. 21313–21320, Oct. 2011.
[43] G. Soriano, M. Zerrad, and C. Amra, "Enpolarization and depolarization of light scattered from chromatic complex media," *Opt. Express*, vol. 22, no. 10, pp. 12603–12613, May 2014.
[44] M. Zerrad, G. Soriano, A. Ghabbach, and C. Amra, "Light enpolarization by disordered media under partial polarized illumination: The role of cross-scattering coefficients," *Opt. Express*, vol. 21, no. 3, pp. 2787–2794, Feb. 2013.
[45] A. Ghabbach, M. Zerrad, G. Soriano, and C. Amra, "Accurate metrology of polarization curves measured at the speckle size of visible light scattering," *Opt. Express*, vol. 22, no. 12, pp. 14594–14609, Jun. 2014.
[46] M. Zerrad, J. Sorrentini, G. Soriano, and C. Amra, "Gradual loss of polarization in light scattered from rough surfaces: Electromagnetic prediction," *Opt. Express*, vol. 18, no. 15, pp. 15832–15843, Jul. 2010.
[47] M. Zerrad, H. Tortel, G. Soriano, A. Ghabbach, and C. Amra, "Spatial depolarization of light from the bulks: electromagnetic prediction," *Opt. Express*, vol. 23, no. 7, pp. 8246–8260, Apr. 2015.
[48] A. Ghabbach, M. Zerrad, G. Soriano, S. Liukaityte, and C. Amra, "Depolarization and enpolarization DOP histograms measured for surface and bulk speckle patterns," *Opt. Express*, vol. 22, no. 18, pp. 21427–21440, Sep. 2014.
[49] J. D. van der Laan, D. A. Scrymgeour, J. B. Wright, S. A. Kemme, and E. L. Dereniak, "Increasing persistence through scattering environments by using circularly polarized light," *Proc. SPIE*, vol. 9465. p. 94650U, 2015.
[50] D. Goldstein, *Polarized Light, Revised and Expanded*. CRC Press, 2003.
[51] W. A. Shurcliff, *Polarized Light*. Cambridge, MA: Harvard University Press, 1962.
[52] H. G. Akarçay, A. Hohmann, A. Kienle, M. Frenz, and J. Rička, "Monte Carlo modeling of polarized light propagation: Stokes vs. Jones. Part I," *Appl. Opt.*, vol. 53, no. 31, pp.

7576–7585, Nov. 2014.
[53] G. G. Stokes, "On the composition and resolution of streams of polarized light from different sources," *Trans. Camb. Phil. Soc.*, vol. 1, no. 9, pp. 399–416, 1852.
[54] J. D. van der Laan, J. B. Wright, D. A. Scrymgeour, and S. A. Kemme, "Effects of collection geometry variations on linear and circular polarization persistence in both isotropic-scattering and forward-scattering environments," *Appl. Opt.*, p. In Review.
[55] N. Ghosh, P. K. Gupta, H. S. Patel, B. Jain, and B. N. Singh, "Depolarization of light in tissue phantoms – effect of collection geometry," *Opt. Commun.*, vol. 222, no. 1–6, pp. 93–100, 2003.
[56] A. J. Gomes, V. Turzhitsky, S. Ruderman, and V. Backman, "Monte Carlo model of the penetration depth for polarization gating spectroscopy: influence of illumination-collection geometry and sample optical properties," *Appl. Opt.*, vol. 51, no. 20, pp. 4627–4637, Jul. 2012.
[57] A. J. Gomes, H. C. Wolfsen, M. B. Wallace, F. K. Cayer, and V. Backman, "Monte Carlo model of the depolarization of backscattered linearly polarized light in the sub-diffusion regime," *Opt. Express*, vol. 22, no. 5, p. 5325, 2014.
[58] V. M. Turzhitsky, A. J. Gomes, Y. L. Kim, Y. Liu, A. Kromine, J. D. Rogers, M. Jameel, H. K. Roy, and V. Backman, "Measuring mucosal blood supply in vivo with a polarization-gating probe.," *Appl. Opt.*, vol. 47, no. 32, pp. 6046–6057, 2008.
[59] J. C. Ramella-Roman, S. a Prahl, and S. L. Jacques, "Three Monte Carlo programs of polarized light transport into scattering media: part II.," *Opt. Express*, vol. 13, no. 25, pp. 10392–405, Dec. 2005.
[60] X. Ma, J. Q. Lu, R. S. Brock, K. M. Jacobs, P. Yang, and X.-H. Hu, "Determination of complex refractive index of polystyrene microspheres from 370 to 1610 nm.," *Phys. Med. Biol.*, vol. 48, no. 24, pp. 4165–72, Dec. 2003.
[61] I. Freund and M. Kaveh, "Comment on ``Polarization memory of multiply scattered light'','' *Phys. Rev. B*, vol. 45, no. 14, pp. 8162–8164, Apr. 1992.

DISTRIBUTION

1	MS0509	D. Wiegandt	5330
1	MS0957	Robert Spulak	5331
1	MS0957	S. Kemme	5331
1	MS0957	J. Wright	5331
1	MS0957	J. van der Laan	5331
1	MS1082	D. Scrymgeour	1728
1	MS1153	D. Gardner	5444
1	MS1161	T. Stalker	5447
1	MS0899	Technical Library	9536 (electronic copy)
1	MS0359	D. Chavez, LDRD Office	1911

Sandia National Laboratories